Segmentation and Evaluation of Fluorescence Microscopy Images

Christophe Restif

Thesis submitted in partial fulfilment of the requirements of the award of

Doctor of Philosophy

Oxford Brookes University

July 2006

Abstract

This dissertation presents contributions to the automation of cell image analysis, in particular the segmentation of fluorescent nuclei and probes, and the evaluation of segmentation results. We present two new methods of segmentation of nuclei and chromosomal probes – core objects for cytometry medical imaging. Our nucleic segmentation method is mathematically grounded on a novel parametric model of the image, which accounts at the same time for the background noise, the nucleic textures and the nuclei's contribution to the background fluorescence. We adapted an Expectation-Maximisation algorithm to adjust this model to the histograms of each image and subregion of interest. A new dome-detection algorithm is used for probe segmentation, which is insensitive to background and foreground noise, and detects probes of any intensity. We have applied these methods as part of a large-scale project for the improvement of prenatal diagnostic of genetic diseases, and tested them on more than 2,100 images with nearly 14,000 nuclei. We report 99.3% accuracy for each of our segmentation methods, with a robustness to different laboratory conditions unreported before. We compare our methods with existing methods, which we review in detail. We use them to study the reliability of telomeric probe intensity in order to differentiate maternal and fetal leucocytes, and show a promising trend.

We also detail a novel framework for referencing objects, combining references and evaluating segmentation results with a single measure, in the context of medical imaging, where blur and ambiguity add to the complexity of evaluation. This framework introduces a novel method called *Confidence Maps Estimating True Segmentation* (*Comets*). We compare this framework to existing methods, show that the single measure allows intuitive quantitative and qualitative interpretation of discrepancy evaluation, and illustrate its use for tuning parameters on large volumes of data.

Finally we explain how our methods were ported to a high performance computing cluster server, based on XML databases and standard communication protocols, to allow reliable, scalable and robust image processing that can be monitored in real time.

Acknowledgements

First of all, I wish to thank my parents for always being there when I needed them, from my early stage of thinking about a PhD, till the end of it. I also thank my brothers Olivier and Cyrille, my sisters-in-law Aurore and Marie, for their continuous help and support.

I would not have started my PhD without the help of many friends and colleagues during my time in Paris, a help which was much needed in a time of changing my professional and personal life. I thank in particular my almost siblings Carine Babet, Anne Mestre and Guy Muller, my recommenders Julie Le Cardinal, Patrick Callet and Frédérique Itier, the Orsyp gang Prakash Hemchand, Frédéric Caloone, Michel Enkiri, Mauro Robbe, Arnaud Lamy, Stéphane and Anne-Sophie Daudigeos, Renaud Fargis, Alain Brossard, Alexandre Balzeau, Esther Fernandez, Anthony Raison, Olivier Denel and Jean-Michel Breul, my osteopath Sam Cohen, and my all-time friends Marie Blanchard, Virginie Prioux, Ségolène Trésarrieu, Jean-Philippe Alexander, Odile Prevost, Cécile Rançon, Magali Druot and the Skalabites band, Nathalie Alepée, Marie Gélibert and the other rock'n roll dancers. Many thanks also to the Cambridge gang MengMeng Wang, Jorge Biaggini, Christophe Beaucé and Giamee, who supported me from around the world.

My time in Oxford has been a wonderful experience. I thank my supervisor William Clocksin, in particular for obtaining my scholarship, and my other supervisors John Nealon and Phil Torr. I give special thanks to Matthieu Bray and Tony McCollum, who have been constantly helping and supporting me, especially during our endless talks at Cleo's. My housemates and lab-mates have been a pleasure to live with: Sarah, Tom, Derek and the publishers gang, Caroline and Ulf, Coco, Jess, Yue, Minhue, Tim, Joumana, David, the 'elder' PhD students Christine, Peter, Prem, and the 'younger' ones Wee-Jin, Pawan, Pushmeet, Carl, Pratheep, Sammy, Karteek, Chris, Jon. Many thanks to the friends who brightened my days, in particular to Arnaud, José, Cristiana, Anne-Gaëlle and her friends at the pancake parties, Shemi, Roni, Chloe, Ariel and Nevyanne, trainer Aline and the salsa teachers Rosa, Giles, Lisa, Mark. Teaching has been a rewarding experience, and I thank in particular Nigel Crook, Anne Becker, Peter Marshall, Samia Kamal, and the computing department staff for their help and all my students for their enthusiasm.

Last but not least, I thank my girlfriend Aurore Aquilina, for sharing my life and supporting me whenever I need it.

To my parents, my brothers, and my whole family,

To Carine Babet, Anne Mestre,
Guy Muller and Matthieu Bray,

To Aurore Aquilina.

Contents

List of Figures

List of Tables

List of Algorithms

Chapter I

Introduction

Segmentation is of fundamental importance in computer vision for discriminating between different parts of an image. In cytometry, segmentation is used for the delineation of cells and their components, in particular their nuclei and specific parts of their chromosomes. Our particular interest is in fluorescence *in-situ* hybridisation (FISH) microscopy, in which cells are prepared with fluorescent probes that bind to given DNA sequences. Improved segmentation methods could be used for qualitative and quantitative assay of cell samples.

It has been proposed recently that FISH can be used to discriminate maternal from fetal cells in the maternal bloodstream. Automating this idea places new demands on segmentation techniques and offers new challenges to computer vision. In this dissertation we present new contributions that offer significant improvements in automated cytometry.

I.1. Towards safer and faster prenatal genetic tests

I.1.1 Fetal cells in maternal blood

Over the past twenty years, the age at which women become pregnant has been rising significantly in Western countries. This is known to increase the risk of genetic disease for the babies. A typical example is the age-related increase of frequency of Down syndrome [58, 191], due to trisomy 21 (when cells have three number 21 chromosomes). Thanks to the progress made by research in genetics, many genetic diseases can be detected during pregnancy [4]. However, current diagnostic methods require invasive procedures during pregnancy. Two common examples are amniocentesis and chorionic villus sampling: fetal cells are sampled directly from within the womb. These methods offer reliable results, but are uncomfortable, time-consuming, and associated with a 1-2% rate of miscarriage [4, 59]. Although these methods are widely used, those risks and costs prevent them from being routinely used on all pregnant women.

Intensive research is done in biology and cytometry to develop non-invasive alternatives to detect genetic diseases in the fetus. A European Commission-funded Network of Excellence called SAFE (standing for Special non-invasive Advances in Fetal and neonatal Evaluation) has recently been started to investigate and develop such alternatives. One of the promising areas of investigation is the automated recognition of fetal cells in maternal blood. It has been known for a few decades that a few fetal cells enter the maternal circulation through the placental barrier [60, 182]. Isolating these cells non-destructively would give access to complete genetic information about the fetus, from a maternal blood sample.

Two major issues arise. First, these cells have to be discriminated from maternal cells in a reliable way. Currently, the most informative descriptor is the sex chromosomes [78]. In case the fetus is male, its cells will contain a Y chromosome,

whereas the maternal cells will contain only X chromosomes. Consequently, this method cannot be applied when the fetus is female. There is still need for another discriminant to identify fetal cells within a maternal sample with certainty. Possible markers, such as telomeres, are under investigation, and our work is part of this effort. The second issue is that fetal cells in maternal circulation are present but rare [80]. Depending on the cells' types, a non-processed blood sample may contain one fetal cell within 10^4 to 10^9 maternal cells [80, 99]. Enrichment methods exist: the sample can be physically filtered, which reduces the concentration to 1 in 10^4 or 10^5 [64]. This still classifies the problem as a rare-event search. Computer vision can make the detection of fetal cells easier [113], which is also an application of our work.

Although many types of fetal cells are present in maternal blood, not all can be used. The main factor distinguishing them is their expected life-time within the maternal circulation [60]. Because they qualify as foreign body in the maternal fluids, they are targeted by the maternal immune system. The cells with the shortest lifetimes, on the order of hours [78], cannot be relied on for our work, as too few would be present. On the contrary, those with the longest lifetimes, on the order of years [60] or decades [124], cannot be used either: it would be too difficult to determine their origin in case of multiple pregnancies. The cells chosen for our work are leucocytes, or white-blood cells. Their lifetime on the order of a year [60, 152], makes them still acceptable for our purposes, as this whole project is still in a pilot phase. Besides, unlike other cells, effective enrichment methods are available for leucocytes [64, 65]. Thus, leucocytes offer a reasonable trade-off.

Telomeres are repeated sequences of DNA, namely $(T_2AG_3)_n$, located at the end of each chromosomes, about ten thousand base pair long [28, 86, 148, 151]. They contain no genetic information, and shorten during cell divisions throughout the life of an individual [22, 63, 151]. They stand out as potential discriminants between maternal and fetal cells for the following reasons. They are proven to be longer in fetal cells than in maternal ones, by about 30% [148]. Secondly, marking them does not alter the genetic material of a cell, which can still be fully investigated afterwards. Finally, specific markers and techniques exist to tag telomeres and visualise the results [6, 86, 112], using Fluorescence *in-situ* Hybridization (FISH), detailed in the next section. These theoretical reasons still have to be tested quantitatively [128, 139].

Another issue affects the study of fetal cells in maternal circulation. As the environmental conditions in the maternal blood are very different from those in the womb (e.g. the oxygen pressure is 10 times higher in the maternal circulation [5]), and since the immune system is targeting them, fetal cells are physically affected when they pass the placental barrier. Although it does not affect their

genome, it alters their physical properties. As a result, they cannot be easily cultivated in vitro, unlike other cells [60]. Without cultivation, they cannot be prepared and imaged during metaphase, when chromosomes separate before cell division. They have to be imaged as they were in the sample, in interphase. Many studies of telomeric length assessment have been published using cultured cells [6, 86, 112, 183]. The clear separation of chromosomes during metaphase helps the analysis of genes and telomeres and its automation with computer vision [128, 139]. In particular, quantitative FISH (Q-FISH) [138], which can be used to evaluate telomeric length, requires intact metaphase spread [151]. However, previous work based on metaphase cannot be applied in our context. A significant difference between the two phases is the arrangement of chromosomes within the cells. During metaphase, the nucleus border vanishes, and chromosomes are clearly distinguished in X-shapes and occupy the whole cell. In interphase though, they are wrapped within the nuclei. They can still be used for diagnostic purposes: about 70% of chromosomal abnormalities can be detected in interphase cells [60].

An application of our work is to evaluate whether quantifying telomere length based on FISH image analysis provides a good discriminant between fetal and maternal cells, in the case of uncultured interphase leucocytes.

I.1.2 Fluorescence microscopy

Fluorescence is a physical property of some specific materials. When illuminated at specific wavelengths, usually in the ultraviolet (UV) domain, *i.e.* between 100 nm and 400 nm, fluorescent materials emit light back, at lower wavelength, usually in a specific portion of the visible spectrum (e.g. blue, red, green). This phenomenon is well described by quantum physics: the illumination excites the material, which progressively relaxes to its original non-excited state. The final part of the relaxation causes the emission of photons, at a lower energy than the excitation.

Fluorescence has been widely used as a marker in various fields, from physics, mineralogy, to biology and cytometry, as early as the 1930s. Fluorescent markers have been developed for specific cells, parts of cells, nuclei and chromosomes. In our context, we are interested in visualising two types of objects: nuclei and telomeres. Two specific markers exist for them. Nuclei can be stained thoroughly with diamidinophenylindole (DAPI), a fluorescent marker that emits blue light (maximum of emission at 461 nm [25]). Telomeres can be marked with fluorescein isothiocyanate (FITC), which emits green light (maximum of emission at 519 nm [25]). These markers can be attached to the cells' components with hybridisa-

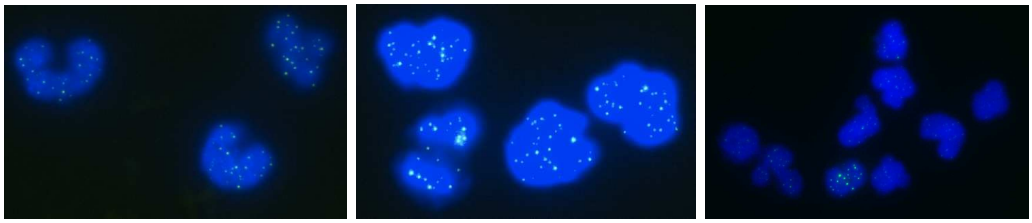

Figure I.1.1: *Three typical images obtained with the FISH technique.*

tion: they complement specific DNA and other chemical sequences, and can thus chemically attach to chosen specific places, such as telomeres and nuclei. This technique is called Fluorescence *in-situ* Hybridisation (FISH): the fluorescence observed is emitted at the place where the hybridisation happened. Details on the FISH techniques and applications can be found in [25, 95, 113].

Fluorescence microscopy differs from classic optic microscopy. In classic microscopy, the sample to visualise is placed between a source of visible light and the observer. The light is either absorbed by or transmitted through the sample. Fluorescence microscopy follows the following principle. A high-intensity UV light is directed at the sample; the fluorescent markers in use emit light at specific visible wavelengths; these signals are then observed through adapted filters. The fluorescent signals obtained are recorded on a charge-coupled device (CCD) camera, resulting in as many grayscale images as the number of filters used. In our case, each sample is imaged twice, one in the blue domain for the nuclei, and one in the green domain for the telomeres. To account for the volume of the objects, the sample is imaged at fields of view of different depths, distant by 50 nm. The results are averaged to define the final image. Typical reconstructed and coloured images are shown in Figure I.1.1. Incidentally, in the wavelength domains used for imaging, the objects imaged are actually sources of light.

The objects in the image are to be analysed in the following way. The nuclei have to be delineated, or *segmented*, and their telomeric contents evaluated. This requires the segmentation of the green signals visible inside them. Although these signals are attached to telomeres, some telomeres may be unattached to FITC material and vice versa. For this reason, we will refer to the small bright green signals as *probes*, not telomeres. Technically, the task consists in segmenting nuclei in the DAPI channel, then segmenting the corresponding probes in the FITC channel, and evaluating the telomeric contents of every nucleus. As we know beforehand which nuclei are fetal and which are maternal, a statistical study on the results obtained will indicate whether this protocol enables a sufficient discrimination between maternal and fetal nuclei.

The core of this work lies in the two segmentation steps, one for the nuclei and one for the probes. Segmentation results are used to evaluate the differences between the estimated telomere lengths in different individuals. Also, the

segmentation results need to be evaluated as such.

I.1.3 Need for evaluation

Evaluating a segmentation method is at the same time necessary, important, and ill-posed. It is necessary to rank segmentation results obtained by different methods, or one method with different sets of parameter values, in order to select a method or to tune parameters. Although this sounds natural, deciding on a way to rank results can actually be difficult. Evaluating a method is also important in order to assess and validate it: this requires to have a quantitative and qualitative measure of the segmentation results. Here again, deciding on a metric to perform these measures is not obvious. Finally, evaluation in itself is an ill-posed task. It refers to different criteria, some of which have various interpretations and are measured with various metrics.

Recent publications have clarified the different evaluation criteria. In [201], Zhang describes three types of evaluation, namely analysis, goodness, and discrepancy. *Analysis* focuses on the algorithm used in a segmentation method, in particular its complexity, in terms of memory or runtime. This type of evaluation is important to assess the performance of an algorithm, or to implement optimisation. In our context however, analysis is not the main evaluation required: runtime, memory allocation or optimisation are secondary for our pilot study. *Goodness* evaluates results based on image and object properties, regardless of external references. It can be based on intra-region uniformity, inter-region contrast, or region shapes. These somehow artificial criteria have been used to reproduce human judgement on the quality of segmentation in itself. They do not apply in our task however: our goal is not to produce visually pleasing results, but to accurately segment nuclei and probes. The final criterion by Zhang is *discrepancy*: this type of evaluation consists in comparing results against references. It requires prior referencing of the images, and a measure to compare a computed segmentation against a reference segmentation. This is the evaluation required in our context. It allows an objective comparison of segmentation methods and guidelines for tuning a method's parameters.

I.2. Specifications of the cytometric task

In this section we detail the specific requirements and issues of the cytometric task introduced in the previous section.

As a pilot study, several sets of leucocytes are to be analysed. There are four sets, each containing two or three populations of leucocytes, separated from each other: one from a fetus (obtained through cord-blood), one from an adult woman, and in some sets one from an adult man. Each population, containing several hundred cells, was processed and imaged with the FISH technique following the same protocol. One of our tasks is to develop an image processing tool to evaluate the quantity of telomeres visible in all the images. Given the high volume of data to process, the tool is required to be fully automated and robust enough to process all the samples. Figure I.2 shows the main steps of the required processing.

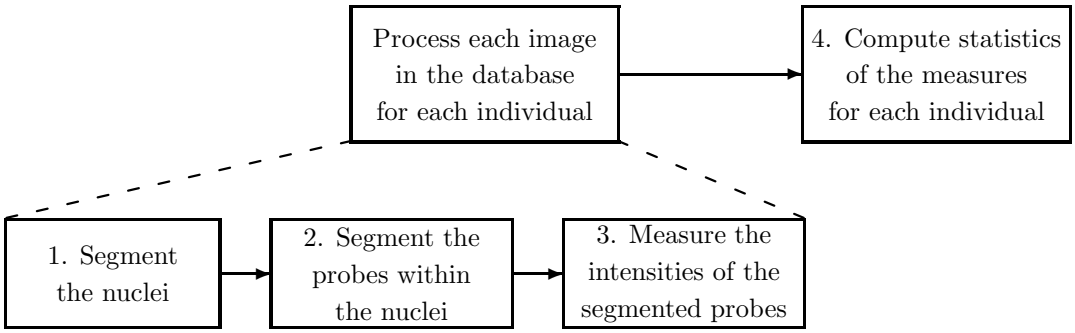

Figure I.2.1: *The main steps of our image analysis tool.*

I.2.1 Nucleic segmentation

Nucleic segmentation consists in localising and delineating all the nuclei present in each image. Although the protocols followed during the sample preparation and imaging are consistent, there are unavoidable variations of experimental and

imaging conditions. The following variations have significant impact on the image quality. First, the nuclei show a wide range of appearances, in terms of sizes, shapes and textures. Figure I.2.2 shows nuclei with different appearances. In particular, as the nuclei were not cultured, specific processing ensuring the convexity of nuclei could not be applied: nuclei do not have fixed convexity or concavity. Second, the concentration of nuclei within an image is not consistent. Images may contain from zero to a few dozen nuclei. Some nuclei are isolated, other are close to their neighbours but still distinguishable by eye: we use the term *touching nuclei* to describe them. Other nuclei are tightly clustered and visually undistinguishable: we use the term *clustered nuclei*. See Figure I.2.3 for an illustration of those three cases. Finally, another important type of variation affects the image histograms. The range of pixel intensities within an image is sometimes restricted to 200 values, or conversely reaches 1,000 values. The histograms' shapes may show any number of peaks, valleys, and may contain peaks resulting from saturation at high intensities. Figure I.2.4 presents three different histograms.

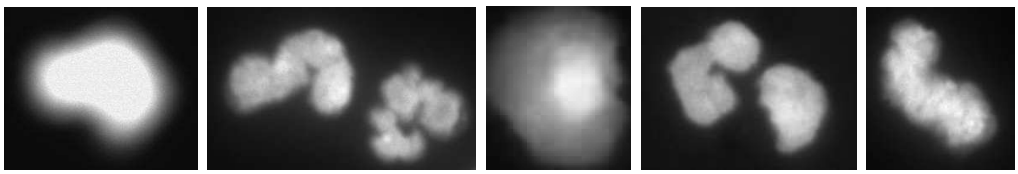

Figure I.2.2: *Variations of nuclei's appearances, in terms of shapes and textures.*

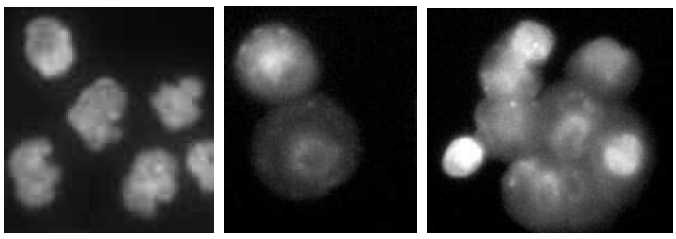

Figure I.2.3: *Variations of nuclei's concentrations. Left: isolated nuclei. Middle: touching nuclei. Right: clustered nuclei.*

An important property of the DAPI images results from the nature of the FISH imaging technique. As explained in the previous section, the nuclei are imaged as sources of light. When illuminated in their excitation domain, the DAPI markers emit light in every direction. The optics used in the microscope filters the direction of light before imaging. However, not all the light collected comes directly from the nuclei. Part of the light emitted in different directions is deflected in the medium surrounding the nuclei, and part of it is collected on the image. This induces a significant increase of intensity in the background regions

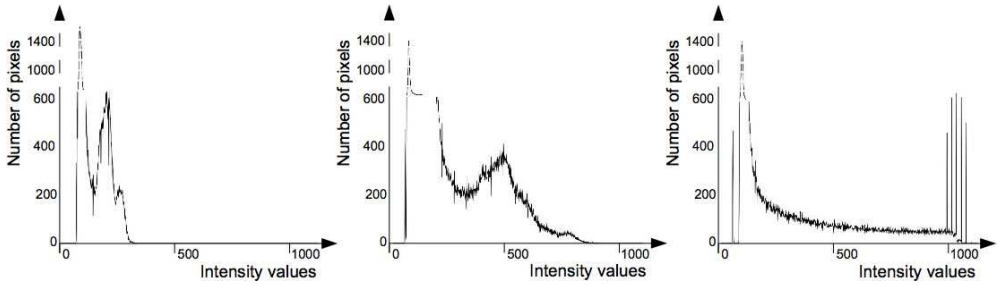

Figure I.2.4: *Variations affecting image histograms: three examples of histograms with different range of values. Left: compact range. Middle: medium range. Right: wide range with high-intensity peaks resulting from saturation.*

immediately surrounding the nuclei. We call this effect *background illumination*, and refers to the background surrounding nuclei as illuminated background. This phenomenon is illustrated in Figure I.2.5.

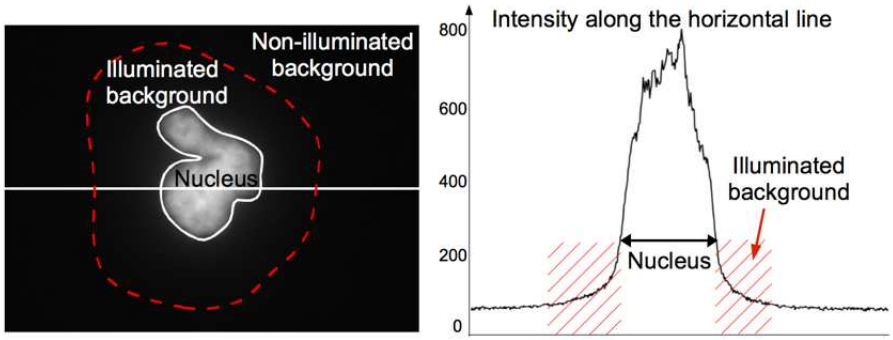

Figure I.2.5: *Background illumination. Top left: image with three segmented regions: nucleus, illuminated and non-illuminated background. Right: intensity values along the horizontal line across the image. The intensity in the illuminated background is significantly higher than in the non-illuminated background.*

I.2.2 Probe segmentation

Once the nuclei have been segmented in the DAPI images, their content is to be evaluated in the FITC images. The probes they contain appear as small bright circles. In the same way, the range of intensities vary significantly across images, due to slightly different imaging conditions.

Another issue affects the quality of the FITC images. As explained above, the probes are hybridised to telomeres, then the excess non-attached probes are washed out of the sample. However, this washing cannot be performed perfectly. Consequently, unwashed probes tend to gather in large clusters, which appear very bright on the FITC images. We refer to these cluster as *foreground noise*.

Although it is a relatively rare phenomenon, affecting about one in thirty images, it has a significant impact on the image processing. When foreground noise overlaps a nucleus, it hides the attached probes, and might alter the intensity measures performed to evaluate the telomeric contents: thus it should not be segmented as probes. An example of foreground noise overlapping a nucleus is shown in Figure I.2.6.

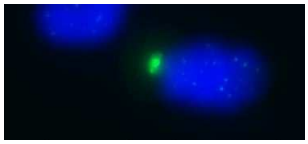

Figure I.2.6: *Foreground noise in the FITC channel: unwashed cluster of FITC probes overlap a nucleus, thus hiding part of its actual contents.*

I.2.3 Evaluation of a segmentation method

As explained in Section I.1.3, the segmentation results have to be evaluated, using a discrepancy evaluation against references. The results should be quantitative, in order to rank different segmentation methods or tune one method's parameters. In addition, there needs to be a qualitative description of the results as well. We identified four issues related to evaluation in our context. First, segmentation results need to be presented in more categories than a "correct / incorrect" binary outcome: there are several ways in which a segmentation result may be wrong. Possible segmentation outcomes are:

– Correct: the segmented shape is correct, though it might not be a perfect match for a pre-defined reference on the object.

– Over-segmented: part of the object is missed by the segmentation.

– Under-segmented: conversely, part of the background (or another object) is wrongly segmented as the object.

– Missed: the whole object is labeled as background.

– Noise: background is labeled as a valid object.

Not all the incorrect results have the same severity. As we are interested in evaluating the telomeric contents of the segmented objects, over-segmentation will affect the measures. Under-segmentation is less severe, unless part of an object is segmented as another object: that would affect the measures for two objects. A missed object is not significant for our pilot study, where we are analysing single populations. However, in the long run the method we develop is meant to identify rare fetal nuclei within a maternal population: missing nuclei would then be a serious issue. Finally, segmented noise can be identified after the seg-

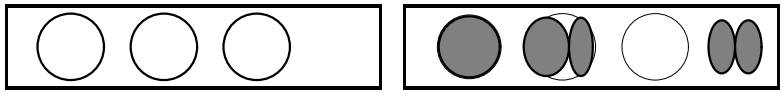

Figure I.2.7: *Ambiguity in evaluating a segmentation method. Left: image with three references. Right: same image with five segmented objects. 33% of the references are correctly segmented by objects, but only 20% of the objects correctly segment references.*

mentation, as not containing probes: it is the less severe outcome in our context. An evaluation method has to account for these different categories. When over- and under-segmentation occur on the same object, our approach is to classify the result as the most severe of these two errors.

The second issue concerns the definition of a correctly segmented object. In our images, objects boundaries span over several pixels, as a result of the following imaging features. First, as in other medical imaging fields, partial volume effect occurs in microscopy: at the border between objects, more than one object contribute to the pixel intensities. Nuclei are curved objects, and are imaged at different depths before the final image is constructed. At each depth a nucleus will appear with a slightly different radius. In the resulting image the nuclei's borders will thus be slightly blurred. Secondly, the background illumination described above induces intensity smoothing between a nucleus and its surrounding background, which increases the boundary blur. Finally, although autofocus is used during image acquisition, some slides may be slightly blurred if the optical settings are not optimal. All these effects contribute to the visual blur, which has to be accounted for during the evaluation: there has to be some tolerance margin, so that segmented objects not perfectly matching a reference may still be classified as correct.

The third issue we identified is inter- and intra-user variability, and is also present in other medical imaging fields. Different experts, or one expert at different times, may disagree on some parts of the objects' boundaries, while agreeing on others. This calls for a way to combine multiple reference segmentations into a single one. Ideally this process should keep as much expert knowledge as possible.

The final issue lies in the interpretation of evaluation results. Fig. I.2.7 shows an artificial reference and segmentation output. While one in three references are correctly segmented, it is also true that only one in five segmented objects correctly segment a reference. Thus the success rate of that segmentation could either be 33% or 20%. Similarly, the oversegmentation rate may either be one in three, or two in five. Published results [66, 143] tend to use the former of those numbers. Meaningful as it is, this approach does not account well for the amount of noise segmented as objects, nor for the number of objects oversegmenting one reference. There is a need to clarify the interpretation of results while presenting as much data as possible.

I.3. Contributions and outline

In this section we list the contributions we have made to provide a working tool for the tasks presented in section I.1, given the specifications and issues detailed in section I.2, and we present the outline of this dissertation.

I.3.1 Contributions

In this work we present the following contributions:

1. A novel segmentation method for fluorescent nuclei which is at the same time automatic, robust and more accurate than previously published work, achieving a success rate of 99.3% on our data set, containing nearly 14,000 objects. It is based on a novel mathematically grounded model of the image, and uses an adaptation of the Expectation-Maximisation algorithm for histogram modeling.

2. A novel segmentation method for fluorescent probes, also automatic, robust in particular to foreground noise, and which also has a success rate of 99.3% on our data set. It is based on a novel dome-detection algorithm sensitive to the local density of local maxima in image values.

3. A novel method of referencing medical images, with efficiently stored local confidence factors, which can be used to combine multiple references while keeping more expert knowledge than existing methods, and to evaluate segmentation results quantitatively and qualitatively, with a single measure.

4. A comprehensive and consistent review of existing segmentation methods in cytometry, with particular emphasis on their strengths, weaknesses and improvements.

5. An XML database structure adapted to our cytometric task.

6. A detailed case study of porting an image analysis tool to a cluster.

7. Complete working software, developed in Java, to reference medical images, tune a segmentation method's parameters, mass process any volume of images on a cluster, and visualise segmentation and evaluation results, with consistent interfaces and framework.

I.3.2 Outline

This dissertation is organised as follows.
Chapter I introduces the task at hand, presents its technical specifications and its challenges as a computer vision problem, and lists our contributions.
Chapter II reviews the state-of-the-art segmentation methods published and currently used in cytometry, discusses their strengths and weaknesses, and presents recent improvements, in the light of our cytometric task.
Chapter III presents our novel segmentation methods, for the nuclei and for the probes. It details their underlying principles and algorithms, and compares them qualitatively and quantitatively with existing methods.
Chapter IV details our novel method to reference images and evaluate segmentation methods, called *Comets*. It explains how a reference is built from user input, how multiple references are combined, and how segmentation results are evaluated both quantitatively and qualitatively with a single measure. It also presents a quantitative comparison with existing evaluation methods.
Chapter V discusses the main issues addressed in this work, and lists three future projects emerging from this work, namely a classification of segmented nuclei in terms of usability, a further possible use of *Comets*, and the adaptation of our segmentation methods for another cytometric task based on other types of cells.
Appendix A details some of the algorithms presented in Chapter II.
Appendices B to D describe the software we developed for segmentation and evaluation. Appendix B presents the underlying XML database used, Appendix C explains the way the image processing was ported to a cluster, and Appendix D illustrates the user interfaces.

Chapter II

Review of Segmentation Methods for Cytometry

In this chapter we present several segmentation methods used in cytometric applications. We list some of the most popular methods in Table II, published for the segmentation of specific types of cells.

In this review we deliberately take an application-oriented approach: we review existing methods in the light of our application, described in the previous chapter. Our approach is different from other published literature reviews on medical image segmentation. The reviews by McInerney and Terzopoulos [109], and by Lehmann *et al.* [90] are method-oriented: they focus on one segmentation method, active contours, and review its adaptations to several types of medical images, such as brain or heart scans. In [133], Pham *et al.* review segmentation methods for various types of images, but do not mention cytometry. In application-oriented theses for cytometry, Laak [178] and Wahlby [181] review two segmentation methods, low-level vision operations and watershed. To the best of our knowledge, the review closest to our work is in the thesis by Bamford [10], where four segmentation methods for cytometry are reviewed; however, only the underlying ideas are described, not their actual implementations nor their improvements.

We detail four commonly used methods, namely low-level vision operations, watershed, active contours and level sets, and present four less frequent methods in cytometry, based on region growing, neural networks, region competition and graph cut. For each method, we detail the original definitions, discuss the strengths and weaknesses, and present several published improvements.

In this chapter we consider two dimensional grayscale images, and note $f(x, y)$ the integer pixel value at location (x, y).

Table II.0.1: *Existing segmentation methods applied to cytometry. The methods of initialisation are specified in the third column when relevant.*

Segmentation method	*Type of cell*	*References*
low-level vision	leucocytes	[3, 16, 83, 97]
	fibroblasts	[115, 128, 157]
	erythroblasts	[113, 131]
	tumour cells	[125, 163]
	malaria	[147]
	meristem	[166]
	neurons	[120]
	bacteria	[85]
	cervical cell nuclei	[178]
	melanoms	[3]
	mitochondria	[57]
watershed	cervical cell nuclei	[71, 96] (init: threshold)
	tumour cells	[50, 181] (init: threshold)
	bone marrow nuclei	[104] (init: low-level vision)
	dermatofibroma	[170] (init: threshold)
	brain cells	[98] (init: low-level vision)
active contours	leucocytes	[35] (init: clustering)
	bone structures	[88] (init: manual)
	neurons	[18, 114] (init: manual)
	cervical cell nuclei	[10] (init: watershed)
	nodules	[198] (init: manual)
level sets	prostate cells	[153] (init: clustering)
region growing	karyocytes	[200] (init: threshold)
	cervical cell nuclei	[7] (init: clustering)
	leucocytes	[36] (init: threshold)
	tumour cells	[126] (init: low-level vision)
neural networks	-	-
region growing	-	-
graph cut	-	-

II.1. Low-level vision

Low-level vision consists in processing the image at the pixel-value level, using very little knowledge of the image contents. It is commonly used in many vision systems, though often only for pre-processing. In cytometry however, it is often used to achieve complete segmentation. There are several equivalent definitions of low-level vision operations [45,46]. For consistency we describe them as kernel-based filtering processes whenever possible. We present our formalism, and detail low-level vision operations for noise reduction, shape smoothing, shape extraction, image transform, and thresholding.

A. Original definitions

Kernel-based filtering: A *kernel*, or structuring element, may be seen as a small image. It is defined by its size in pixels, its domain or geometry (e.g. a disk or a square), its application point (by default its centre) and its shape, *i.e.* its values: the kernel is *flat* if it contains only 0 and 1, *non-flat* otherwise. We use the following notations: a kernel k is defined over a domain $D(k)$, indexed by (i, j). Without loss of generality, we consider $D(k)$ to be square and centred: $D(k) = [-n, n] \times [-n, n]$ for some odd $n \geq 1$. Figure II.1.1 illustrates how to build a *filtered image* g from an original image f and a kernel k. For some operations, e.g. dilation, the filtered image g is conventionally noted f *symbol* k, where *symbol* is specific to each operation.

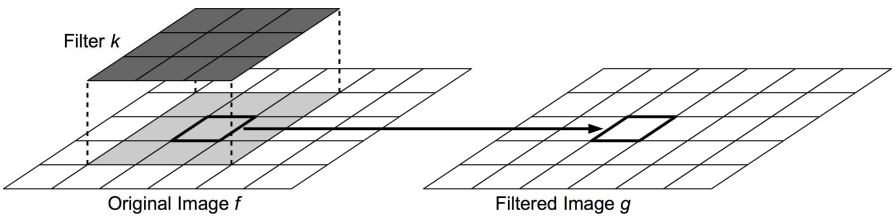

Figure II.1.1: *Image filtering.*

Noise reduction: Two ways to reduce the effects of noise are filtering and the construction of a pyramid of images. *Average filtering* is achieved by:

$$k_{av} = \frac{1}{9}\begin{pmatrix} 1 & 1 & 1 \\ 1 & 1 & 1 \\ 1 & 1 & 1 \end{pmatrix} \ , \ g(x,y) = \sum_{(i,j)\in D(k_{av})} k_{av}(i,j)\cdot f(x+i,y+j) \qquad \text{(II.1.1)}$$

Gaussian filtering [117] uses the same formula for g, but with non-flat kernels approximating two-dimensional Gaussian, such as:

$$\frac{1}{4}\begin{pmatrix} .25 & .50 & .25 \\ .50 & 1 & .50 \\ .25 & .50 & .25 \end{pmatrix} \ , \ \frac{1}{4.76}\begin{pmatrix} 0 & .04 & .08 & .04 & 0 \\ .04 & .28 & .50 & .28 & .04 \\ .08 & .50 & 1 & .50 & .08 \\ .04 & .28 & .50 & .28 & .04 \\ 0 & .04 & .08 & .04 & 0 \end{pmatrix} \qquad \text{(II.1.2)}$$

An alternative is *median filtering*, where k_{med} may be 3×3 or 5×5:

$$k_{med} = \begin{pmatrix} 1 & 1 & 1 \\ 1 & 1 & 1 \\ 1 & 1 & 1 \end{pmatrix} \ , \ g(x,y) = median\left\{f(x+i,y+j)\ ,\ (i,j)\in D(k_{med})\right\} \qquad \text{(II.1.3)}$$

These noise-reducing filters are routinely used before segmentation [3, 125].

Another approach to noise filtering is to build a *pyramid of images*, from fine to coarse resolution. It is assumed than images at coarser resolution will only show the main features of the image, rougher but easier to segment. Pyramid construction is the basis of segmentation techniques using *coarse-to-fine strategies*. Once a pyramid is built, the coarser images are segmented first. The labels found are then transferred to the next finer scale for improvement. There are many ways to build a lower-resolution image f_{low} from an image f_{high}, which are essentially sub-sampling methods iterated a few times. Formally, each pixel (u,v) in f_{low} is computed from a subset of pixels $S_{u,v} = \{(x,y)\}$ in f_{high} (see Figure II.1.2). During the coarse-to-fine process, the label of (u,v) will be passed to the pixels $(x,y)\in S_{u,v}$ for refinement. A simple sub-sampling is the following:

$$\begin{cases} S_{u,v} = \{(2u,2v),\ (2u+1,2v),\ (2u,2v+1),\ (2u+1,2v+1)\} \\ f_{low}(u,v) = mean\{f_{high}(x,y)\ ,\ (x,y)\in S_{u,v}\} \end{cases} \qquad \text{(II.1.4)}$$

Other formulas may be used, such as cubic splines [21, 176]. Gaussian pyramids [23, 149] use wider subsets, and weight the values using Gaussian filtering. However, the subsets of neighbouring pixels overlap: during the coarse-to-fine process, the pixels in the overlap will receive two labels.

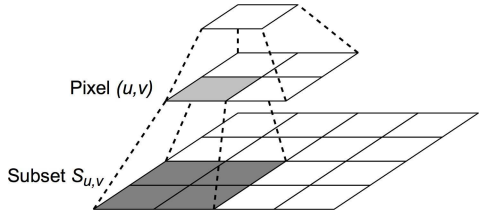

Figure II.1.2: *Pyramid of images.*

Shape smoothing: A shape can be smoothed by smoothing its borders, or by filling the holes it may contain. Borders can be smoothed by *dilation* and *erosion*, which respectively expand and shrink the shape, or by *opening* and *closing*, which do not affect the overall size of the shape. Any kernel can be used for all these operations, depending on the smoothing effect expected. The erosion $\ominus$ and dilation $\oplus$ of image f by kernel k are defined as:

$$\begin{aligned}(f \ominus k)(x,y) &= \min\{f(x+i,y+j) - k(i,j),\ (i,j) \in D(k)\} \\ (f \oplus k)(x,y) &= \max\{f(x+i,y+j) + k(i,j),\ (i,j) \in D(k)\}\end{aligned} \tag{II.1.5}$$

The opening $\circ$ and closing $\bullet$ of f by k are defined as:

$$f \circ k = (f \ominus k) \oplus k\ ,\ f \bullet k = (f \oplus k) \ominus k \tag{II.1.6}$$

It is to be noted that opening and closing may alter the connections between components.

A segmented shape can also be smoothed by filling the holes in it. Holes are background pixels surrounded by foreground pixels. They can be identified as background connected components that are not connected to a known background region, such as the edges of the image. Efficient algorithms to find connected components are described in [44]. Closing may be used to fill holes as well, but it can also adversely affect the connections between the segmented components.

An alternative to smooth the borders and fill holes at the same time is the use of convex hull. In [162], Soille describes methods to compute binary and grayscale convex hulls efficiently. In short, the binary convex hull of an object is defined as the intersection of all the semi-planes that contain the object. It is computed by finding the lines, in several directions, that touch the object without intersecting it. Incidentally, the difference between an object and its convex hull enhances its concavities, which may be useful for object recognition. This technique can be used to detect overlapping convex cells [85].

Shape extraction: A grayscale image can be viewed as a 3D landscape, with the gray value of a pixel indicating the height of the point. This way, objects of interests may appear as peaks (sharp mountains), domes (smooth hills), or

valleys (V- or U-shaped). Such features can be extracted with morphological operations. The open $\hat{\circ}$ and close $\hat{\bullet}$ *top-hat transforms* of an image f by a kernel k respectively extract the peaks and the V-shaped valleys in f. They are defined as:

$$f\hat{\circ}k = f - (f \circ k)\ ,\ f\hat{\bullet}k = (f \bullet k) - f \tag{II.1.7}$$

As with opening and closing, any kernel k can be used. The domain and shape of k actually control the extend and size of the peaks and valleys extracted [45,46,187].

The extraction of domes and U-shaped valleys can be performed with *grayscale reconstruction* [46,179]. The U-shaped valleys of depth h in f are extracted as the domes of height h in the inverse of f. See Appendix A.1 page 126 for details on grayscale reconstruction.

Image transform: These operations turn f into an image with the same dimensions but whose values are in another domain. Common transforms are gradient extraction (edge map and gradient vector flow), which turns an image into its derivative, and distance transform, which turns a binary image into grayscale.

Computing the gradient intensity per pixel results in an image called an *edge map*. Even though the gradient is mathematically defined for continuous two-dimensional functions, there are several definitions of gradient when it comes to image processing. *Morphological gradient* [46] is defined as the subtraction between the dilation and erosion of a image, with two kernels k_e and k_i (usually $k_e = k_i$):

$$\nabla_{k_e,k_i} f = (f \oplus k_e) - (f \ominus k_i) \tag{II.1.8}$$

The term $f \oplus k_e$ is called external gradient, and $f \ominus k_i$ internal gradient. The resulting value reflects the norm of the gradient, but gives no indication on its orientation.

Analytical gradients are computed with filters reproducing finite differences. The same formula:

$$g(x,y) = \sum_{(i,j)\in D(k)} k(i,j) \cdot f(x+i, y+j) \tag{II.1.9}$$

is used with different kernels, to compute the intensity of the gradient projected onto different directions. The classic filters used are the Roberts operators (resp. horizontal, vertical and two diagonals):

$$\begin{pmatrix} 0 & 0 & 0 \\ -1 & 1 & 0 \\ 0 & 0 & 0 \end{pmatrix}, \begin{pmatrix} 0 & -1 & 0 \\ 0 & 1 & 0 \\ 0 & 0 & 0 \end{pmatrix}, \begin{pmatrix} -1 & 0 & 0 \\ 0 & 1 & 0 \\ 0 & 0 & 0 \end{pmatrix}, \begin{pmatrix} 0 & 0 & -1 \\ 0 & 1 & 0 \\ 0 & 0 & 0 \end{pmatrix} \tag{II.1.10}$$

and the Sobel edge-detectors:

$$\begin{pmatrix} -1 & 0 & 1 \\ -2 & 0 & 2 \\ -1 & 0 & 1 \end{pmatrix}, \begin{pmatrix} -1 & -2 & -1 \\ 0 & 0 & 0 \\ 1 & 2 & 1 \end{pmatrix}, \begin{pmatrix} -2 & -1 & 0 \\ -1 & 0 & 1 \\ 0 & 1 & 2 \end{pmatrix}, \begin{pmatrix} 0 & -1 & -2 \\ 1 & 0 & -1 \\ 2 & 1 & 0 \end{pmatrix} \quad \text{(II.1.11)}$$

The same method can be applied to compute Laplacian of images (second derivative). Using Equation II.1.9, the non-directional Laplacian can be computed with the kernels [187]:

$$k_{Lapl4} = \begin{pmatrix} 0 & -1 & 0 \\ -1 & 4 & -1 \\ 0 & -1 & 0 \end{pmatrix}, k_{Lapl8} = \begin{pmatrix} -1 & -1 & -1 \\ -1 & 8 & -1 \\ -1 & -1 & -1 \end{pmatrix} \quad \text{(II.1.12)}$$

The gradient direction can be computed at the same time as its intensity, resulting in a vector-valued image. One technique is called *gradient vector flow (GVF)* [194, 195]. It is detailed in Appendix A.1 page 127.

The *distance transform* turns a binary image f into a gray-scale image g: each foreground pixel in f is assigned a grayscale value proportional to the distance to the closest background pixel. The Chamfer algorithm [187] is a filter-based method to compute the distance transform in the inside of objects. It can be used to compute the l_0 and l_1 distances correctly, with appropriate filters. However, the l_∞ distance can only be approximated: better approximations require bigger filters and thus more computation time. Besides, it can only be applied to images where the foreground is surrounded with background. An alternative, fast algorithm applicable to every image to compute the square of the l_∞ distance exactly is detailed by Felzenszwalb and Huttenlocher [51]. It is reproduced as Algorithm 3 in Appendix A.1 page 128. During the algorithm, g is scanned only twice, and at the end, it contains the square of the Euclidian distance transform of f.

Thresholding: It consists in labeling a pixel as foreground if it is above a threshold value, and as background if it is below. The threshold value may be the same for all pixels, or it may be a function $T(x, y)$ of the pixel location, called a *threshold surface*. Several thresholds may be used to obtain multi-labeled segmentation. For robustness, thresholds can be computed using image features, e.g. its histogram (*histogram-based threshold*) or using local statistics (*space-based threshold*). Sezgin *et al.* recently published a comprehensive review of thresholding techniques [156]. Two histogram-based threshold methods popular in cytometry are Otsu's and the isodata [104]. They are detailed in Appendix A.1 page 128. More histogram-based thresholds are presented in [159].

A simple way to define a threshold surface consists in dividing the image into smaller tiles [29, 67, 118, 169, 190]. A single threshold value is computed for each tile; these values are then interpolated over the image.

B. Strengths

The morphological operations described above are straightforward and quick to implement: they only require image scanning and histogram computations. The main parameters to tune are the size, geometry and shape of the kernel: their meaning are intuitive and their effects are easy to perceive. They have linear complexity, little memory requirements, and thus are fast at runtime. Also, given the range of functions they perform, they can easily be combined to achieve the complete segmentation of an image [120]. Finally, even though they are defined on binary and grayscale images, they can be extended to colour images or stacks of images, using vector-valued or 3D kernels.

C. Weaknesses

They actually suffer from their simplicity: they can only include very little knowledge about the objects to segment. Thus, they are mostly ad-hoc techniques, selected and tuned manually to perform well on very specific types of objects, but have to be rebuilt for other objects. They are little robust to shape and size variations, as well as intensity variations within an image or across images, which are all frequent in cytometry images. Finally, as most of them work at the level of connected components, they are not meant to segment clustered objects.

D. Improvements

Even though the original definitions of the operations can be implemented as such, the algorithms can be improved, especially for large images. Fast implementations of the dilation, erosion, opening and closing are described in [30]. Fast algorithms for grayscale reconstruction are detailed in [179].

II.2. Watershed

A. Original definitions

Considering an image as a landscape, the watershed transform can be pictured as a flooding process. Starting from specific pixels, called *markers*, water rises gradually in the landscape. Each valley being flooded is called the *catchment basin* of the marker. When two catchment basins come in contact, their connections are labeled *watershed lines*. The flooding process continues as if dams were build on the watershed lines, preventing the actual merging of basins. The process stops when either the whole image is segmented, or the water level reaches a given height (the pixels above it are labeled as background). The watershed by immersion algorithm is reproduced in Appendix A.2, page 131. Mathematical definitions can be found in [14, 47], along with the links between watershed, skeleton by influence zones and Voronoi diagrams. Detailed watershed definitions, algorithms and analyses are in [144].

B. Strengths

A major feature of the watershed is that it is quick to implement, and does not need any parameter: there is no tuning to do before using it. Regarding its complexity, it runs in linear time, and its memory requirements are one temporary image, one array storing sorted pixels, and a queue. As a result it is fast and cheap.

C. Weaknesses

The main issue is to preprocess the image to produce the correct number of markers in the right places. Basically, the robustness of the watershed depends greatly on the robustness of the marker-finding preprocessing. An edge map often contains too many edges, not fully connected: this creates still too many basins,

with possible leaks. The distance transform is convenient to find markers within convex objects, but finds too many markers within concave objects.

Also, the watershed poorly detects low contrast boundaries [55]: this is inherent to the immersion process. Similarly, when a plateau happens to be a boundary between two basins, it is not properly segmented; however, this seldom happens with cytometry images.

Finally the watershed transform does not include any prior knowledge on the objects to segment. This is the inevitable drawback of any parameter-free segmentation method, and may be a significant issue for robustness.

D. Improvements

The weaknesses mentioned above are well-known, and several methods have been developed to address them.

Preprocessing: Finding the correct number and location of the markers is crucial for the segmentation results, and has to be done beforehand. Originally all local minima were used, causing severe oversegmentation. Alternatively, markers may be placed manually, or found automatically during preprocessing. Two examples of markers are the h-domes found by geodesic reconstruction [55] (see Section II.1, Shape extraction), and the maxima of the distance transform on thresholded images [104]. A combination of them is given by Lin [98]. Using the distance values $D(x, y)$ and the gradient values $G(x, y)$ (ranging from G_{min} to G_{max}), the quantity:

$$D'(x, y) = D(x, y) \cdot \exp\left(1 - \frac{G(x, y) - G_{min}}{G_{max} - G_{min}}\right) \tag{II.2.1}$$

is assigned to the pixel (x, y). The resulting image is inverted, and has the following property: it has high values near the boundaries of components, and also where the gradient is high; conversely, it has low values at the centre of components and in regions of low variations of intensities. With these properties, this method can find reliable markers for isolated or slightly touching convex objects, but not for concave objects.

Postprocessing: over-segmentation can be reduced by merging segmented regions. Using the immersion metaphor, it consists in removing some of the dams to merge some basins. To select which basins to merge, one way consists in evaluating the edges between two neighbouring regions [71]. Various criteria can be defined, using the range of intensity or gradient values along the edge. Another way is to measure some similarity between neighbouring regions, and merge the

most similar regions. The following issue is to decide when to stop the region-merging process. This may be done after a fixed number of merges [160], or when all regions meet some predefined quality criteria, e.g. based on their circularity. Overall this approaches introduces several parameters, and is often used ad-hoc.

Hierarchical watershed: this method, detailed in [47], also aims at reducing oversegmentation. The watershed transform is applied to the same image several times with a decreasing number of markers. After each segmentation, the depths of the basins are measured (defined as the difference between the minimum value inside a basin and the minimum value on its edges). Then, the markers of the shallowest basins are removed from the set of markers, and a new watershed transform is performed. After several iterations, a multi-scale or hierarchical segmentation of the image is obtained. The edges still present at coarser scale are considered more reliable. However, images at coarse scales tend to show a mixture of oversegmented and undersegmented objects. As a result, this method is more appropriate as a helper tool to assist a final manual segmentation than as part of a fully automatic tool.

Hierarchical watershed is actually different from *iterative watershed*, as defined in [105]. The latter also consists in performing several watershed, but uses the watershed lines as extra markers for the next watershed segmentation. The resulting lines can be interpreted as soft boundaries between the centre of an object and its boundaries. It is used in [105–107] to segment single objects, in a context where markers are easier to find than boundaries. This is different from cytometry, where reliable markers are usually more difficult to find than reliable boundaries.

Local watershed operators: this is also based on successive watershed transforms, but here each one is only applied locally around the markers. It is detailed in [171]. Starting from a set of markers, the watershed transform by immersion is applied, defining regions called *layer-0*. When water reaches a local edge (a pixel with an unvisited neighbour of lower intensity), a watershed border is drawn to stop the extension of layer 0, but then the corresponding neighbouring region is filled by watershed – and called layer-1. The process is applied to fill the layer-1 neighbouring regions, defining layers-2 regions. This method is meant to segment a wider neighbourhood of selected markers. As it also results in oversegmentation, region-merging post-processing needs to be applied.

Viscous watershed: this improvement presented in [177] is designed to segment objects with low contrast boundaries or with missing boundaries. In keeping

with the immersion metaphor, the liquid used is replaced by either oil, for blur, or mercury, for missing edges. Instead of modifying the watershed implementation to simulate viscous immersion, the authors present a way to preprocess the image to get equivalent results with the standard immersion algorithm. For the oil flooding, each level set h of the image f (*i.e.* the sets of pixels having the same grey value h) is closed with a disk-shaped flat mask of radius $r(h)$, decreasing with h. The resulting images $closure_h$ have two values, 0 and h. They are combined to define the smoothed image g: $g(x,y) = \max_h\{closure_h(x,y)\}$. For the mercury flooding, a gray value $t \geq 0$ is added to all pixels in f; the vertically translated image, noted $f + t$, is closed with a disk-shaped flat mask of radius $r(t)$ decreasing with t, resulting in an image noted $closure_t$. The final result g is computed as: $g(x,y) = \min_t\{closure_t(x,y)\}$. For both the oil and mercury flooding, the standard watershed transform is applied to g. This improvement is not quite adapted to our images, where finding the correct number and location of markers is more difficult that finding the correct boundaries.

Prior knowledge: there have been several attempts to include prior knowledge in the watershed transform: unavoidably, such methods are specific to the type of object to segment. In [98], Lin *et al.* present a post-processing step for nuclei segmentation. Several features are measured on the segmented regions, from eccentricity to texture. A supervised training phase extracts features and builds statistical models of them. Then the objects segmented by the watershed are compared to the models, and assigned a confidence measure. Edges are removed if the merged objects have a higher confidence than the separated ones. Actually, in this method the prior knowledge is not part of the watershed, but of the region-merging post-processing.

A revised watershed algorithm that includes prior knowledge was published in [55]. Using supervised learning, a function is build to evaluate the probability of having an edge between two neighbouring pixels, given the label of one of them. This function is then used in the flooding process, to decide which pixels should be investigated in each iteration and in which order. This method is illustrated in the case of MR images. It is difficult to adapt it to our context: the variations of appearance, geometry and concentrations make the selection of a training set difficult.

II.3. Active contours

Active contours, also called snakes or deformable models, appear in a variety of ways in the literature. Extensive reviews can be found in [90, 109, 193]. The idea they are based on consists in fitting an estimate of the object boundaries to the image, using at the same time the shape of the current estimate and the image values. Contours do not perform a complete segmentation of the image, but are meant to isolate the objects of interests: labeling all the image pixels is then straightforward.

A contour is initially created near the object boundaries: this is done manually or after a preprocessing step. It is then fitted to the object using various influences. Using the generic terms presented by Lehmann *et al.* [90], *contour influences* control the shape of the contour regardless of the image values (often called internal force or energy), while *image influences* adjust local parts of the contour to the image values regardless of the contour geometry (referring to external or image force or energy). The third type of influence, namely user-defined attraction or rejection zones, is of little relevance in applications requiring automation. These influences are combined, most of the time linearly, with parameters weighting their relative importance. The contour is locally extended, shrank, or remeshed, until it stabilises. Its final position defines the borders of the segmented region.

Active contours have been referred to with various adjectives, depending on the way they are stored and used (parametric, geometric, geodesic active contours, B-snakes, GVF-snakes, T-snakes, etc.). However, there are no standard definitions of these adjectives, even some contradictions. In this chapter, we consider two types of active contours, and name them parametric and geometric, depending on the way they are stored. Parametric contours are stored as sets of vertices, while geometric contours are stored as continuous curves. Also, we distinguish between energy-based and force-based influences. Energies are scalar values defined over the image, based on the image values and the contour's current

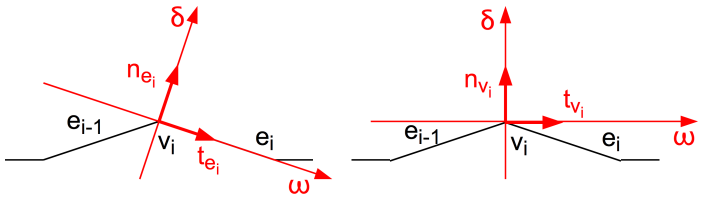

Figure II.3.1: *Two systems of coordinates at a vertex v_i. Left: edge-based coordinates. Right: vertex-based coordinates.*

geometry; vertices are moved in a way to reach minimum energy values. Forces are vectors defined at each vertex, and directly define the next movement of the vertices; they are also functions of the image values and the contour's current geometry.

It is to be noted that geometric active contours are often implemented as level sets in the literature [192]. However, as they are two different segmentation methods, we decided to devote distinct sections for them.

A. Original definitions

Contour encoding: *Parametric active contours* are deformable and remeshable polygons. In the literature, they are often noted as continuous curves $v(s) = (x(s), y(s)), s \in [0, 1]$. However, this notation is only meant to simplify the mathematical explanations of energy minimisation: the contours are actually implemented as polygons, not as continuous curve. Let V be the set of n vertices $v_i = (x_i, y_i)$; for convenience, we use cyclic indexing $v_0 = v_n$. Let $e_i = v_{i+1} - v_i$ be the edge between v_{i+1} and v_i. Two sets of coordinates can be defined at each vertex, as illustrated in Figure II.3.1. We use the subscript e_i for *edge-based* coordinates, and the subscript v_i for *vertex-based* coordinates. Let n_{e_i} and t_{e_i} be the external normal and tangent vectors at the edge e_i, defined as:

$$t_{e_i} = \frac{e_i}{\|e_i\|}\ ,\ n_{e_i} = \begin{pmatrix} 0 & 1 \\ -1 & 0 \end{pmatrix} \cdot t_{e_i} \tag{II.3.1}$$

(supposing the vertices are numbered anti-clockwise). Let n_{v_i} and t_{v_i} be the external normal and tangent vectors for vertex v_i, defined as:

$$n_{v_i} = \frac{n_{e_i} + n_{e_{i-1}}}{\|n_{e_i} + n_{e_{i-1}}\|}\ ,\ t_{v_i} = \begin{pmatrix} 0 & -1 \\ 1 & 0 \end{pmatrix} \cdot n_{v_i} \tag{II.3.2}$$

Each pair of vectors (t_{e_i}, n_{e_i}) and (t_{v_i}, n_{v_i}) at vertex v_i defines a referential in which each pixel of the image has unique coordinates (ω, δ). The original coordinates (x, y) can be computed with the formulas:

$$(x, y) = \omega \cdot t_{e_i} + \delta \cdot n_{e_i} \text{ or } (x, y) = \omega \cdot t_{v_i} + \delta \cdot n_{v_i} \tag{II.3.3}$$

Geometric active contours are defined as continuous curves: their points $v(s) = (x(s), y(s))$ are parametric functions of the arc length s of the curve. They are initialised as a set of discrete points, which are then either interpolated or approximated with a continuous function. Samples of this function are submitted to various influences, moved accordingly, and used to define a new continuous function, by interpolation or approximation. This process is performed iteratively until stabilisation [146]. The standard way to store a continuous function with a finite number of parameters is to project it on a chosen family of functions. Two families frequently used in cytometry are the Fourier basis and the cubic B-splines. See Appendix A.3 page 131 for details. Other representations can be used, using the *sinc* function for example [70], but will not be discussed here.

Contour influences: They control the shape of the contour locally. Given the typical shapes of nuclei, contour influences should enforce smoothness and local roundness.

The original *contour energy* used by Cohen [37] for parametric active contours combines the first two discrete derivatives of v:

$$v'_i = \frac{1}{h}(v_i - v_{i-1}) \ , \ v''_i = \frac{1}{h^2}(v_{i-1} - 2v_i + v_{i+1}) \tag{II.3.4}$$

where h is the spatial sampling rate (corresponding to the distance between two vertices). In the case of geometric active contour, the derivatives can be computed formally and continuously. When using Fourier parameters, formulas to compute the gradient can be found in [164]; for splines on a uniform sampling, see [20]. The final formulas are reproduced in Appendix A.3 page 131. The contour energy is defined as:

$$E_{contour} = \alpha \sum_{i=0}^{n-i} \|v'_i\|^2 + \beta \sum_{i=0}^{n-i} \|v''_i\|^2 \tag{II.3.5}$$

The first term, called *tension*, ensures that vertices are evenly spaced around the contour, while the second term, *stiffness*, ensures that consecutive edges are collinear. The parameters α and β control their relative importance.

The most common *contour forces* are the first two derivatives of v [114, 193], and the pressure force introduced by Cohen in the balloon model [37]:

$$F_{tension}(i) = v'_i \ , \ F_{stiff}(i) = v''_i \ , \ F_{pressure}(i) = k \, n_{v_i} \tag{II.3.6}$$

where k is a constant, positive for expanding pressure and negative for shrinking pressure. The contour force is defined as a linear combination of them:

$$F_{contour}(i) = \alpha \, F_{tension}(i) + \beta \, F_{stiff}(i) + \gamma \, F_{pressure}(i) \tag{II.3.7}$$

Image influences: They are meant to drive the vertices toward the object's boundaries, so they have to be designed according to relevant features.

To drive a vertex toward a grayscale value f_{target}, a possible *image energy* is:

$$E_{image}(x,y) = \mu \cdot (f(x,y) - f_{target})^2 \tag{II.3.8}$$

where μ is a weighting parameter. The value f_{target} can be fixed for the whole image, or can be a function of the contour. For example it can be a percentage of the intensity at the centre of the contour [35]: $f^t_{target} = 0.7 f(v^t_{centre})$ where $v^t_{centre} = \frac{1}{n}\sum_{v \in V^t} v$. Energies to drive vertices towards regions of high intensity variations can be defined as:

$$E_{image}(x,y) = \mu \cdot \phi(\|\nabla f(x,y)\|) \tag{II.3.9}$$

where ϕ is a decreasing function, such as $\phi(t) = -t^2$, $\phi(t) = e^{-t}$, or $\phi(t) = \frac{1}{1+t}$. If a set of edges is already available, an image energy based on the corresponding edge map can be used to drive a contour to these edges [88]. An energy driving a contour towards a set of strokes is detailed in [119]. Any other energy can be devised according to the characteristics of the objects to segment: it simply has to be minimum at the objects' boundaries. Incidentally, some energy minimisation algorithms only use the gradient of the energy function. Whether to compute the energy (and its gradient) on the whole image before fitting the contour, or to compute it only when needed during the minimisation, depends on the memory available and the processing time desired.

Image forces can be derived from image energies, using the formula:

$$F_{image}(i) = E_{image}(x_i, y_i) \cdot n_{v_i} \tag{II.3.10}$$

Another image force uses on the gradient vector flow $g(x,y)$ [193]:

$$F_{image}(i) = \mu \cdot g(x_i, y_i) \tag{II.3.11}$$

with μ acting as a weighting parameter (see Section II.1, Image Transforms, for details on GVF computation).

These forces only use image information located around the vertices. Other image forces are based on a wider range of data. The model presented in [18, 19] uses image information around the edges, before transmitting it to the vertices. The neighbourhood of e_i is a rectangle parallel to (t_{e_i}, n_{e_i}), containing the pixels of coordinates $0 \leq \omega \leq \|e_i\|$ and $-\delta_{max} \leq \delta \leq \delta_{max}$ (see Figure II.3.2, left). The pixels closer to the edge are given more importance, by means of a multiplicative weight $k(\delta) = 1/\delta$ for $\delta \neq 0$ and $k(0) = 0$, or any other function with similar shape. The image force applied to the edge e_i is:

$$F_{image}(e_i) = \mu \cdot \sum_{\omega=0}^{\|e_i\|} \sum_{\delta=-\delta_{max}}^{\delta_{max}} k(\delta) \cdot f(\omega \cdot t_{e_i} + \delta \cdot n_{e_i}) \cdot n_{e_i} \tag{II.3.12}$$

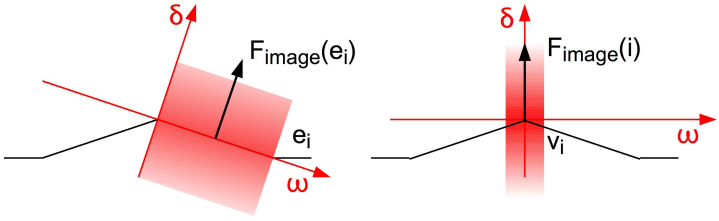

Figure II.3.2: *Image forces at an edge and at a vertex.*

where μ is a weighting parameter. The resulting image force applied to the vertex v_i, belonging to e_i and e_{i-1}, is:

$$F_{image}(i) = F_{image}(e_i) + F_{image}(e_{i-1}) \tag{II.3.13}$$

A similar technique is described in [146]. Instead of using image values around edges and transferring them to the vertices, the image values are scanned directly around a vertex. This time, the neighbourhood used is a rectangle centered on v_i, parallel to (t_{v_i}, n_{v_i}), containing the pixels of coordinates $-\omega_{max} \leq \omega \leq \omega_{max}$ and $-\delta_{max} \leq \delta \leq \delta_{max}$ (see Figure II.3.2, right). Using the same function $k(\delta)$ and parameter μ as above, the image force at vertex v_i is:

$$F_{image}(i) = \mu \cdot \sum_{\omega=-\omega_{max}}^{\omega_{max}} \sum_{\delta=-\delta_{max}}^{\delta_{max}} k(\delta) \cdot f(\omega \cdot t_{v_i} + \delta \cdot n_{v_i}) \cdot n_{v_i} \tag{II.3.14}$$

Contour fitting Once the contour and image influences are designed and the contour initialised, it has to be fitted to the image. Using energies, this amounts to minimising the total energy:

$$E_{total} = E_{contour} + E_{image} \tag{II.3.15}$$

This can be done iteratively with gradient descent method: moving each vertex v in the direction given by $\delta v \propto -\frac{\partial E_{total}}{\partial v}$ will progressively decrease the total energy. It is shown [69] that this amounts to the quantity:

$$\delta v_i = \alpha v_i'' - \beta v_i'''' - \nabla E_{image}(v_i) \tag{II.3.16}$$

The contour is moved iteratively, as $v_i^{t+1} = v_i^t + \delta v_i$, until all the δv_i are small enough. An efficient method to compute these iterations is presented in [37, 69]. It is a semi-implicit method, consisting in moving all the vertices based only on the image energy, and then updating their new positions using the contour energy. The previous equation can be written as:

$$\delta v_i = \frac{\alpha}{h^2}(v_{i-1} - 2v_i + v_{i+1}) - \frac{\beta}{h^4}(v_{i-2} - 4v_{i-1} + 6v_i - 4v_{i+1} + v_{i+2}) - \nabla E_{image}(v_i) \tag{II.3.17}$$

where h is the space between two consecutive vertices. Let $x^t = (x_0^t \cdots x_{n-1}^t)^T$ and $y^t = (y_0^t \cdots y_{n-1}^t)^T$ be the vectors of the contour coordinates; let e_x^t and e_y^t be the n-dimensional vectors containing at location i the x and y coordinates of $-\nabla E_{image}(v_i^t)$; finally, let τ be the time step between two iterations. The evolution of the contour is given by the linear equations:

$$\begin{cases} (I_n + \tau A)x^{t+1} = x^t + \tau e_x^t \\ (I_n + \tau A)y^{t+1} = y^t + \tau e_y^t \end{cases} \tag{II.3.18}$$

where I_n is the identity matrix of size n, and A a cyclic symmetric pentadiagonal banded matrix:

$$A = \begin{pmatrix} a & b & c & 0 & \cdots & c & b \\ b & a & b & c & 0 & \cdots & c \\ & \ddots & \ddots & \ddots & \ddots & & \\ b & c & 0 & \cdots & c & b & a \end{pmatrix} \tag{II.3.19}$$

where $a = 2\alpha/h^2 + 6\beta/h^4$, $b = -\alpha/h^2 - 4\beta/h^4$, and $c = \beta/h^4$. $I_n + \tau A$ can be inverted efficiently [34,37,69]. The iterations are stopped when $\max_{0 \leq i < n}\{\|v_i^{t+1} - v_i^t\|\} < \varepsilon$.

Using forces, the contour-fitting process is more straightforward than with energies. At iteration t, the contour and image forces are computed at vertex v_i, added, resulting in a single vector $F_{total}(i)$. Then, the most frequent formula to compute the movement of the vertex is:

$$v_i^{t+1} = v_i^t + F_{total}(i) = v_i^t + F_{image}(i) + F_{contour}(i) \tag{II.3.20}$$

Physically, this corresponds to the movement of a zero-weighted object in a viscous medium. In a more complex way, Lobregt [100] uses the forces to modify the vertices' accelerations, then updates their velocities, and finally their positions. This requires special care in designing the forces, to ensure that both velocities and accelerations are zero when the contour reaches the object boundaries.

B. Strengths

Active contours use prior knowledge on the object's shape and local image information. As their topology is enforced during the segmentation, they can segment objects with missing boundaries. Reducing the relative weight parameter of image influences increases the contours' robustness to noise.

For cytometric applications, the contour influences presented here are well adapted for cells and nuclei borders, while the flexibility of the image energy allows the specification of a variety of boundary features.

Regarding the mathematical nature of influences, using energies ensures by

construction that the final contour lies at a local energy minimum. On the other hand, vector force-based influences can encode more information than scalar energies. In addition, as it doesn't require differentiation of the external influence, it makes the design of influences more flexible. Also, the force-based method of fitting is faster than with energy.

Finally, each contour encoding has its own strengths. Parametric contours are straightforward to define, initialise, move and remesh. Conversely, geometric contours benefit from being continuous. Unlike parametric contours, the normals are naturally defined, which makes the definition of internal influences more robust to the contour geometry. Also they can be sub-sampled at chosen arc lengths, regular or not. The sampling rate does not influence the resolution of the curve, which is always stored as continuous. In particular, sub-pixel sampling can be used to compute image influences accurately.

C. Weaknesses

A major weakness of active contours is the delicate tuning of all the parameters weighting which influences are more significant. Their values and order of magnitude can be very different, but there is no rule to choose them. This makes their tuning little intuitive and long to perform manually, by trials and errors. In [37], the author reports good results for α and β of order of magnitude h^2 and h^4 respectively. This simply amounts to removing the factor $1/h$ in the definitions of derivatives, but is not a guideline for tuning. In [88], Larsen *et al.* present a method to estimate all the parameters beforehand, reducing manual tuning. However, their formulas are very specific to the formalism they use, and in particular require an edge map and prior knowledge about the amount of missing edges.

Also, active contours have to be initialised beforehand. It is a similar issue as finding markers for watershed. However, in addition to the location of the contour, the positions of all its vertices have to be specified.

A general limitation of contours is their fixed and basic topology. However, this is hardly an issue in cytometry, where the objects of interest tend to have simple topologies.

Two topological problems affect all active contours. *Self-crossing*, or the intersection of edges, can happen when two distinct part of a contour are attracted by the same image region, or when neighbouring vertices have radically different moves for a few iterations. Secondly, *vertices clustering* happens when vertices gather around the same image feature, resulting in very short edges where the contour influences have unreliable values. This second effect is reduced for geometric contours, due to the resampling of vertices at every iteration, but still

happens.

As a contour only inspects the image locally, with no mechanism for global minimum search, it can be trapped in a local minimum. Reducing the number of local minima requires a careful design of image influences, but it is generally not possible to ensure single minima at the objects' boundaries on all images. This problem of local search is inherent to all active contours; it is more critical with energy-based contours though, as the design of image influences is restricted to the use of scalar values. Force-based influences do not explicitly ensure minimisation – a notion which is anyway more relevant to a scalar field than a vectorial field.

Contour energies, in their original definitions, tend to shrink and flatten objects. Yet the energy minimisation process is highly dependent on their expression, which makes other contour energies difficult to implement.

Finally, parametric contours generally require frequent re-meshing: this is done by splitting edges longer than a threshold value into two, and merging short edges. This may have a significant computational cost in cytometry if many contours are used on an image. Geometric contours have a high computation cost at every iteration, during interpolation.

D. Improvements

Contour energy: Alternatives to the two original contour energies are presented in [74,132,188], and briefly described below. They are all meant to control the contour's curvature without the shrinking and flattening side effects mentioned above.

In [188], Williams and Shah compare five methods to compute the curvature at vertex v_i of a polygon: the variation of the angles around v_i, the curvature κ of a parametric curve $v(s)$, the norm of the v'', the difference between edge vectors, and the difference between normalised edge vectors. The curvature chosen can replace the stiffness presented above. However, there is no rule to decide which one to choose, and they have different values and orders of magnitude: changing the curvature definition requires a different set of parameter values.

In [132], Perrin and Smith presents a method to replace tension and stiffness, and to reduce vertices clustering. It is done by moving vertex v_i towards the perpendicular bisector of its two neighbours v_{i-1} and v_{i+1}, so that the angle $v_{i-1}, \widehat{v_i}, v_{i+1}$ is the average of $v_{i-2}, \widehat{v_{i-1}}, v_i$ and $v_i, v_{\widehat{i+1}}, v_{i+2}$. This way, vertices are regularly spaced and the angles between the edges vary smoothly. This model still requires a pressure term though.

The contour energy presented by Kang [74] is meant to reduce self-crossing

and improve smoothness. It is defined as:

$$E^t_{contour} = \alpha \sum_{i=0}^{n-1} E^t_i \text{ where } E^t_i = \|(v_i^{t+1} - v_i^t) - (v_{i-1}^{t+1} - v_{i-1}^t)\| \tag{II.3.21}$$

The contour energy is minimum when neighbouring vertices move in a similar way. This is implemented with an efficient dynamic programming technique [42, Chapter 16]. This model favors regular convex objects though; enforcing similar displacement is not adapted for concavities.

Contour forces: The traditional internal forces, tension and stiffness, are defined as discrete approximations of the first and second derivatives of curves. However, variable edge lengths and vertices clustering can make such approximations unreliable as measures of local curvature; besides, internal pressure force is not guaranteed to prevent shrinking. A different approach to compute the internal forces in presented by Lobregt and Viergever [100]. The curvature at vertex v_i is defined as: $c_i = e_i - e_{i-1}$, and the internal force is its projection on the normal vector e_{v_i}. In addition, the curvature is distributed over the neighbouring vertices, to prevent regions of constant curvature from shrinking. The internal force at vertex v_i is defined as[1]:

$$F_{in}(v_i) = \left(-\frac{1}{2} f_{in}(v_{i-1}) + f_{in}(v_i) - \frac{1}{2} f_{in}(v_{i+1})\right) n_{v_i} \tag{II.3.22}$$

where $f_{in}(v_i) = c_i \cdot n_{v_i}$. This method reduces the number of parameters while ensuring a control on the local curvature along the contour. The curvature definition is ad-hoc though, and the parameters weighting the local distribution of internal forces are arbitrary. Overall, this method introduces extra parameters to the model.

The original pressure force [37] is constant throughout the contour fitting. As a result the other forces have to counter-balance it at the object boundaries, which may be an issue for their design. Alternatively, the *adaptive balloon force* by Luo *et al.* [101] reduces over time. It induces greater moves in early iterations, while it has a lesser influence later on, as the contour gets closer to the object boundaries. The rate of reduction is yet another parameter to tune though, and is dependent on the expected total number of iterations. The pressure variations may instead by driven by the contour location. This approach in taken by Ivins using *statistical snakes*. Assuming the object of interests has a Gaussian histogram, with mean μ and standard deviation σ, the pressure at vertex i is:

$$F_{stat}(v_i) = \gamma \left(1 - \frac{|f(x_i, y_i) - \mu|}{k\,\sigma}\right) \cdot n_{v_i} \tag{II.3.23}$$

[1]The formulas presented in [100] are based on the internal normal vector $\hat{r}_i = -n_{v_i}$, but this has no effect on the final expression of the force here, by linearity of the equations involved.

where γ is a weighting parameter and k is the number of standard deviations tolerated from the mean intensity before the pressure becomes negative. Incidentally, this pressure force is now an image influence. Using a single Gaussian model for objects' histograms, with known parameters, may cause robustness issues for large-scale cytometric applications though. This model is generalised by Fester *et al.* [52] and Abd-Almageed *et al.* [1], called *kernel snakes*. It requires a clear distinction between the histograms of foreground and background, which is not the case in our context.

Internal influence alternative for geometric contours: An improvement specific to geometric contours consists in using a variable sampling rate instead of internal influence. Interpolating points chosen with a low sampling rate will result in a smooth curve, potentially smoother than the original curve. This way, a low sampling rate corresponds to a high weight for internal influences, and conversely for a high sampling rate. In [20], Brigger *et al.* suggest using a multiple of the number of node points, and compare variable sampling rate with internal energies, reporting similar results. This replaces the weighting parameters by sampling parameters, which still have to be tuned.

In the same vein, Precioso *et al.* describe a way to approximate (as opposed to interpolate), the points with cubic splines, called *smoothing splines* [140, 141]. The idea is to impose a smoothness to the resulting curve, at the expense of approximating the sample points. A single parameter can be used to control the amount of smoothness required. However, the smoothing splines are defined only implicitly, as the solutions to a minimisation problem. A detailed algorithm to compute them is detailed in [140, 142]. A theoretical presentation of smoothing splines can be found in [175]. This method was published for tracking purposes, where convergence speed was more important than segmentation results, which is not the case in our context.

Image energy: The design of image energy can also be improved. Defining it as a 'scalar field' independent of the contour (such as an edge map) restricts the possible designs. Another approach is to define the image energies using the current contour position, and update them at every iteration of the fitting process. Let Ω_{in} be the inside of the contour and Ω_{out} the outside; the corresponding image energies $E_{\Omega_{in}}$ and $E_{\Omega_{out}}$ may have different definitions. This is of particular interest when the object to segment has a texture different from the background. This is used in the $DREAM^2S$ model [72]. As an example, the inner image energy

may be the variance of the pixel intensities:

$$E_{\Omega_{in}} = \frac{\sum_{(x,y)\in\Omega_{in}} (f(x,y) - \overline{f}_{\Omega_{in}})^2}{\sum_{(x,y)\in\Omega_{in}} 1} \tag{II.3.24}$$

where $\overline{f}_{\Omega_{in}}$ is the mean intensity value within the contour, while the outer image energy Ω_{in} may be zero, or the variance of outer pixel intensities, as done by Precioso [140]. In [184], Wang *et al.* use a similar method with the inner image energy:

$$E_{\Omega_{in}} = \sum_{(x,y)\in\Omega_{in}} (f(x,y) - T) \tag{II.3.25}$$

where T is a threshold value. As this formula is not normalised by the size of the contour, the external energy will have a greater influence as the contour grows; this can be seen as ensuring that the average pixel intensity is close to T, with a weight increasing as the contour grows. Another type of design consists in comparing the intensity histogram of the pixels in Ω_{in} with a reference histogram; the inner image energy is then designed to reduce the distance between the histograms. For more details, we refer the reader to [73]. Incidentally, the design of $E_{\Omega_{out}}$ is based on prior knowledge of the background, which is not always available: in particular its size, intensities and variations may be unknown. This is why Ω_{out} is often set to zero in the literature. In our context however, little information on the foreground and background textures is available, which makes this model unreliable.

Contour fitting: Other improvements are concerned with the contour fitting method itself.

A method to check that a contour is not trapped in a local minima consists in fitting two contours, one from inside the object, one from outside. These *twin snakes*, presented by Kerschner [75], should converge to the same boundary of the object and be parallel. Non-parallel parts of the contours are detected by high gradients of the distance between them. More fitting iterations are then performed for these parts only. The main issues are to detect which contour was trapped, and to initialise the outer contour so that it only contains one object of interest. This is a significant problem for segmenting numerous and touching objects, as in our context.

In [197,198], Xu *et al.* present a graph-cut method, which in particular ensures non self-crossing contours. At each iteration, the region surrounding the contour is turned into a graph, whose weights are sets according to the image energy. Graph-cut is applied to find a global minimum in this region. This global minimum defines the new position of the contour. A recent article presents general classes of functions that can be minimised by graph-cut [79]. Efficient algorithms

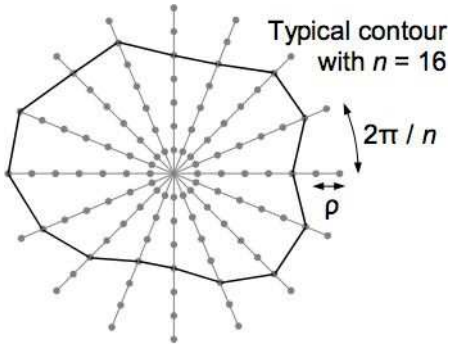

Figure II.3.3: *Polar grid used for certain active contours.*

for graph-cut can be found in [42, Chapter 27]. This method finds a global minimum in a local part of the image, and thus is still sensitive to local minima. Besides, it restricts the regions where the contour can evolve, thus making it more sensitive to its initialisation.

An alternative to the analytic fitting is to use a *genetic algorithm* to reduce the overall energy of a contour. In [8,9], Ballerini and Bocchi describe a contour in polar coordinates from its centre (x_c, y_c), regarded as a fixed seed point, with $v_i = (x_c + r(i)\cos(\theta_i), y_c + r(i)\sin(\theta_i))$, and $\theta_i = 2\pi i/n$. With these notations, a contour is encoded in a chromosome as $(r(0), \ldots, r(n-1))$, and its fitness is a decreasing function of its energy. Then, as for all genetic algorithms, cross-over and mutation rates have to be chosen, along with a way to create off-spring. Detailed descriptions of genetic algorithms can be found in [121, Chapter 7] [150, Chapter 20] [199]. Using a polar description of contours, any chromosome with positive values corresponds to a non-crossing contour. However, genetic algorithms are not guaranteed to converge, and include randomness as a core feature, which might not be desirable for robust clinical applications. Besides, only star-convex contours can be represented this way. Although this is enough to segment most objects in cytometry, in our application we expect non-star-convex nuclei.

With a similar polar representation of contours, only discrete, Bamford *et al.* present an efficient method of fitting, achieving energy minimisation in few iterations [10]. The contour is centred around a seed point (x_c, y_c) located anywhere within the object. The search space is then discretised around it. The possible locations of vertices are at angles $2\pi i/n$, with $i \in [0, n]$ integer, and at distance $d\rho$ with $d \in [d_{min}, d_{max}]$ integer, from the seed, where ρ is the radial step chosen for the discretisation (see Figure II.3.3). With these notations, the vertex v_i of a contour can only be located at: $v_i = (x_c + d_i\rho\cos(\theta_i)\,,\, y_c + d_i\rho\sin(\theta_i))$ with $\theta_i = 2\pi i/n$, for some $d_i \in [d_{min}, d_{max}]$ integer. The energy functions used are:

$$E_{contour}(i) = \left(\frac{v_{i+1} - 2v_i + v_{i-1}}{v_{i+1} - v_{i-1}}\right)^2 \,,\, E_{image}(i) = \phi(\|\nabla_i f(x_i, y_i))\|) \qquad \text{(II.3.26)}$$

where ϕ is a decreasing function, and ∇_i is the gradient of f computed in the direction θ_i. The total energy of vertex v_i is:

$$E_{total}(i) = \lambda E_{contour}(i) + (1 - \lambda) E_{image}(i) \tag{II.3.27}$$

where λ is a weighting parameter. Given the seed point, the contour is fully described by $(d_0, \dots d_{n-1})$. The fitting method consists in choosing the values d_i one by one, starting with $i = 0$, so that the energy is minimum at each vertex. A dynamic programming technique based on the Viterbi algorithm is used (see [42, Chapter 16]). The energy of vertex v_i is computed for every d_i and d_{i+1} (as d_{i-1} is fixed), and the value d_i chosen is one that minimises:

$$S_i(v_i, v_{i+1}) = \min_{d_i, d_{i+1}} \{S_{i-1}(v_{i-1}, v_i) + E_{total}(i)\} \tag{II.3.28}$$

A similar method is presented by Chen *et al.* [33]: they use the same polar representation, and a similar dynamic programming technique to fit the contour. The difference lies in the way to close the contour. One contour is fit for every possible position of v_0, and the one with the overall minimum energy is kept. A similar approach is presented by Xu *et al.* [196] for lung nodule segmentation, using expectation-maximisation and dynamic programming, with no mention of contours. These methods have two significant issues in our context. First, they can only segment star-convex objects. Second, they are restricted to non-touching objects.

An improvement for the speed of convergence is presented by Metzler *et al.* in [114]. It consists in *freezing* the edges that are stable, thus reducing the number of vertices to move in the next iterations. While this method may be useful in some applications, it will fail when an edge of the contour is stopped at a local spurious feature of the image. Experiments on our images show that it usually takes a few iterations for the internal forces to drive that edge out of a spurious local minima, but with that method it will stay and block its neighbouring edges.

Topology conservation: The following improvements aim at reducing self-crossing and vertices clustering.

The spreading of internal forces [100] described above smoothes the relative movements of vertices, thus reducing these risks. Similarly, external forces can be spread, as done by Ronfard [146]. The image energy computed at vertex v_i can be added to that of its neighbours, with a weight decreasing with their distances. These methods introduce further parameters though, and only *tend* to reduce the risk of self-crossing.

Another way to reduce clustering is to move a vertex v_i using only the force components parallel to n_{v_i} [100]. Also, the internal force can be designed to drive

vertices towards the centre of gravity of their neighbours. This is achieved in two dimensions by Pagador *et al.* [129], and in three-dimensions by Miller *et al.* [116]. It reduces the possible moves of vertices though, and can be detrimental to the segmentation of concave objects.

In case vertices clustering does happen, a common way to correct it consists in merging an edge e_i with one of its neighbours when $\|e_i\|$ is below a threshold, and creating a new vertex in its centre when $\|e_i\|$ is above another threshold. This requires a renumbering of vertices, and is usually performed after a certain number of iterations, to trade precision against computation time. Choosing the threshold values is another trade-off: smaller values allow a finer resolution of the contour, but reduce the effect of internal influences. A less computational intensive version, presented in [68], consists in doubling or halving the number of vertices when the mean length of edges reaches out the thresholds.

Self-crossing is intrinsically difficult to avoid. This problem is somehow inherent to contours: influences and movements are computed locally, but self-crossing is a global issue. The standard approach is to test if any vertex is inside the contour. Detecting if a point lies inside or outside a shape can be done with methods from computer graphics, such as scan lines. As it is a time consuming operation, it is usually performed only after a certain number of iterations. Once detected, it can be difficult to correct. Merging non-neighbouring edges would alter the contour's topology. Sudden moves of vertices sharply increase the contour influences locally, which may cause oscillations or divergence.

A different approach to control the contour shape was introduced by Hamarneh *et al.* [61]. The active contour, named *deformable organism*, is designed with an internal structure. Vertices are connected not only by edges, but also by a skeleton-like structure, made of 'internal edges'. Their lengths can vary within given ranges, depending on the variations allowed for the final shape. This method is a robust way to segment a specific shape that is know in advance, such as organs or brain structures, while allowing controlled variations. However, it may not be relevant for the objects usually found in cytometry, where no internal structure can easily be modeled with edges.

Topological changes: Although the fixed topology of contours is rarely an issue in cytometry, it is worth mentioning methods that were developed to handle topological changes during the contour fitting. They could be adapted for the segmentation of clusters, making it more robust with respect to the initialisation of contours. *Topologically adaptable snakes* presented by McInerney and Terzopoulos [108, 110, 111] evolve over an underlying grid, made of triangles. In short, after each iteration, the intersections between the edges and the grid define

the new contour vertices. This ensures a fairly regular distribution of vertices. In addition, the topology of the contour can be determined by scanning the grid cells containing contour edges, and counting the number of edges they contain. Self-crossing and contour intrusions can be detected efficiently, then contours can be easily split or merged. Splitting contours, by Lefevre *et al.* [89], are meant for tracking purposes, but could be adapted for cluster segmentation. When contour edges exceed a given length, they are divided into three parts. The contour is split at these parts if it makes its energy lower. While this may be desirable to make contours recover from a wrong initialisation, level sets are a more consistent framework to handle topological changes, as described in the next section.

Multiple contours: Finally, one important improvement for the segmentation of clustered object is the use of multiple contours that do not inter-penetrate. In [35], Clocksin introduces a new force. If vertex v_i is inside another contour, a *repulsive force* is applied to it, directed along $-n_{v_i}$ and proportional to the distance of v_i within that contour. The weight of this new force is yet another parameter to tune, and while it is desirable to correct for intruding vertices, sudden moves of one vertex tend to alter the evolution of the whole contour. An alternative is to use a force proportional to the area of overlap between the two contours. The *communicating snakes* described by Ballerini and Bocchi [9] are connected with spring-like forces, which keeps them at a fixed distance to each other. However, this requires many connections between vertices, and new parameters to tune the importance of these forces. It was introduced to segment bones, whose number and relative positions are known, but is less relevant in cytometry.

Prior shape knowledge: Internal influences tend to control the shape locally, but cannot be used to enforce global shape constraints. When prior knowledge on the whole shape is available, several methods have been presented to use it during the contour fitting.

Geometric contours are well suited for prior knowledge, since they are described globally as a continuous curve. Prior knowledge on the coefficients describing the curve can easily be obtained on a set of training shapes. In [164], Staib and Duncan describe how to include prior distributions in the fitting process. Besides, they introduce alternative Fourier parameters that encode the phase and amplitude of the Fourier components, and are less sensitive to relative rotations of components. A similar idea is presented by Szekely *et al.* in [168]: the distributions of Fourier parameters are stored during a training phase. A mean contour value is computed, and the deformations modes are extracted by princi-

pal component analysis of the covariance matrix of the Fourier parameters. After the training phase, a contour is fitted to the image, using the main deformation modes at first, then improving the resolution by introducing more deformations, in a coarse-to-fine approach. However, computing the deformations requires a reference in the images, from which the Fourier parameters can be normalised. This method is well-suited for brain scan images where landmarks can be manually placed, but is not convenient in our context.

Another approach to include prior knowledge, by Blake and Isard, is detailed in [15]. It consists in using a template shape Q_0, described as a continuous curve (such as a cubic spline), along with a *shape-space*, where each vector X corresponds to a deformation of the template. This assumes that the set of deformations needed to obtain any shape from the template are known and simple (e.g. Euclidian, affine), and applied to the whole shape. These restrictions are significant in cytometry, where objects can deform locally.

In a recent article [53], Foulonneau *et al.* compute Legendre moments on training shapes, and drive the contours towards these values. Legendre moments are affine-invariant, and thus adapted for the segmentation of objects with known shapes but varying pose. In our context however, nuclei show large variations of shapes, which makes the selection of a training set difficult and causes robustness issues.

A more flexible approach to include prior knowledge was developed by Cootes [38, 39], as Active Shape Models and Active Appearance Models, respectively ASM and AAM. These models are trained on a set of objects, initialised near an object in an image, and adjusted using both the underlying image content and the training shapes. The training of the two models is based on sets of landmarks positioned on the segmented objects. The landmarks' positions and the underlying textures are encoded as vectors. The distributions of these training vectors are then modeled with an appropriate parametric model. Using a Gaussian model, the mean vector and the eigen vectors of the covariance matrix can be computed easily. A mixture of Gaussian models can also be used, with an Expectation-Maximisation algorithm, as well as other methods, depending on the types of deformations to model [40, 41]. Once a parametric model is built on the training set, the active models are initialised near the objects, and fitted iteratively so that their geometry and the underlying texture falls within the model. While the general principles of ASM and AAM are similar, their implementations are different. ASM encode the geometric relations between the vertices and the underlying texture around each vertex, while AAM model the whole texture within the vertices. As a result, the fitting is performed locally around each vertex for ASM, and globally on the whole shape for AAM. Compared to active contours,

the model of the vertices' positions plays a similar role as the internal influences, and the model of the underlying texture, as the external influences. However, in the active model framework, the two models are encoded globally. As a result, a shape may have different local geometry and textures, which is not allowed in most active contours models. These models are well-suited for the segmentation of objects with consistent geometry and textures, such as faces or brain MRI images. In our context however, nuclei have very diverse textures and geometry. No landmark can easily be defined around or inside nuclei, and no corresponding points can easily be found between two nuclei. Also, clusters of nuclei cause extra variations of textures and geometry, and would require their own model.

Finally, an extension of geometric active contours consists in embedding the contour curve as a level set of a higher-dimensional function: this is the basis of level set segmentation methods, which are detailed in the next section.

II.4. Level sets

Mathematically speaking, the level set of a function $\Psi(x,t)$ is the subset of some of its arguments $\{x, \Psi(x,t) = C_0\}$ for a given constant C_0 and a chosen value for the other arguments t. A function $v(t)$ is *embedded* in a higher-dimensional function $\Psi(x,t)$ if it is a level set of Ψ, *i.e.* if there is a value C_0 so that $\forall t, v(t) = \{x, \Psi(x,t) = C_0\}$. The idea underlying the level set method of segmentation is to embed a function defining the object boundaries into a higher-dimensional function. This can be pictured with contours: at iteration t, the contour $v(t)$ is the level set $\{(x,y), \Psi(x,y,t) = C_0\}$ of a function $\Psi(x,y,t)$; that function has many other level sets $C_i \neq C_0$, more or less parallel to $v(t)$. A level set has to be initialised near the object boundaries, and is fitted iteratively to the underlying image, using image influences and internal influences. Since this is similar to contours, the two methods are often mixed in the literature – level sets are sometimes called *implicit active contours*. However, to avoid confusion between level sets and contours, we will refer to the level set C_0 as the *front* $v(t)$. For convenience, we set $C_0 = 0$:

$$v(t) = \{(x,y), \Psi(x,y,t) = 0\} \tag{II.4.1}$$

A segmentation with level sets is done in the following way. The front $v(t_0 = 0)$ is initialised, ideally near the object boundaries, and the whole embedding function $\Psi(x,y,t_0 = 0)$ is constructed, so that $v(t_0)$ is its level set $C_0 = 0$. Then, the values of Ψ are modified in each pixel (x,y) iteratively over t, using an equation of motion; as a result all the level sets of Ψ, in particular the front $v(t)$, are modified at each iteration. The process is stopped, ideally when the front $v(t)$ stands on the objects' boundaries.

Roughly speaking, each level set of Ψ is a set of pixels, on which Ψ has a given value. It is to be noted that only the front $v(t)$ is related to the contents of the image: it alone will eventually define the segmented objects. The other level sets of Ψ are meant to improve the convergence and the topology changes

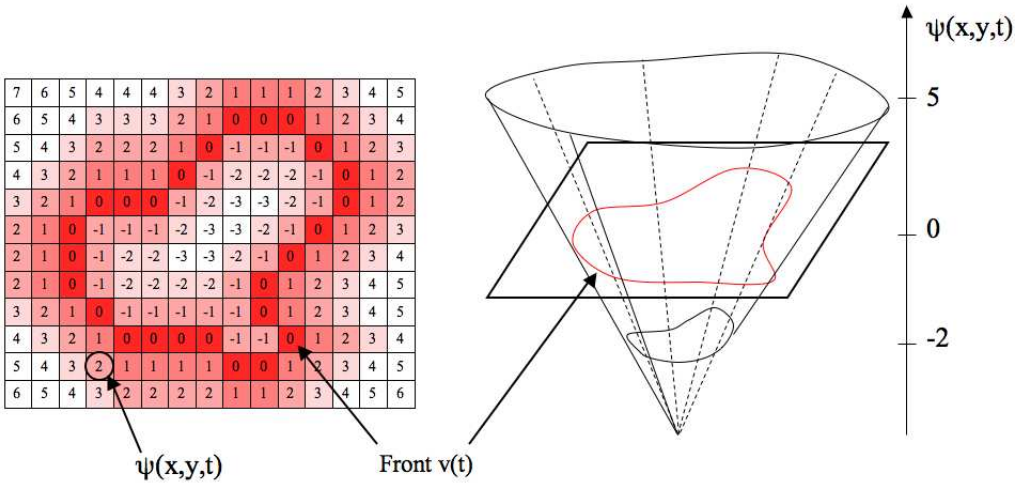

Figure II.4.1: *Illustration of an embedding function defined as a signed distance. Left: values of the embedding function* Ψ *discretised on the image pixels. Right: the same continuous embedding function* Ψ *shown in three dimensions. The front* v *is shown in red.*

of the front, but not to segment anything. Thus, the image influences are often computed for v only, and then *extended* to the other level sets.

A. Original definitions

Embedding function: The approach we use in this section is based on the work by Malladi *et al.* [103]. Once the front $v(t_0 = 0)$ is initialised, Ψ is defined as:

$$\Psi(x, y, 0) = \begin{cases} -dist(x, y, v) & \text{if } (x, y) \text{ is inside } v(0) \\ 0 & \text{if } (x, y) \text{ is on } v(0) \\ dist(x, y, v) & \text{if } (x, y) \text{ is outside } v(0) \end{cases} \quad \text{(II.4.2)}$$

where $dist(x, y, v)$ is the distance between (x, y) and $v(0)$. This definition stands whether v is discrete (e.g. a set of vertices) or continuous, and whether Ψ is defined as discrete (over all pixels of the image) or continuous. An illustration of Ψ is shown in Figure II.4.1. For a description of continuous curves using Fourier coefficients and cubic splines, we refer the reader to the previous section on geometric active contours.

Equation of motion: To control the evolution of Ψ over time, its derivatives are linked by the following equation, called equation of motion:

$$\frac{\partial \Psi}{\partial t}(x, y, t) + \hat{k}(x, y) \cdot (F_A + F_G(\kappa)) \cdot \|\nabla \Psi(x, y, t)\| = 0 \quad \text{(II.4.3)}$$

We now detail the terms introduced in the equation of motion.

The partial derivative of Ψ over time is meant to introduce a movement in Ψ.

For an iterative solution, it is approximated as:

$$\frac{\partial \Psi}{\partial t}(x,y,t) = \frac{\Psi(x,y,t+\Delta t) - \Psi(x,y,t)}{\Delta t} \tag{II.4.4}$$

where Δt is the time step, a parameter controlling the amount of change allowed for Ψ between each iteration.

$\hat{k}$ is the *extended speed function*. The (non-extended) speed function k is defined only for the pixels where the front stands, and encodes the image influence in the equation. However, since the same equation is used for all level sets of Ψ, k has to be extended to them, thus defining $\hat{k}$. The main constraint in designing k is that it has to be ideally zero at the objects' boundaries. Supposing the boundaries are characterised by high gradient, k can be defined as:

$$k(x,y) = \frac{1}{1+|\nabla f(x,y)|} \text{ or } k(x,y) = e^{-|\nabla f(x,y)|} \tag{II.4.5}$$

For more examples of image influences, we refer the reader to the previous section on active contours. Incidentally, in [103], Malladi *et al.* define k as above, using $\nabla G_\sigma * f(x,y)$ instead of $\nabla f(x,y)$. This simply amounts to smoothing f with a Gaussian filter of variance σ, which is one of many possible preprocessing. We consider that any relevant preprocessing was performed on f beforehand. Once $k(x,y)$ is defined, it can be extended in the following way, called *global extension*:

$$\hat{k}(x,y) = k(x',y') \tag{II.4.6}$$

where (x',y') is the point on the front v that is closest to (x,y).

The term F_A, standing for 'advection', is meant to expand or contract Ψ, similarly to the pressure force in the balloon model. It can simply be a constant scalar value c, positive for expansion and negative for contraction[1].

The term $F_G(\kappa)$, standing for 'geometry', is a scalar value depending on the curvature $\kappa = \kappa(x,y,t)$, defined as:

$$\kappa(x,y,t) = \operatorname{div}\left(\frac{\nabla\Psi(x,y,t)}{\|\nabla\Psi(x,y,t)\|}\right) \tag{II.4.7}$$

Using subscript notations for partial derivatives, *i.e.* $\Psi_x = \frac{\partial\Psi}{\partial x}(x,y,t)$, the curvature is computed as [103]:

$$\kappa(x,y,t) = -\frac{\Psi_{xx}\Psi_y^2 - 2\Psi_x\Psi_y\Psi_{xy} + \Psi_{yy}\Psi_x^2}{\left(\Psi_x^2+\Psi_y^2\right)^{3/2}} \tag{II.4.8}$$

[1]Expansion of Ψ means that each of its level set expands. Here, it corresponds to a decrease in the values of Ψ because it is shaped as a pit, not a mountain. Yet, the value added at each iteration is $-c : c \geq 0$ reduces the values of Ψ, thus expanding its level sets.

This expression includes a minus sign, simply because the term added to each iteration is actually $-\kappa$. F_G is similar to the contour influences presented above, and is usually meant to penalise high curvature in the level sets. In [26], Caselles *et al.* define it as $F_G(\kappa) = \kappa$.

Finally, the norm of the gradient of Ψ is:

$$\|\nabla\Psi(x,y,t)\| = \left(\Psi_x^2 + \Psi_y^2\right)^{1/2} \tag{II.4.9}$$

This term corresponds to the amount of change in the values of Ψ around the point (x, y); in other words, it is higher if level sets are closer to each other around (x, y).

Using these new notations, $\Psi(x, y, t + \Delta t)$ can be expressed as:

$$\Psi(x,y,t+\Delta t) = \Psi(x,y,t) - \Delta t \cdot \hat{k} \cdot (c+\kappa) \cdot \|\nabla\Psi\| \tag{II.4.10}$$

Each point (x, y) is assigned this new value, and may thus be on a different level set. This way, level sets may expand, shrink, and change topology.

Alternative equation of motion: A different equation of motion, derived from an energy minimisation view of the level set fitting, is sometimes used [81,94]. It is detailed by Caselles *et al.* [26,27]. In this model the extended speed function $\hat{k}(x, y)$ is called the *stopping function* $g(f(x, y))$: it is designed to be zero at the objects' boundaries. The equation controlling the evolution of the level set is:

$$\frac{\partial\Psi}{\partial t} = \|\nabla\Psi\|\mathrm{div}\left(g(f)\frac{\nabla\Psi}{\|\nabla\Psi\|}\right) + c\cdot g(f)\cdot\|\nabla\Psi\| \tag{II.4.11}$$

where c is a constant velocity, which in this context should be negative for an expansion of Ψ. By developing the divergence of a product, and using the definition of curvature $\kappa = \mathrm{div}\left(\frac{\nabla\Psi}{\|\nabla\Psi\|}\right)$, the equation is equivalent to:

$$\frac{\partial\Psi}{\partial t} = (c+\kappa)\|\nabla\Psi\|\ g(f) + c\ \nabla g(f)\cdot\nabla\Psi \tag{II.4.12}$$

This model is often referred to as *geodesic active contour* or *implicit geodesic active contour*. In comparison, the model described first in this section is sometimes called *implicit geometric active contour*, and with this new notation, the equation of movement II.4.3 would be written as:

$$\frac{\partial\Psi}{\partial t} = g(f)\ \|\nabla\Psi\|\mathrm{div}\left(\frac{\nabla\Psi}{\|\nabla\Psi\|}\right) + c\ g(f)\|\nabla\Psi\| \tag{II.4.13}$$

A general equation of motion, by Kuhne *et al.* [82], links these two models:

$$\frac{\partial\Psi}{\partial t} = a(f)\ \|\nabla\Psi\|\mathrm{div}\left(b(f)\frac{\nabla\Psi}{\|\nabla\Psi\|}\right) + c\ g(f)\|\nabla\Psi\| \tag{II.4.14}$$

where $\{a, b\} = \{1, g\}$. This allows a general analysis of the level set models.

Front location: The final step of the iteration is to identify the new location of the front, which corresponds to solving the equation $\Psi(x, y, t+\Delta t) = 0$ for (x, y). If Ψ is computed discretely over the pixels, one way to solve it is to interpolate the values linearly between pixels, as in the Algorithm 1 in [103]. In brief, each pixel (x, y) and its four closer neighbours are considered. Among these five pixels, if the maximum value of Ψ is positive and the minimum value negative, then the front should stand between the two pixels where these values are reached. The pixel closer to the front is found by linear interpolation of these two pixels.

The iteration ends when the new values of Ψ are computed for all pixels, and the new location of the front is obtained. In the next iteration a new speed function k will be defined over the new front. The process continues until the front is stationary.

B. Strengths

With the combined use of internal and image influences, level sets allow the segmentation of objects with missing boundaries and noise. The general definition given above can be used for either discrete or continuous level sets, depending on the resolution and accuracy required for the final segmentation, and the affordable computation time. With a continuous description, the curvature and normal are properly defined, thus more robust to the local geometry of the curve.

Another strength of level sets is the front's ability to change topology in response to image contents. The front may split, merge, have holes created or filled, with no extra dedicated step in the algorithm detecting and handling such changes, as with contours. This may be a useful feature when segmenting clustered objects.

Also, as the embedding function Ψ is potentially defined over the whole image, the final segmentation is less dependent on the initialisation of the front.

C. Weaknesses

The high computational time to process level sets is a general weakness. In particular, the evaluation of the local curvature requires the computation of many partial first- and second-order derivatives of the embedding function, at every point and every iteration. Similarly, the extension of the speed function has a significant cost at each iteration.

Also, the flexible topology may be an issue for some applications: there is no guarantee that the final segmentation will have a shape or topology similar to the initial front. Thus, with the original definitions it is actually difficult to include and keep prior knowledge concerning the global shape of the objects of interest.

D. Improvements

Computation time: There are several ways to improve significantly the computation time, in particular the narrow band, the fast marching and the Hermes methods. In our context, computation time is not a significant issue. We list these improvements for completeness.

The *narrow band* method [2,103] is based on the following observation. Only the front is needed for segmentation, and distant level sets have little influence on its evolution; yet they increase the computation time. By restricting the embedded function to a few level sets, forming a narrow band around the front, the final result will be little affected. This require care when evaluating the partial derivatives at the borders at the band [2]. Since only the level sets within the band are modified, the front can only be located within in: this may restrict its topology [103]. A solution is to re-initialise the band regularly, around the new position of the front. At the latest, it must be re-initialised when the front reaches the borders.

A further speed improvement of the narrow band technique consists in computing the extended speed function $\hat{k}$ in the same way as k [103]:

$$\hat{k}(x,y) = \frac{1}{1 + \|\nabla f(x,y)\|} \tag{II.4.15}$$

The *fast marching* technique is based on a somewhat different vision of level sets, called *front propagation* [155]. It may be pictured as a wave v traveling over the image. In this context, the embedding function of v is $T(x,y)$, whose value is the time at which v reached the point (x,y). v is still called $front$, but is now the outside level set of the embedding function T:

$$v(t) = \{(x,y), T(x,y) = t\} \tag{II.4.16}$$

It is to be noted that the values of T are not modified once defined: T can only expand. However, its geometry as a surface may influence the evolution of the front in a richer way than was possible with active contours. Once stabilised, the position of the front defines the segmented objects. This time, the equation describing the evolution of the front boils down to:

$$\|\nabla T(x,y)\| \cdot F(x,y) = 1 \tag{II.4.17}$$

F is a term controlling the evolution of the propagation. It has to be positive, to prevent the front from moving back, and large at the objects boundaries, to stop the front there. An exponential function ensures both constraints:

$$F(x,y) = \exp \|\nabla f(x,y)\|^2 \tag{II.4.18}$$

The design of F depends on the characteristics of the objects to segment. More examples are given by Schupp *et al.* [153]. F may contain terms depending on the image intensity or gradient, and on the local front geometry. For information, the curvature of T is defined as [155]:

$$\kappa(x,y) = \frac{T_{xx}T_y^2 - 2T_xT_yT_{xy} + T_{yy}T_x^2}{\left(T_x^2 + T_y^2\right)^{3/2}} \tag{II.4.19}$$

This approach of level set runs faster, but restricts the front evolution to one direction. If the front moves past the object boundaries, it cannot move back onto them. Viewing the front as a flame expanding and burning the pixels it passes over, this is summarised as: 'once a particle is burnt, its stays burnt'.

A combination of narrow band and fast marching, called *Hermes*, is given by Paragios and Deriche in [130]. At each iteration only some pixels selected within a narrow band around the current front are updated.

Finally, another way to improve the computation time is to view the evolution of the embedding function Ψ as a minimisation problem, which can be solved efficiently numerically. In [82], Kuhne *et al.* present a semi-implicit adaptive operator splitting method to iteratively find the values of Ψ. The equation of motion is approximated as a linear equation in the form:

$$\Psi(t+1) = \frac{1}{2}\sum_{l\in\{x,y\}} \left(I - 2\,\Delta t\; A_l\left(\Psi(t)\right)\right)^{-1}\Psi(t) \tag{II.4.20}$$

where $\Psi(t)$ is a vector containing all the values $\Psi(x,y,t)$ at every pixel location, and $A_x(\Psi(t))$ and $A_y(\Psi(t))$ are square matrices containing the terms of the equation of movement sampled on the pixels. The matrices to inverse are strictly diagonally dominant tridiagonal, so the system can be solved efficiently. Alternatively, in [184], Wang *et al.* present a minimisation method using Lagrange multiplier.

Multiple objects: Schupp *et al.* use fast marching to segment multiple objects [153]. The propagating fronts have unique labels and are grown in parallel. When a front reaches a pixel, it assigns it the current iteration time and its label. If the pixel was already labeled, it stops growing locally. This prevents inter-penetrating fronts. However, this mechanism relies mainly on a correct initialisation of all level sets: in particular they are expected to be all at similar distances from objects boundaries. This makes the segmentation results less robust to initialisation.

Topology preservation: The original topology of the front can be preserved, as presented by Han *et al.* [62]. In addition to narrow band, an underlying grid

is used to sample the embedding function Ψ, and may be finer than the pixel grid. This way, the topology of the front is easier to analyse, and critical points for its topology (called non-simple points) are not allowed to change values. The other points are updated normally. The definition of simple points is based on topological numbers, describing the topology of shapes. This extra step in the processing requires further computation, and depends on the grid size used. This introduces yet another parameter to the segmentation method.

Prior knowledge: To include knowledge on shape variations within the segmentation process, Leventon *et al.* present a method based on statistical distributions of parameters describing the shape [94]. These distributions are stored as a training set, and used through to a modified equation of motion.

$$u(t+1) = u(t) + \lambda_1 F(u(t)) + \lambda_2 (u^*(t) - u(t)) \qquad \text{(II.4.21)}$$

The term $F(u(t))$ is from the standard equation of motion $u(t+1) = u(t) + F(u(t))$. The term $u^*(t)$ is the most probable final front given the current front $u(t)$ and the image: $u^*(t) = \arg\max_{u^*} P(u^*|u, f)$. This probability is decomposed with Bayes' rule and evaluated thanks to the probabilities computed during the training. In the new equation of motion, the parameters λ_i can be tuned to give more influence to the image contents or to the training data. An improved version of this method, using alignment of fronts during the training, was published by Tsai *et al.* in [173]. A similar method, using not only prior shapes but also intensity profiles, is presented by Chen *et al.* in [32]. As with other methods based on a training phase, it may be less relevant to cytometry than to other medical imaging fields, such as image guided surgery [56].

Combination of influences: In the standard implementation of active contours, image influences and contour influences are linearly combined, with tuned parameters. Conversely, with the standard level sets, the equivalent of the image influence, $\hat{k}$, and that of the contour influence, $F_G(\kappa)$, are multiplied. This removes the need for tuning before segmentation. However, at least one of the terms has to be zero for the level set to stop moving. Since the curvature is usually high, it is the image speed that stops the iterations. Whereas in the contour models, the influences may balance each other, even when none is zero. In case this feature of level sets is undesirable, linear combinations of influences can be used instead, as in the *RAGS* model presented by Xie and Mirmehdi in [192].

II.5. Other methods

In this final part, we mention other segmentation methods that have been widely used in various fields of computer vision, but are not as popular in published cytometry than the ones cited before.

II.5.1 Region growing

Region growing consists in grouping neighbouring pixels based on their similarity [48]. A region is grown from a seed pixel, and the pixels at the border of the region are gradually added if a similarity measure between them and the region is within a given range of values. The process stops when no more pixels are added. Similarity can be based on a statistical model of the object's histogram. The model may also be dynamically updated during the region-growing process.

The main strengths of region growing are its fast execution, its ease of implementation, and its flexibility. The models used are not necessarily Gaussian, as any measure of similarity can be used to compare pixels. Also, the models can be updated at runtime.

However, the resulting segmented regions usually have irregular borders and holes. Region growing is intrinsically a bottom-up process, and is not meant to include prior knowledge on global shapes. Besides, as it only segments homogenous regions, it often results in oversegmentation. Also, as it may be difficult to design a similarity criterion that excludes noise, region growing is potentially very sensitive to noise. Finally, a dynamic adaptation of the model makes the results highly dependent on the location of the seed.

A first improvement, by Sclaroff and Liu, aimed at incorporating prior shape knowledge consists in running two consecutive region growings [154]. The first time, the image is oversegmented in small homogenous regions. The second iteration actually merges them: regions are merged if their overall shape fits a deformable template, in a way similar to energy-based active contours. Inciden-

tally this second step is often used after a watershed transform. It requires a model of possible shapes adapted to the oversegmentation results: this is not practical for our application.

Another improvement concerns the robustness and automation of the region growing, as presented by Pohle and Toennies [134, 135] for organ segmentation. From a seed selected manually, a first region growing is performed, using dynamic adaptation of the similarity model. In more details, the object's intensity histogram is modeled as a Gaussian, and the mean and variance are evaluated every time the segmented region doubles in size. A tabulated correction factor is used to compensate for the under-estimated standard deviation during the growing. Once the growing is over, the final values of the mean and deviation are stored. A second run of region growing is performed, from the same seed, using these stored values as a fixed model all along the process. The segmented regions are then merged using their similarities and a shape factor. Apart from the manual seed location, which has to be near the objects' centres, this method may be automated. It is very specific to their application though. In our context, seed location cannot be manual, and single Gaussian models are not adapted to the variety of textures found in our context.

II.5.2 Neural networks

Neural networks represent a large field of research and applications in computer science, and presenting them is beyond the scope of this chapter. For detailed introductions to neural networks, we refer the reader to [121, Chapter 6], [150, Chapter 19]. Neural networks are reputed for their classification properties. However, classification often require segmentation results as an input, as for example [127], and is not the focus of our work.

A comprehensive review of the use of neural networks for image processing was recently published by Egmont-Petersen *et al.* [49]. Their section on image segmentation lists the possible networks that can be used, with many references, along with their limitations.

In [137], Poli and Valli present a segmentation method based on Hopfield networks, applied to images of brain and organs. A network is build with several two-dimensional layers of neurons, each layer corresponding to a label. Each pixel is assigned to one neuron in each layer. The energy of the network is made of two parts: a sensitivity energy, which is meant to be minimum at the boundaries, and a robustness energy, lower for large connected regions. The network is initialised by a first probabilistic segmentation based on morphological thresholding, and then evolved so as to minimise its energy. The use of energies makes this

method somehow similar to active contours. However, the robustness energy is not enough to include prior knowledge on shape, which is a general weakness of neural networks for segmentation. Also, such a network is sensitive to the actual location of objects on an image. In our context nuclei can be present literally anywhere on images.

A different use of neural networks in presented by Ossen *et al.* in [127]. Their idea is to add a classifier step after the segmentation, and use the results of the classification as new parameters for a further segmentation. They use back-propagation feed-forward neural network as a classifier, and texture properties of the segmented objects to compute a posteriori probabilities. Useful as it is, this step is not linked to segmentation, but to object recognition, beyond the scope of our work.

Finally, Shareef *et al.* use oscillatory networks for segmentation of brain images [158]. It is meant to group pixels based on their similarities. This method is also specific to the imaging protocols used, namely MRI and CT, and is not adapted to fluorescent microscopy.

II.5.3 Region competition

We present region competition, by Zhu and Yuille [203, 204], for completeness. It is based on principles underlying active contours, region growing and probabilistic segmentation. It requires prior models of the object intensity distributions. A region of the image is called *homogenous* if its intensity values correspond to one predefined model. As it is unlikely that a region fits a model perfectly, the homogeneity of a region is measured as its probability of corresponding to a given model.

Region competition is an iterative segmentation based on energy minimisation. A region, characterised by a specific parametric model (e.g. of its histogram) is grown from a seed. Pixels are added to a nearby region based on its similarity with the region's model, using a probabilistic framework. Since the models' parameters and the region's contents are co-dependent, but unknown to start with, they are evaluated iteratively, with a greedy method. After the first region-growing, the models' parameters are re-evaluated. These new parameters are then fixed, and the objects' boundaries are modified using two forces. A smoothing force, which is high where the boundary has a high curvature, will straighten the boundary, while a statistics force, which is weak when the region has a high homogeneity, will compress the region. If the regions do not cover the whole image, a new seed is selected inside uncovered parts, and a new run of the greedy region growing method is performed. Once all the image is segmented, the next step of

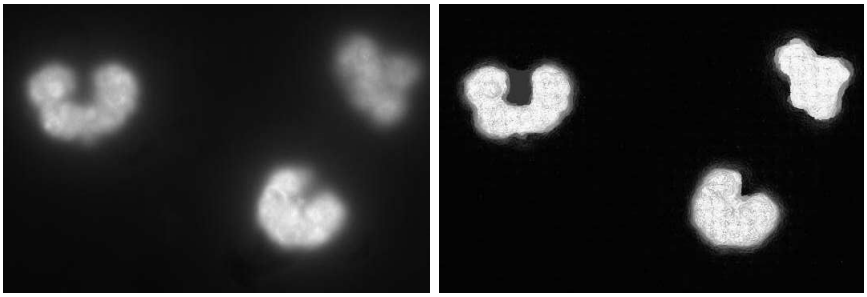

Figure II.5.1: *Image segmented with dynamic graph-cut. Left: original image. Right: results of the dynamic graph-cut. The pixel brightness is proportional to their likelihood of belonging to a nucleus. Although the boundaries are generally correct, the results inside the nuclei are noisy.*

the algorithm merges neighbouring regions if that reduces the overall energy over the image. If no regions were merged, the segmentation is over; otherwise, after merging, a new run of the greedy method is performed.

This method is reported to be robust to the original selection of seeds [203, 204]. A feature of the region merging process can automatically rule out irrelevant regions – *i.e.* regions that are either not part of an object or which did not pick the correct model.

By combining active contours and region growing, this method also keeps their drawbacks. In particular, it requires the tuning of many parameters for different steps of the segmentation. It also requires that each region has a distinct parametric model, which also needs to be learnt from the image. This is not adapted for our application, where all nuclei in a given image tend to have very similar histograms.

II.5.4 Graph cut

Graph cut refers to a wide family of algorithms, meant to separate weighted graphs in subparts [42]. For image segmentation, they are usually performed on Markov Random Fields [13, 17]. As these two topics are beyond the scope of our review, we only summarise them. Markov Random Fields assign labels to pixels and underlying connections between pixels. In a probabilistic framework, the label assigned to each pixel depends on its intensity, and also on the labels of the connected pixels. By assigning a penalty or a cost to each pixel and each pairs of pixels, a weighted graph is built on the whole image. The subgraphs that can be isolated by separating pairs at a minimal cost, in other words by performing a min-cut on the graph, can be interpreted as different segmented regions. Unlike active contours, this method achieves a global minimisation of the functions used to define the penalties. However, the definition of the penalties

is mainly restricted to absolute pixel intensities and connected pixel values [79]. Also, in a way similar to level sets, it is difficult to encode shape or topology constraints on the segmented regions.

Recent improvements of graph-cuts include the addition of shape priors in the graph weights [84]. As explained above, prior knowledge on shape is difficult to obtain reliably in our context. Another extension of graph-cut consists in assigning a confidence value instead of a label to pixels [77]. An example of this method is shown in Figure II.5.1. This method, however, cannot be used as a standalone for our needs, but only as a pre-processing. The image still needs to be post-processed to isolate the distinct nuclei, and touching nuclei can be difficult to separate. This method is more adapted to images showing a single object with a regular texture.

Summary

In this part, we reviewed several segmentation methods, including low-level vision, watershed, active contours, level sets, reflecting the methods commonly used in cytometry. We presented their original definitions, strengths and weaknesses, and published improvements. We showed how the requirements for our application, explained in Chapter I, restrict the use of existing methods, in particular:

- The full automation required forbids manual intervention during the segmentation, in particular for the initialisation.
- The unknown number, location and closeness of nuclei requires robust seed-finding.
- The variation of shapes (in particular concavities), sizes and textures of nuclei makes learning-based methods very sensitive to the training set, thus loosing robustness.
- The variations in imaging conditions and nuclei appearance require image-based parameter values for robustness, which makes manual tuning unpractical.

For these reasons, the simultaneous requirements of robustness and automation for our application call for novel methods of segmentation. In the next chapter we present the methods we developed to segment nuclei and probes. In particular we detail the algorithms we use, and present quantitative comparison with existing methods.

Chapter III

Evaluating the Telomere Intensity in Leucocyte Nuclei from Different Individuals

In this chapter we present our novel segmentation methods. We start with the segmentation of nuclei, detailing our novel model for the image and our adaptation of the Expectation-Maximisation (EM) algorithm to adjust our model's parameters to an image. We then present our segmentation method for telomeric probes, based on a new dome-detection algorithm. We compare both our methods with existing methods, and discuss the strengths of our approaches. Finally, we present the results we obtained with our methods on the data set used for the pilot study.

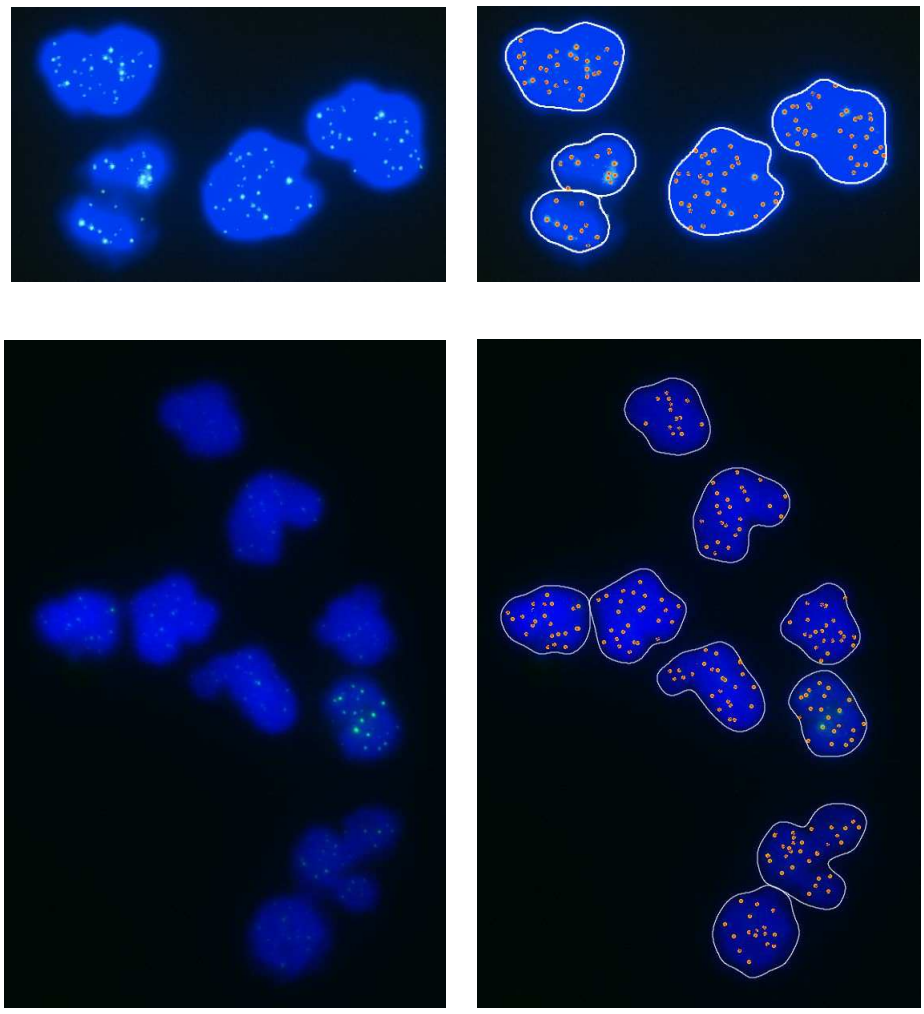

Figure III.0.2: *Left column: Images showing leucocyte nuclei (in blue), containing probes attached to the telomeres (in green). Right column: nuclei and probes segmented with our methods.*

III.1. Segmentation of nuclei

To segment the nuclei under the requirements of robustness and significant variations in the image properties described in Chapter I, we developed a new method of segmentation. It is a three-step method, outlined below. Its details are provided in this section, and a summarising illustration is shown as Figure III.1.5 page 72.

Step 1: Find the image regions containing nuclei. The method starts by modeling the image's histogram with a novel model accounting for each part of the image accurately. This model is fitted to the histogram automatically, with an Expectation-Maximisation algorithm that we adapted for histogram matching. Once fitted, the model is used to find a global threshold value removing most of the background. Each of the segmented regions contains nuclei and still some background.

Step 2: Delineate the nuclei. Each region segmented in step 1 is processed separately with the same method. The histogram model is fitted to the region's histogram with the adapted EM algorithm, and is used to define a local threshold. The thresholded components do not contain background any more, but may contain touching nuclei. They will be used as masks for the final operation.

Step 3: Separate the touching nuclei. To detect and separate touching nuclei, the model fitted to the region's histogram is used to define a higher threshold. Each isolated component corresponds to the inside of a single nucleus, and is marked as a seed. A fast region growing based on distance transform within the masks found previously is performed on the seeds to obtain the final segmentation of nuclei.

Before explaining our segmentation method, we detail first its core features, namely our histogram model and our adapted EM algorithm. We then explain

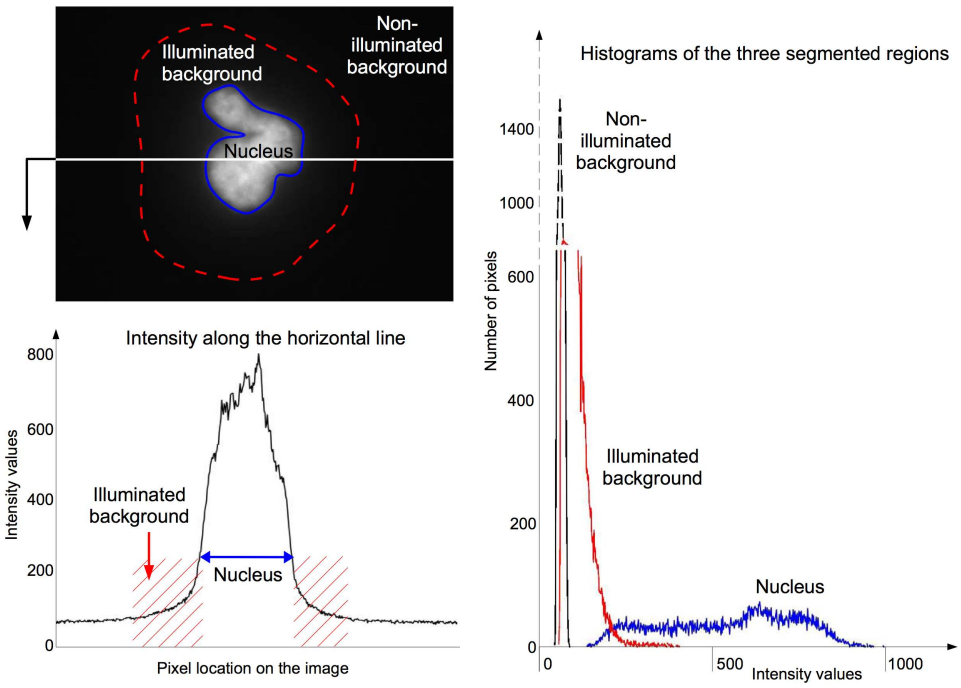

Figure III.1.1: *Background illumination. Top left: image with segmented nucleus, illuminated and non-illuminated background. Bottom left: intensity values along the horizontal line across the image. Right: Histograms of the three segmented regions (The vertical scale is bilinear, as reflected by the values on the side).*

our complete segmentation method, in particular how we use our model to derive the threshold values needed in each of the steps described above. Finally we present and discuss the results obtained with our method, compared with other methods we implemented.

III.1.1 Model of the histogram of an image

As explained in Chapter I, the nuclei have been treated with fluorescent marker DAPI, and when illuminated with light at their exciting wavelength, they diffuse light all around them. The light emitted from the nuclei upwards, towards the microscope lenses, is not the only light collected on the CCD camera though. Part of the light emitted sideways is deflected by the surrounding materials, and part of that deflected light will be collected by lenses and the camera. The resulting image shows a dim enlightenment of the background regions surrounding nuclei. This effect is hardly noticeable by eye, but alters significantly the background intensity values, increasing them up to three-fold. Taking this effect into account is critical to the correct segmentation of the nuclei, but has not yet been addressed directly, to the best of our knowledge. We introduce the term *illuminated background* to

denote the affected background regions surrounding the nuclei, as opposed to the *non-illuminated background*. Figure III.1.1 page 62 shows the three regions of a typical image, a profile of intensities across them, and their histograms. The profile and the histograms show the raise of intensity values in the illuminated background, marked in red.

The extent of the non-illuminated background depends on several unknown or inaccessible parameters, such as the shapes, sizes, concentrations of the nuclei, the quantity of markers they contain, the intensities of light they received or the exposure time. Therefore it cannot be determined directly from an image before segmentation. However, the histograms of the nuclei, the non-illuminated and illuminated backgrounds can be extracted from the histogram of the whole image, in a way described in Section III.1.2. Once extracted, these histograms can be used to segment the nuclei, as explained in Section III.1.3.

As illustrated in Figure III.1.1, an image's histogram consists of three slightly overlapping parts: a sharp peak in the lowest values, a sharply decreasing curve in the medium values, and a plateau with any number of domes and valleys in the highest values. They correspond respectively to the non-illuminated background (NIB), illuminated background (IB), and nuclei (N). In this section, we present the parametric functions we use to model each part, with particular emphasis on our new model for the illuminated background. Let $h(I)$ be an image histogram, consisting of parts NIB, IB and N, which we aim to model with $h_{model}(I)$.

Non-Illuminated Background. To model the NIB, we assume that it contains A_b pixels, has a mean value I_b, and is affected by Gaussian noise of standard deviation σ_b. Using a Gaussian model is supported by observations of images containing no nuclei. The NIB is modeled with:

$$NIB(I) = \frac{A_b}{\sqrt{2\pi}\sigma_b} \exp\left(-\frac{(I - I_b)^2}{2\sigma_b^2}\right) . \tag{III.1.1}$$

Nuclei. The part of the histogram corresponding to the highest intensities, N, reflects the textures of the nuclei, which show high variability within and across images. In particular, variations affect the range of intensity values, the shape of the histogram and its number of peaks, as illustrated in Chapter I. Also, saturation can occur at high intensities, depending on the procedure and hardware used for imaging. To overcome these problems, we model the histogram of the nuclei with a sum of Gaussians: this is both robust and flexible enough for our needs. Since we do not know in advance how many nuclei are on an image, nor how many Gaussians are needed for each texture, we introduce a new parameter, n, the number of Gaussians modeling the nuclei's histogram. Each of

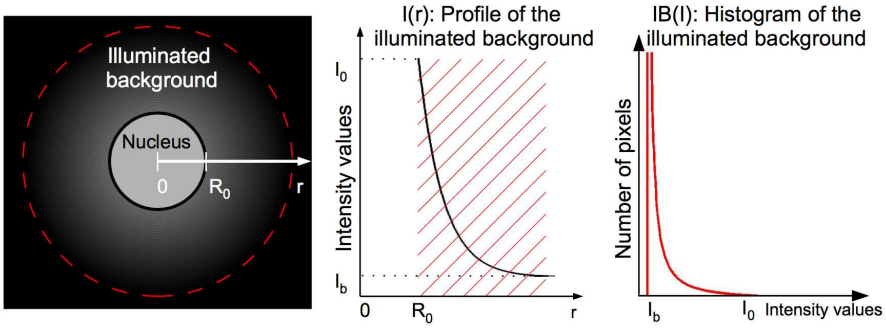

Figure III.1.2: *Illustration of our model. Left: model of a circular nucleus. Center: model of the intensity values in the illuminated background, $I(r)$, defined in Equation (III.1.3). Right: model of the histogram of the illuminated background, $IB(I)$, defined in Equation (III.1.12).*

these Gaussians i will model A_i pixels, with mean I_i and deviation σ_i:

$$N_i(I) = \frac{A_i}{\sqrt{2\pi}\sigma_i} \exp\left(-\frac{(I-I_i)^2}{2\sigma_i^2}\right) \ , \ 1 \leq i \leq n \ . \tag{III.1.2}$$

Illuminated Background. Our model of the illuminated background's histogram is based on a model of the physics that generates it. We model the light diffused outside a nucleus as a function of the distance to that nucleus, and integrate it all around the nucleus. We then use this model to measure the background area having a given intensity. Finally we apply it to integer intensities to obtain a model of the histogram of the illuminated background. Given that our model will only be used for intensity values I above the mean background value I_b with $I - I_b \gg 1$, we develop expressions to the first order in $\frac{1}{I-I_b}$ when appropriate.

We consider a circular nucleus, as illustrated in the left of Figure III.1.2, but will then make our model independent from the nucleus' shape. Let I_0 be the intensity at the border of the nucleus, at distance R_0 from its center, and I_b be the average intensity of non-illuminated background. We model the intensity in the illuminated background, along a line normal to the nucleus, with a decreasing exponential (see middle of Figure III.1.2):

$$I(r) = I_b + (I_0 - I_b) \cdot \exp\left(-\frac{r-R_0}{\rho}\right), \text{ for } r \geq R_0 \ . \tag{III.1.3}$$

The parameter ρ controls the slope of the intensity's decay: it corresponds to the distance outside the nucleus at which the intensity has decreased by $\frac{1}{e} \approx 37\%$. Our model, however, cannot be fitted directly to an image for segmentation purposes as it requires a prior segmentation of the nuclei. Nevertheless, it can be used to derive a model of the histogram of the illuminated background. This

latter model will be easier to adjust to the image histogram, as detailed in the next section. We now explain how to derive that model.

The expression of $I(r)$ in Equation (III.1.3) can be inverted to define $r(I)$:

$$r(I) = R_0 - \rho \cdot \ln \frac{I - I_b}{I_0 - I_b} \tag{III.1.4}$$

Using Equation (III.1.4), the number of points $dn(r) = 2\pi\, r\, dr$ at distance r from the nucleus can be expressed as a function of the intensity:

$$dn(I) = 2\pi \left(R_0 - \rho \cdot \ln \frac{I - I_b}{I_0 - I_b} \right) \cdot \rho \cdot \frac{-dI}{I - I_b} \tag{III.1.5}$$

Introducing the new parameters $\alpha = \frac{\rho}{R_0}$ and $A = \pi R_0^2$, $dn(I)$ can be written as:

$$dn(I) = 2\, A\, \alpha \left(1 - \alpha \ln \frac{I - I_b}{I_0 - I_b} \right) \frac{-dI}{I - I_b}\ . \tag{III.1.6}$$

The expression of $dn(I)$ is now independent of the actual shape of the nucleus. It only depends on its area A and the dimensionless parameter α, which controls the extent of the illumination relative to the size of the nucleus. By integrating $dn(I)$ between I and $I+1$, we obtain by definition the histogram of the illuminated background. Since $dn(I)$ is a decreasing function of I, its has to be integrated from $I+1$ to I:

$$IB(I) = \int_{I+1}^{I} dn(I') = 2\, A\, \alpha \left(\underbrace{\int_{I}^{I+1} \frac{dI'}{I' - I_b}}_{a} - \alpha \underbrace{\int_{I}^{I+1} \ln \left(\frac{I' - I_b}{I_0 - I_b} \right) \frac{dI'}{I' - I_b}}_{b} \right) \tag{III.1.7}$$

The two terms a and b of Equation (III.1.7) can be integrated separately and developed in the first order with respect to $\frac{1}{I - I_0}$. The first term is:

$$a = \left[\ln(I' - I_0) \right]_I^{I+1} = \ln \left(1 + \frac{1}{I - I_0} \right) = \frac{1}{I - I_0} + o\left(\frac{1}{I - I_0} \right) \tag{III.1.8}$$

The second term can be integrated with the change of variables $X = \frac{I' - I_b}{I_0 - I_b}$:

$$b = \int_{\frac{I - I_b}{I_0 - I_b}}^{\frac{I+1-I_b}{I_0-I_b}} \frac{\ln X}{X} dX = \left[\frac{1}{2} \ln^2 X \right]_{\frac{I-I_b}{I_0-I_b}}^{\frac{I+1-I_b}{I_0-I_b}} \tag{III.1.9}$$

Using the identity $\ln^2 x - \ln^2 y = \ln(x\, y) \cdot \ln \frac{x}{y}$, b can be factorised and developed with respect to $\frac{1}{I - I_b}$:

$$\begin{aligned} b &= \ln \left(1 + \frac{1}{I - I_b} \right) \cdot \left(\ln \left(\frac{I - I_b}{I_0 - I_b} \right) + \frac{1}{2} \ln \left(1 + \frac{1}{I - I_b} \right) \right) \\ &= \left(\frac{1}{I - I_b} + o\left(\frac{1}{I - I_b} \right) \right) \cdot \left(\ln \left(\frac{I - I_b}{I_0 - I_b} \right) + o(1) \right) \\ b &= \frac{1}{I - I_b} \cdot \ln \left(\frac{I - I_b}{I_0 - I_b} \right) + o\left(\frac{1}{I - I_b} \right) \end{aligned} \tag{III.1.10}$$

Using Equations (III.1.8) and (III.1.10) in Equation (III.1.7), we get:

$$\begin{aligned} IB(I) &= \frac{2\ A\ \alpha}{I - I_b}\left(1 + \alpha\ \ln\left(\frac{I_0 - I_b}{I - I_b}\right)\right) + o\left(\frac{1}{I - I_b}\right) \\ IB(I) &= \frac{2\ A\ \alpha^2}{I - I_b}\ln\left(\frac{I_0 - I_b}{I - I_b}\right) + O\left(\frac{1}{I - I_b}\right) \end{aligned} \tag{III.1.11}$$

Keeping only the first-order term in Equation III.1.11 leads to the definition of our model of the illuminated background's histogram:

$$IB(I) = \frac{2\ A\ \alpha^2}{I - I_b}\ln\left(\frac{I_0 - I_b}{I - I_b}\right)\ . \tag{III.1.12}$$

This function is illustrated in the right-hand side of Figure III.1.2. The two parameters A and α correspond respectively to the area of the nucleus creating the illumination, and to the spatial decay of the illumination. The two parameters I_b and I_0 corresponds respectively to the mean intensity of the non-illuminated background and to the intensity at the border of the nucleus causing the illumination.

To link this model with that of the nuclei, we assume that each Gaussian modeling the nuclei creates part of the illumination. Let $IB_i(I)$ describe the background illuminated by $N_i(I)$. Three of its four parameters are constrained by the rest of the model: the area causing the illumination $A = A_i$, the mean intensity I_b of the non-illuminated background, and the intensity at the border of the nucleus. We set the value of this latter parameter to $I_0 = I_i - 2\sigma_i$: it corresponds to the darker 5% of the nucleus' pixels, which we consider to be on the boundary. This way, the functions modeling the illuminated background are:

$$IB_i(I) = \frac{2\ A_i\ \alpha_i^2}{I - I_b}\ln\left(\frac{I_i - 2\sigma_i - I_b}{I - I_b}\right)\ . \tag{III.1.13}$$

Let Φ_n be the set of all the functions used, which are defined in Equations (III.1.1), (III.1.2) and (III.1.13). The model of the histogram is:

$$h_{model}(I) = \sum_{g \in \Phi_n} g(I)\ \text{, where } \Phi_n = \{NIB\} \cup \bigcup_{1 \leq i \leq n} \{IB_i, N_i\}\ . \tag{III.1.14}$$

It depends on the $4(n+1)$ parameters $n, A_b, I_b, \sigma_b, \{A_i, I_i, \sigma_i, \alpha_i\}_{1 \leq i \leq n}$. They are adjusted to an image histogram using our adapted Expectation-Maximisation algorithm, as detailed in the next section.

III.1.2 Expectation-Maximisation algorithm for histogram modeling

The term *Expectation-Maximisation* (EM) refers to a class of algorithms that iteratively fit a parametric model to incomplete data [172]. The missing data may be

either missing points in a series (e.g. missing pixels in an image, or missing frames in a video), or missing dimensions: a typical example is the missing labeling of pixels in a non-segmented image. Given the parameters of the model of the complete data, the missing points or dimensions may be inferred from the available data. Reciprocally, supposing the available data was complete, the parameters of the model could be computed properly. The problem of fitting a parametric model to incomplete data is that neither the parameters nor the complete data are available in the first place.

The idea underlying an EM algorithm is that the parameters can be estimated given an estimation of the complete data, resulting in a new model. Then, the missing data can be re-estimated based on the latest model. Iterating these steps may result in a convergence of the model to the existing data, and at the same time in a stable estimation of the missing data. Oscillations or divergence may occur, in which case the EM algorithm should be initialised differently.

Formally, let f be the available data, g the missing data, and $D = (f, g)$ the complete data. Let $\Phi(\{p_i\})$ be a parametric model of D, depending on the set of parameters $\{p_i\}$. The two versions of EM algorithms fitting Φ to D are presented in Algorithm 1.

Algorithm 1 General Expectation-Maximisation algorithm: Two versions

Version 1: Estimating the parameters first

1: *Initial E-step*: estimate $\{p_i\}$ given f
2: **repeat**
3: *M-step*: estimate g given f and $\Phi(\{p_i\})$
4: *E-step*: estimate $\{p_i\}$ given $D = (f, g)$
5: **until** convergence

Version 2: Estimating the missing data first

1: *Initial M-step*: estimate g given f
2: **repeat**
3: *E-step*: estimate $\{p_i\}$ given $D = (f, g)$
4: *M-step*: estimate g given f and $\Phi(\{p_i\})$
5: **until** convergence

The criterion for *convergence* depends on the model used and the results expected. For example, the iterations can be stopped as soon as the error between Φ and D (defined accordingly) stops decreasing, or reaches a given threshold value. Alternatively the iterations may be performed a fixed number of times, and the final model Φ is one that had a minimal error.

The terms *Expectation* and *Maximisation* refer to the versions of such algorithms that use the statistical Expectation to estimate the parameters of the

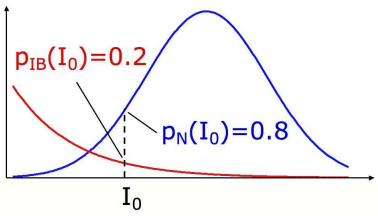

Figure III.1.3: *Illustration of the proportions. At intensity I_0, the function IB accounts for 20% of the modeled value of the histogram, and the function N for 80%.*

model in the E-step, and that estimate the missing data in the M-step by maximising the likelihood that the current model fits the complete data. Such algorithms are commonly used in Computer Vision to fit a mixture of Gaussian models to data with missing labels. In a probabilistic framework, such algorithms also include constraints on the model to ensure that the probabilities of a model or at a point add up to 1. Such constraints, however, come from the use of probabilities, not the use of an EM algorithm.

To explain how we fit the models defined in the previous section to an image histogram with an EM algorithm, we first introduce the notion of *proportions*. Let $h(I)$ be an image histogram, consisting of parts NIB, IB and N, which we aim to model with $h_{model}(I)$. Each intensity I in the histogram contains a proportion of pixels modeled by each function of our model (see Figure III.1.3). We define this proportion as:

$$p_f(I) = \frac{f(I)}{\sum_{g \in \Phi_n} g(I)} \ , \forall f \in \Phi_n \ . \tag{III.1.15}$$

Knowing these proportions is enough to define the successive thresholds needed for our nucleic segmentation, as detailed at the end of this section, and is therefore our goal. Should the model's parameters be known, the proportions can be computed using Equations (III.1.1), (III.1.2), (III.1.13) and (III.1.15). Reciprocally, given all the proportions $p_f(I)$, $\forall I$, $\forall f \in \Phi_n$, the model's parameters can be computed as described below. However, neither the parameters nor the proportions are available in the first place. As explained above, this type of problem can be solved by Expectation-Maximisation [172].

The algorithm we use, presented as Algorithm 2, is adapted to histograms: the steps are the same as in Algorithm 1 Version 1, only the equations used are specific. As explained in the previous section, the number of Gaussian n needed to model the nuclei's textures is unknown. To find the model which best fits an image's histogram, we iterate the EM algorithm with increasing values of n, and keep the model with the lowest error.

Algorithm 2 Expectation-Maximisation algorithm for histogram modeling

for $n = 1$ to 5 **do**
  Initial E-step: set the initial proportions as listed in Table III.1.1.
  for 100 times **do**
    M-step: compute the parameters with Equations (III.1.16) and (III.1.22).
    E-step: update the proportions with Equations (III.1.1), (III.1.2), (III.1.13), (III.1.15).
    Evaluation: measure the error between the model and the histogram with Equation (III.1.23). Store the model if the error is the lowest.
  end for
end for
return the model with the lowest error.

Table III.1.1: *Initial values of the proportions used for the EM algorithm.*

Intensity	$0 \dots \frac{1}{n+2} I_{max}$	$\frac{1}{n+2} I_{max} \dots \frac{2}{n+2} I_{max}$	$\frac{j+1}{n+2} I_{max} \dots \frac{j+2}{n+2} I_{max}, 1 \leq j \leq n$
$p_{NIB}(I)$	0.9	0.1	0
$p_{IB_i}(I)$	$0.1/n$	$0.9/n$	$0.1/n$
$p_{N_i}(I)$	0	0	0.9 if $i = j$, 0 else

Initial E-step: Given a value of n, the initialisation step is performed as follows. Intuitively, most of the dark pixels are modeled by NIB, most of the bright pixels by either one of the N_i, and most of the remaining pixels by the IB_i (see Figure III.1.1). The range $[0, I_{max}]$ of the histogram is divided in $n+2$ segments, and each proportion is initialised by a fixed value on each segment. The actual values we use are listed in Table III.1.1.

M-step: We now detail how to compute the parameters of our model given the histogram $h(I)$ and all the proportions $p_f(I)$. Regarding the Gaussian functions NIB and N_i, the total, mean and deviation of a weighted histogram are evaluated as [161]:

$$A_i = \sum_I p_{N_i}(I)\, h(I) \; ; \; I_i = \sum_I p_{N_i}(I)\, h(I)\, I \; ; \; \sigma_i^2 = \sum_I p_{N_i}(I)\, h(I)\, (I - I_i)^2 \tag{III.1.16}$$

For the remaining functions IB_i, the only parameter to compute is α_i. Using the notation of Equation III.1.6, the sum of histogram values of the illuminated background between any two values I_1 and I_2 is:

$$\sum_{I=I_1}^{I_2} IB(I) = \int_{I_1}^{I_2+1} dn(I) \tag{III.1.17}$$

However, $dn(I)$ is only defined and positive between I_b and I_0, and is not summable near I_b. Let $I_\varepsilon = I_b + \varepsilon\,(I_0 - I_b)$, where $\varepsilon \in (0,1)$:

$$\sum_{I=I_\varepsilon}^{I_0-1} IB(I) = \int_{I_\varepsilon}^{I_0} dn(I) \tag{III.1.18}$$

Developing to first order terms, we get:

$$\sum_{I=I_\varepsilon}^{I_0-1} IB(I) = -2\,A\,\alpha^2 \int_{I_\varepsilon}^{I_0} \ln\left(\frac{I - I_b}{I_0 - I_b}\right) \frac{dI}{I_0 - I_b} \tag{III.1.19}$$

Since $IB(I_0) = 0$, the sum can be extended to I_0, while the integral can be computed with a change of variable:

$$\sum_{I=I_\varepsilon}^{I_0} IB(I) = A\,\alpha^2 \ln^2 \varepsilon \tag{III.1.20}$$

This gives the expression of α as a function of the model values:

$$\alpha = \frac{1}{|\ln \varepsilon|} \sqrt{\frac{1}{A} \sum_{I_\varepsilon}^{I_0} IB(I)} \tag{III.1.21}$$

To evaluate α_i from a labeled histogram, we replace $IB(I)$ in Equation (III.1.21) with its evaluation $p_{IB_i}\, h(I)$:

$$\alpha_i = \frac{1}{|\ln \epsilon|} \sqrt{\frac{1}{A_i} \sum_{I=I_\epsilon}^{I_i - 2\sigma_i} p_{IB_i}\, h(I)} \tag{III.1.22}$$

where $I_\varepsilon = I_b + \varepsilon\,(I_i - 2\sigma_i - I_b)$. In our application we use $\varepsilon = 0.1$.

E-step: Given a parametric model $\Phi_n = \{NIB\} \cup \bigcup_{1 \le i \le n} \{IB_i, N_i\}$, the proportions can be computed directly from their definitions in Equation (III.1.15).

Evaluation: The error we use to evaluate a given set of parameters has to reflect how each part of the model fits the histogram, as equally as possible. The main issue is that the histogram values corresponding to the N_i components are about 20 times lower than that of the NIB. However, it is important that both parts are correctly modeled at the same time. To overcome this issue, we use the error measure of the χ^2 test:

$$error = \sum_I \left(1 - \frac{h_{model}(I)}{h(I)}\right)^2 \tag{III.1.23}$$

Using Algorithm 2, the parameters of our model for the image histogram can be adjusted automatically. In the next section we explain how to use a fitted model to segment the nuclei, by defining global and local thresholds.

III.1.3 Complete segmentation of the nuclei

The complete segmentation of the nuclei is performed in three steps, as illustrated on Figure (III.1.5). First, we use the algorithm above to adjust our parametric model to the image histogram. Once the model is fitted to the histogram, let:

$$\theta_{global} = \max \{I \ : \ \forall i \, , \, \min(p_{NIB}(I), p_{IB_i}(I)) \geq p_{N_i}(I)\} \ . \tag{III.1.24}$$

Below this value, all intensities contain more points from NIB or IB_i than from the corresponding N_i – and it is the highest such value. This is the global threshold we use to discard the non-illuminated and part of the illuminated background. Then, in each of the segmented regions, we apply the same algorithm to find a model of the histogram (without the NIB function this time). In a similar way, we find the highest intensity containing more points from all IB_i than from all N_i, and use it as a local threshold θ_{local}:

$$\theta_{local} = \max \left\{ I \ : \ \sum_{i=1}^{n} p_{IB_i}(I) \geq \sum_{i=1}^{n} p_{N_i}(I) \right\} \ . \tag{III.1.25}$$

The definition of the global threshold is more strict than that of the local threshold, for the following reason. In the global histogram it is more difficult to draw a limit between dark nuclei and bright illuminated background. Since the image intensity tend to vary across an image, brighter parts of the image containing brighter nuclei will also have brighter illuminated background. Using the sum of the IB and N functions in the global model would penalise darker nuclei in darker parts of the image.

The newly segmented components do not contain background any more; however, they might contain more than one nucleus. This is often resolved by studying the concavities of the nuclei's outlines [85], but cannot be applied to uncultured nuclei. We consider the texture instead, which is already modeled by the N_i, and assume that there is more than one distinguishable nucleus if there is a dark path in the region separating two bright components. The threshold we use for this test, called inner threshold θ_{inner}, is the lowest of the I_i. The connected components above θ_{inner} are considered as seeds: each one marks a unique nucleus. We then extend the seeds into the regions above θ_{local} using a fast distance transform [51], reproduced in Appendix A page 128, to obtain the separated nuclei. Figure (III.1.5) shows the three steps of the segmentation, with the models adjusted to the histograms. Examples of segmented images are shown in Figure III.0.2 page 60.

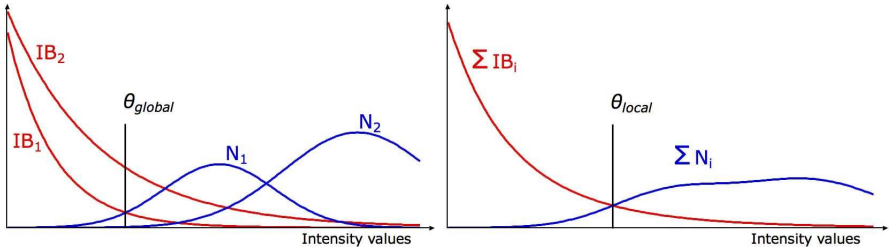

Figure III.1.4: *Global and local thresholds obtained from a fitted model.*

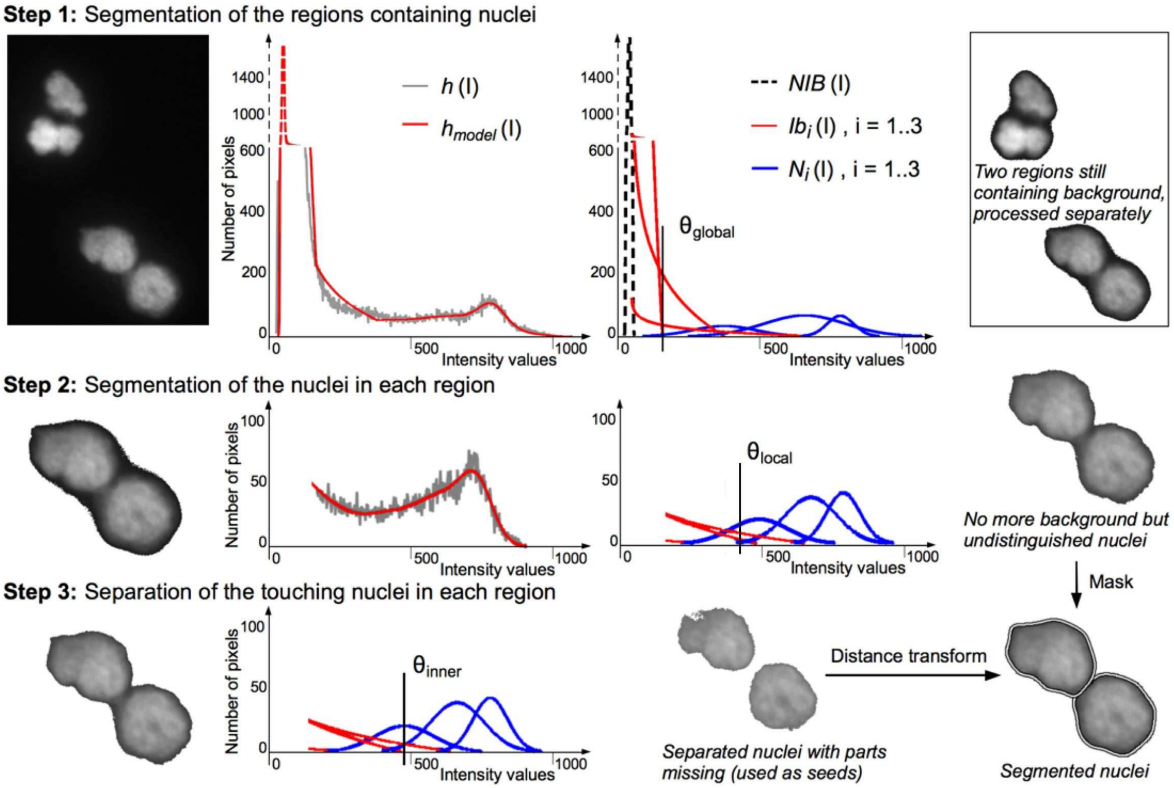

Figure III.1.5: *The stages of nucleic segmentation. Top row, left to right: original image; its histogram with our adjusted model superimposed; the components of our model, used to find a global threshold removing most of the background; the segmented image, with two segmented regions containing nuclei but also some background. Middle row: one of these regions; its histogram and our adjusted model; the components of our model, used to find a local threshold, removing the remaining background; the segmented region, with no more background, but where the two nuclei are still undistinguished: it will be used as a mask for the final step of the segmentation. Bottom row: the segmented region; the components of our model, used to find an inner threshold, removing the darkest parts of the nuclei; the segmented nuclei, isolated but with parts missing: they are used as seeds, and grown with a fast distance transform within the mask defined above; the resulting segmentation of the region, with two separated nuclei and no background.*

III.1.4 Results and discussion

We present the quantitative results obtained using our two methods of segmentation. Our data set contains 2,166 images, showing overall about 14,000 nuclei and 315,000 probes. For comparison, we also implemented a watershed-based method for nucleic segmentation, detailed in [104].

Nucleic Segmentation. We implemented our method as described above, on an iMac with a 1.8GHz PowerPC G5 with 1Gb of RAM. The EM algorithm is used with up to 5 histogram components, fitted during 100 iterations, with initial values as listed in Table III.1.1. These parameter values were selected empirically to give a reasonable combination of speed and accuracy. For comparison, we also implemented a typical watershed-based method used in cytometry, and described in [104]. Briefly, the main steps of this segmentation are as follows. First, the image is thresholded globally with a value found by the isodata algorithm; a distance transform is applied on the resulting image, followed by an h-dome extraction; the zones extracted are used as starting-point for the watershed algorithm, which is applied to the gradient transform of the original image. We implemented this method under the same conditions as ours, and tested it on a sample of 800 images, containing over 2,000 nuclei. Only part of the images was used for the watershed for practical time reasons. They were chosen to represent the variety of imaging conditions, in the following way. Images are organised in 11 directories, each one corresponding to specific imaging conditions. The first images of each directory were selected, until 800 images were chosen. The results of these two segmentation methods are listed in Table (III.1.2), and discussed below.

Table III.1.2: *Results of the nuclei segmentation.*

Segmentation	Watershed	Ours
Number of images	800	2,116
Number of nuclei	2,779	13,917
Correctly Segmented	2,232 = 80.3 %	13,823 = 99.32 %
Over-segmented	211 = 7.6 %	31 = 0.22 %
Under-segmented	212 = 7.6 %	50 = 0.36 %
Ignored	60 = 2.2 %	8 = 0.06 %
Non existing	64 = 2.3 %	5 = 0.04 %

First, in terms of runtime, our method segments one nucleus in about 1 second (with no particular programming optimisation), which is about 3 times faster than the watershed-based one, and 5 times faster than manual segmentation. Our

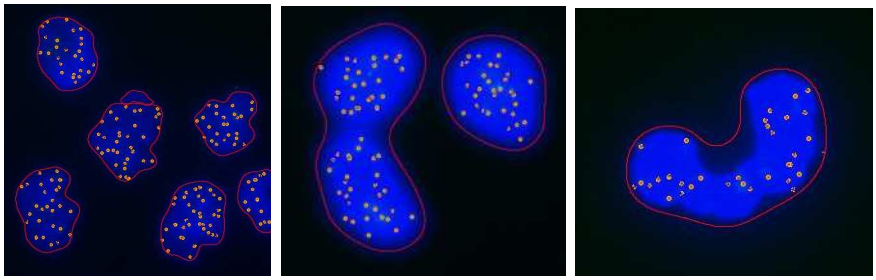

Figure III.1.6: *Examples of incorrect segmentations. Left: over-segmentation due to an inner threshold too high. Middle: under-segmentation due to an inner threshold too low. Right: under-segmentation due to an outer threshold too low.*

method has linear complexity, and has no particular memory requirements (other than for a histogram and for the segmentation results): once the histogram is computed, our EM algorithm runs in constant time, then the thresholding steps require one image scan. Conversely, the watershed-based method stores extra intermediate images, and the h-dome extraction requires an undetermined number of image scans.

The quantitative results are significantly better with our method, which is due to its two main features. First, it finds the nucleic borders using a succession of threshold values that are adapted for each part of the image containing nuclei, while the other method uses a single global threshold: as a result, many more nuclei are ignored, when darker that the global threshold, and many non-existing nuclei are segmented, which are in fact bright background regions. Secondly, our method uses a texture model to separate touching nuclei, and gets very low over-segmentation (when a nucleus is segmented in more than one part) and under-segmentation (when more than one nucleus are segmented as one part). Conversely, the watershed-based method replaces the texture with distance-transform to find seeds, which amounts to using only the outer shape of the nuclei to separate them: this approach is bound to fail with uncultured nuclei, having concavities, as illustrated by the higher over- and under-segmentation rates. Similar results are reported in [143], for this watershed-based method and a contour-based method: both methods reach around 80% accuracy, and 15% of over- and under-segmentation together. Using successive watershed-based and contour-based methods, [12] claims a 99.4% segmentation accuracy, but only after rejecting the non-isolated, non-elliptic nuclei – about 30% of their data, more than 50% of ours.

Our results can still be improved by basic post-processing. Ignored objects cannot be recovered, but are very rare in the first place, while non-existing nuclei are hardly an issue. Oversegmentation happens when θ_{inner} is too high, and can be detected by the small size of the parts oversegmented. Under-segmentation is due to either θ_{global} or θ_{local} being too low, and often results in bigger than average

objects, which could be detected as such and processed with higher thresholds. Examples of under and over-segmentation are shown in Figure III.1.6.

III.2. Segmentation of telomeric probes

Once the nuclei are segmented, their telomere content is evaluated: this is performed by segmenting the fluorescent probes in the green channel. The probes appear as small spots of about twenty pixels in area. Background illumination is observed around the probes as well; however we cannot apply the same segmentation method as for the nuclei. This is for practical reasons: for a typical image, the nuclei represent 8% of the pixels in the image, and the illuminated background about 50%, but the probes only represent 0.3%, and the background around them, 2%. Adjusting our model based on so few pixels would not be reliable enough.

As explained in Chapter I, the FITC images can be affected by foreground noise: unattached and unwashed clustered probes can appear on some images, sometimes overlapping a nuclei in the DAPI channel. This is illustrated in Figure III.2.1. Although it is not frequent, in about one in thirty images, segmenting it as valid attached probes would affect the reliability of our system, which is meant in the long run to identify rare fetal cells based on their probe contents.

Existing methods of probe segmentation fall in two categories. Some methods are meant to count the number of probes, usually to detect aneuploidies [92, 113, 123, 167]. These methods are not applicable for our task, where the total segmented intensity is more relevant than the exact number of probes. The other category is concerned with a quantitative evaluation of fluorescence in nuclei, which is our goal, and especially to assess the telomere length. As explained in Chapter I though, such methods usually rely on cultured metaphase nuclei for quantitative FISH [6, 86, 112, 128, 183]. Methods used to automate the segmentation of probes prior to quantitative evaluation include: image smoothing and top-hat transform [122], background subtraction, image smoothing and watershed [86], background subtraction, image smoothing and threshold [112], background subtraction [128], image smoothing and thresholding [139]. These methods, however, are not meant to segment images with the foreground noise

described above, and would segment it as valid signal. Further processing to classify segmented shapes would be required, as in [92, 93]. This require tuning or learning, bringing additional issues of classification to our segmentation task. Instead, we developed a segmentation method robust to foreground noise, based on a novel dome-finding algorithm.

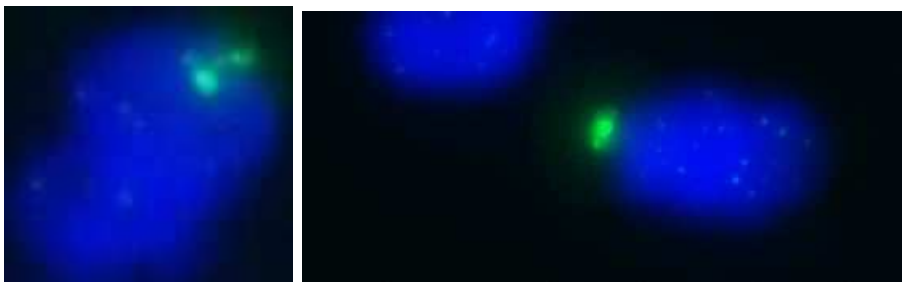

Figure III.2.1: *Examples of foreground noise.*

III.2.1 Dome-finding algorithm

Our new method is based on the following observations. Background noise is caused by random reflections of light towards the optics, and does not reflect any material structure. In the same way, unwashed probes are randomly clustered, and cause random values on the resulting image. Probes attached to telomeres, however, have a consistent spatial structure, reflecting that of telomeres. In interphase nuclei, telomeres are wrapped [24], forming small ovoid structures. Consequently, when imaged with FISH, FITC probes attached to telomeres appear as small spots with a bright centre, due to higher concentration of fluorescent material, and an intensity decreasing away from the centre. This structure of local intensities is consistent for all attached probes, regardless of their actual intensity values. This is what we use to discriminate between valid probes and noise, both background and foreground.

A local maximum is a pixel which value is higher than its 8 nearest neighbours, in our context. Considering a random distribution of integer values in two dimensions, there is no correlation between neighbouring pixels. On such a distribution, the probability of finding a local maximum is equivalent to that of finding the maximum of nine random numbers, *i.e.* $\frac{1}{9} \approx 11\%$. Consequently, in background and foreground regions of FITC images, the proportion of local maxima is approximately 11%. In regions showing probes however, there is one local maximum within the two scores of pixels showing the probe: the proportion of local maxima is around $\frac{1}{20} = 5\%$. We set the average value $8\% = \frac{2}{25}$ as the threshold separating these two proportions. An image region containing more

than 2 local maxima within 25 neighbouring pixels is considered as noise; if it contains 1 or 2 local maxima, it is considered as containing a probe.

Probe segmentation requires more than selecting potential regions of interest, or than finding local maxima. As we are interested in the total probe intensity, we need to segment all the pixels forming a probe signal. Using the landscape metaphor, probes are dome-shaped, circular and no more than 3 pixels in radius. They are centred around a local maximum, in a region containing at most 2 local maxima within 25 pixels.

To segment probes efficiently under these constraints, we use a novel dome-finding algorithm. Briefly, it works as follows: the image is scanned once, and every local maximum is considered as a dome centre. The surrounding pixels are inspected, and marked as part of the dome if they follow a dome-shape criterion. With this marking, the resulting dome will be small in noisy regions and large on probes. Translating the proportion constraint described above into a dome size constraint, only domes of a given size are selected as valid probe segmentation. We now detail these steps.

Dome construction: Around each local maximum, we consider three sets of neighbouring pixels at increasing distances. They approximate the shape of a probe, and are illustrated in Figure III.2.2 by three different shades of gray around the local maximum marked in black. Each set forms a level set of the dome, referring to the original topological definition of level sets, not to the level-set segmentation method. The first level set consists of the 8 closest pixels: $LS_1 = \{p, d_\infty(p, p_M) = 1\}$. In the second level set are the twelve closest pixels that are not already in LS_1: $LS_2 = \{p, p \notin LS_1 \wedge d_1(p, LS_1) = 1\}$. A similar definition holds for the third level sets: $LS_3 = \{p, p \notin LS_1 \cup LS_2 \wedge d_\infty(p, LS_2) = 1\}$. Each pixel in the sets LS_1 and LS_2 is assigned three neighbours, as indicated by the arrows in Figure III.2.2. We refer to them as *downhill neighbours*. When the level sets around a local maximum are inspected, a pixel is marked as part of the dome if its value is higher than its downhill neighbours. Once all pixels in level sets 1 and 2 have been inspected, the constructed dome is defined as the pixels marked.

The use of downhill neighbours in building the dome is motivated by the following reason. A straightforward criterion to build a dome would be: $\min\{LS_i\} \geq \max\{LS_{i+1}\}$. It would only segment domes with circular symmetry though. However when wrapped, telomeres are not perfected spheres, but might be elongated ellipsoids. As a result, the light intensity at one part of the dome might be higher than at the opposite part. Our criterion is robust to such cases, as it is only sensitive to the variations of intensity in subparts of the dome.

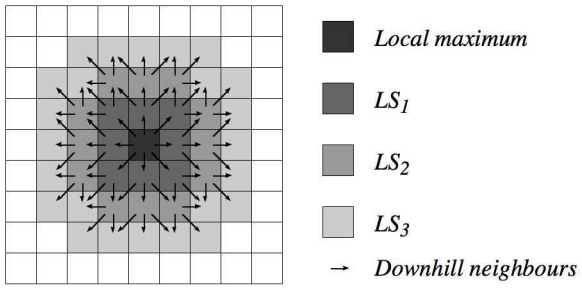

Figure III.2.2: *Dome model: the three level sets around a local maximum are indicated in different shades of gray. All downhill neighbours are indicated with arrows.*

Dome selection: Domes are constructed around every local maximum in the image, but those in noisy regions have to be rejected. The criterion defined above can be translated as follows. Let us consider a 5×5 square of pixels centred on a local maximum. This square either contains:

- One local maximum: the region contains a probe, centred on the maximum, and by construction the dome marks all pixels on it. It should be kept as a valid probe.

- Two local maxima: this is still considered as a region showing probes, so the dome should be kept. However, the pixels in-between the two maxima will follow a saddle shape, and cannot be marked as part of the dome. This interference between the two domes is restricted to one quarter of the dome though (see Figure III.2.3). At most 75% of level sets 1 and 2 can be marked.

- More than two local maxima: the region is now considered as noisy. The combined effect of the two extra local maxima will cause more than one quarter of level sets 1 and 2 to be unmarked.

As a result, we use the following criterion. A dome is kept as segmenting a valid probe if at least 75% of the pixels in LS_1 and at least 75% of those in LS_2 are marked; otherwise it is rejected as noise. Examples of constructed domes are shown in Figure III.2.4: only the one in the middle is kept.

III.2.2 Results and discussion

The categories of segmentation result presented in the introduction and used for the segmentation of nuclei do not correspond well to the segmentation of probes. What is to be evaluated is the total fluorescence segmented within a nucleus, more than the number of probes. Our method prevents undersegmentation and

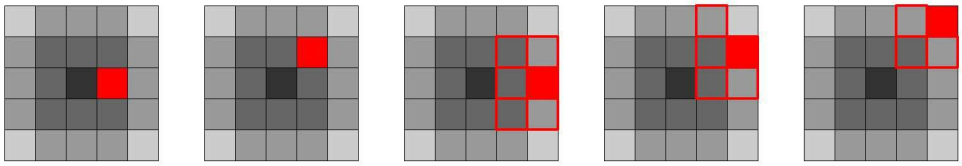

Figure III.2.3: *Pixels affected by the presence of another local maximum, in red: at most one quarter of pixels in level sets 1 and 2 are affected and cannot be marked as part of the dome.*

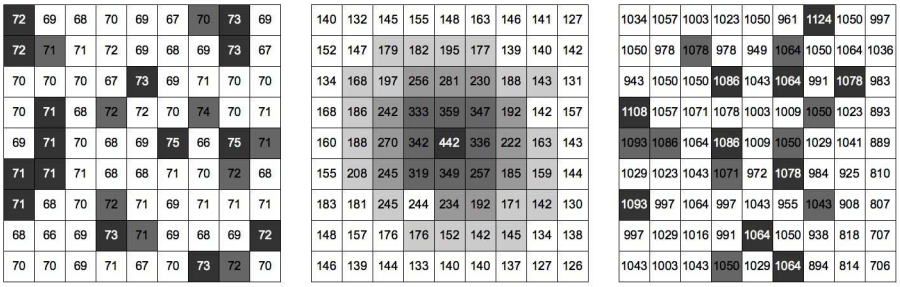

Figure III.2.4: *Domes constructed in image regions containing: background noise (left), probe (middle), foreground noise (right).*

oversegmentation by design, as it keeps probes at a given size. The possible outcomes are simply as follows: a probe is either correctly segmented or missed, and noise may be segmented as a probe. The less severe errors are the segmentation of background noise and the missing of a dark probe. The more severe errors are the missing of a bright probe, and the segmentation of foreground noise.

We do not use Receiver-Operator Characteristic (ROC) curves in this section for the following reasons. ROC curves represent the true positive rate and false positive rate achieved by a classifier when varying one of its parameters. It requires a two-class classifier and supposes that each item can be classified manually into one category. In our case, considering pixel segmentation as a two-class labeling classification is not adapted: while the pixels at the core of a probe are easily distinguishable, some pixels at the edge of a probe may be classified as background or probe by different experts. This amounts to saying that not all the pixel labels have the same significance for the final results. Another possibility would be to consider probe classification as a two-label classification. The first issue with this approach is the definition of a probe: using connected components in the segmented image is bound to fail for methods like the top-hat transform, as can be seen in Figure III.2.6, bottom right-hand corner: nearby probes tend to be merged into single connected component. The second issue is that false positives (noise segmented as probe) falls in two important categories: background noise segmented as probe is not an issue for the application we are considering, while foreground noise segmented as probe is a major problem. In the same vein,

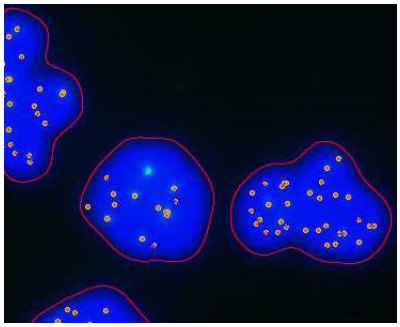

Figure III.2.5: *Example of a probe missed with our dome-finding segmentation method.*

false negatives need to be classified in two categories: missing dark probes is not very important, while missing bright probes is problematic. For these reasons, we ruled out the use of ROC curves to analyse the probe segmentation results. The threshold parameter, set to 75%, was empirically found to offer a good quality of results, based on the severities presented above.

Table III.2.1: *Results of the telomere segmentation.*

Segmentation	Dome-finding	Top-hat
Number of probes	1,000	1,000
Correctly Segmented	993	931
Dark probes missed	5	62
Bright probes missed	2	7

The results of our dome-finding method, as well as a top-hat segmentation method (see Section II.1 on Shape extraction, page 20, for details on the top-hat segmentation), are listed in Table III.2.1. Our method correctly segments 99.3% of probes. An example of missed probe is shown in Figure III.2.5. It performs better than the top-hat segmentation. Figure III.2.6 shows a comparison of the two methods. In addition, our dome-finding method segments background noise as probe with a frequency of about 0.1%, and leaves foreground noise unsegmented. By contrast, the top-hat method never segments background noise, but always segments foreground noise, as illustrated in Figure III.2.7. Our dome-finding algorithm is reliable to segment probes and count them. In the next part we use it in addition to our nucleus finding algorithm to compare the telomeric intensities from different individuals.

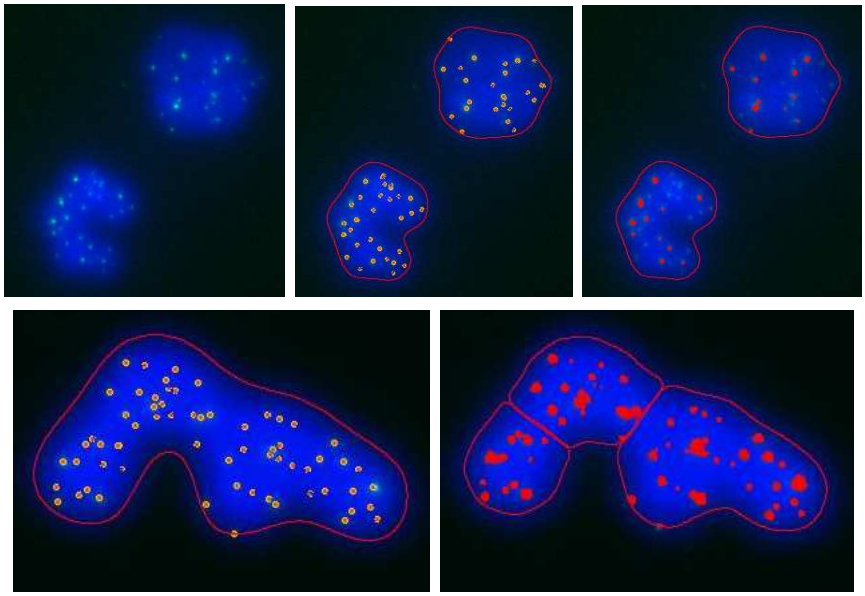

Figure III.2.6: *Comparison of probe segmentations. Top row, from left to right: original image; results of our dome-finding segmentation; results of the top-hat segmentation. Most of the dark probes are missed by the top-hat. Bottom row, left: image segmented with our nucleic and our dome-finding segmentation methods; right: same image segmented with the watershed and the top-hat segmentation. While the nucleus is over-segmented, most of the probes are merged with the top-hat.*

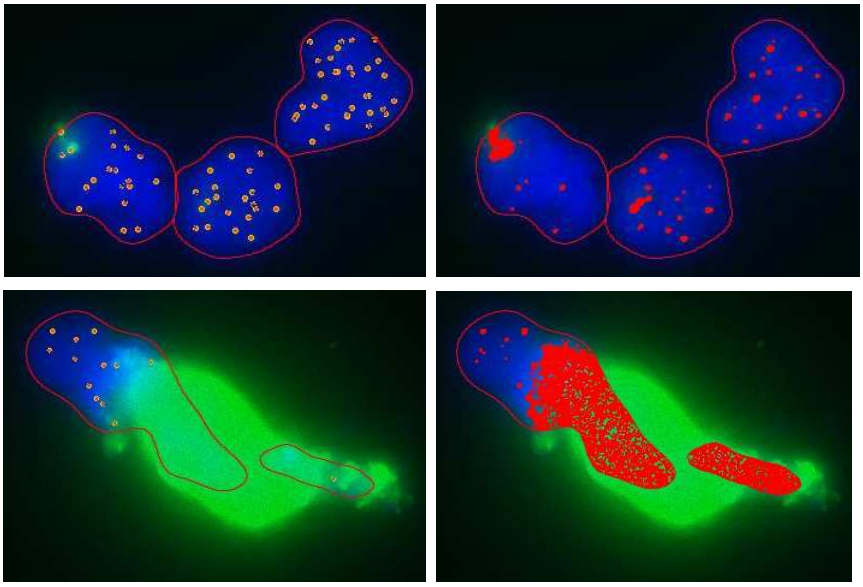

Figure III.2.7: *Probe segmentation on foreground noise. Top row: minor foreground noise; bottom row: major foreground noise. In the two cases our dome segmentation leaves the noise un-segmented (left column), while the top-hat method segments it (right column).*

III.3. Comparison of telomere intensities

III.3.1 Data set and calibration

We now use the two segmentation methods together to proceed to the cytometric task described in Chapter I. The final goal of this task is to identify a fetal nucleus within several thousand maternal nuclei, based on the fluorescent intensity of telomeric probes visible in all the nuclei. Before this can be achieved, we need to evaluate whether probe intensity is significantly different in nuclei sampled from people at different ages.

As a pilot study to assess the reliability of the telomeric probe intensity as an indication of a person's age, four blind trials were conducted, resulting in four sets called MT002, MT004, MT007 and MT024. For each trial, three individuals (except in set MT007 with only two individuals) were sampled for telomeres, which were then processed and imaged in similar conditions. The individuals within each set, named MT0xx-1, MT0xx-2 and MT0xx-3, differ in age. One of them is a foetus, one is an adult female and one (except in set MT007) is an adult male. As a blind trial, we do not known which individual corresponds to which name. The trial consists in processing the images from each individual in the same way, as detailed before, so as to measure the average probe intensity in each nucleus from each individual. Several hundred nuclei are to be segmented for each individual, and the resulting distribution of the average probe intensities will be represented with one histogram per individual. As explained in Chapted I, the telomeric length decreases with a person's age, inducing a decrease of probe intensity, so it is expected that one individual (the foetus) in each set will show higher probe intensities than the other two.

In addition, the imaging quality of the samples can be estimated, using the number of probes segmented per nucleus. With 23 pairs of chromosomes, a typical

Set	*Individual*	*# Images*	*Set*	*Individual*	*# Images*
MT002	MT002-1	228	MT007	MT007-1	247
	MT002-2	198		MT007-2	180
	MT002-3	297			
MT004	MT004-1	152	MT024	MT024-1	70
	MT004-2	273		MT024-2	70
	MT004-3	382		MT024-3	69

Table III.3.1: *Number of images for each individual in our data set.*

nucleus contains 92 telomeres. However, no nucleus contains 92 probe signals. This is mostly because the telomeres tend to cluster [186], and partly because of imaging quality. In particular blur reduces the number of visible and segmentable probes. As a rough quality estimation, nuclei showing above 20 probes can be considered as correctly imaged [186], while the others may suffer from unmarked telomeres, blur or missed segmentation. Again, the distributions of the number of probes segmented per nuclei will be represented with histograms, one per individual in each set. For each individual, one slide of uncultured interphase leucocytes was prepared for FISH imaging: the numbers of images, in pairs DAPI-FITC, available for each individual are listed in Table III.3.1. The whole data set was processed with the segmentation methods described in the previous two sections. Nuclei were segmented first, then the telomeric probes inside them were also segmented.

The FITC probes used attach to small regions of the telomeres: the longer the telomeres, the more probes are attached. However, the probes cannot be used to measure directly telomere length. In interphase nuclei, telomeres are wrapped, and at the scale used for imaging, probes are about two or three pixels in diameter. A change in length by 30% would affect the size of the probe signal by less than a pixel. Instead, the pixel intensity can be used to measure the energy emitted by a probe. Two measures can be performed after segmentation: the average probe intensity f^i and the average background intensity b^i in a nucleus i. Considering two individuals 1 and 2 in a given set, we note these measures respectively f_1^i, b_1^i, f_2^i, b_2^i. Let f_1, b_1, f_2, b_2 be the average values of these measures.

A significant issue arises when measuring pixel intensities to compare different individuals. Even though each individual's sample within a set was processed in the same way, they were imaged separately, at different times. The imaging conditions, such as the surrounding illumination, the excitation intensity or the exposure time may be slightly different for different individuals within a set, with a direct impact on image intensity. Before comparing the probe intensities from different individuals, the FITC intensities f_1, b_1, f_2, b_2 have to be calibrated.

To calibrate segmented FITC images from the different individuals of a set, we use the following model. Considering two individuals 1 and 2, let I_1 and I_2 be their average probe intensities. We model the background fluorescence as additive background noise; since their samples were processed in the same way, we consider that the FITC background has the same average intensity for both of them, and note it B. As a result, the intensity at a probe is $I_1 + B$ for individual 1, and $I_2 + B$ for individual 2, and the background intensity is B for both of them. The excitation intensity and the exposure time induce a multiplicative gain: let α_1 be the gain for individual 1, and α_2 that for individual 2. After segmentation of the FITC images, the average intensities measured in the background of foreground are:

	individual 1	individual 2
background	$b_1 = \alpha_1 B$	$b_2 = \alpha_2 B$
foreground (probe)	$f_1 = \alpha_1 \cdot (I_1 + B)$	$f_2 = \alpha_2 \cdot (I_2 + B)$

(III.3.1)

With this model, calibrating the intensities can be achieved by multiplying the foreground intensities of individual 2 by $\frac{\alpha_1}{\alpha_2}$. This ratio, which we refer to as *calibrating factor*, could be obtained directly from the average background intensities b_1 and b_2, defined in Equation III.3.1. Such a measure would not be precise though, because of the wide range of values taken by the b^i. A more precise measure can be performed as follows.

The values measured after segmentation for individual 1 are f_1^i and b_1^i in each nucleus i. With the model above, the average of the differences $f_1^i - b_1^i$ is $\alpha_1 I_1$. The average of the ratios $\frac{f_1^i}{b_1^i}$ is $\frac{I_1+B}{B}$, so the average of the quantities $\frac{f_1^i}{b_1^i} - 1$ is $\frac{I_1}{B}$. This way, in the two-dimensional graph

$$\left(x = \frac{f_1^i}{b_1^i} - 1 \, , \, y = f_1^i - b_1^i \right) \tag{III.3.2}$$

the slope of a linear interpolation is $\alpha_1 I_1 \cdot \frac{B}{I_1} = \alpha_1 \cdot B$. Plotting the same graph for individual 2 gives access to $\alpha_2 \cdot B$, as the slope of the linear interpolation of the samples. Finally, the ratio of these two slopes gives the calibrating factor $\frac{\alpha_1}{\alpha_2}$ for individual 2.

The graphs described in Equation III.3.2 and the calibrating factors are presented in Figure III.3.1 for the four sets. In each set, an individual *ref* is chosen as a reference, and its measured intensities are not modified. For the other individuals *oth* of the set, the measured intensities f_{oth} and b_{oth} are calibrated, by multiplying them with the corresponding calibration factor $\frac{\alpha_{ref}}{\alpha_{oth}}$, listed in Fig-

ure III.3.1. The calibrated measures are:

	reference individual *ref*	other individual *oth*
background	$\hat{b}^i_{ref} = b^i_{ref}$	$\hat{b}^i_{oth} = \frac{\alpha_{ref}}{\alpha_{oth}} b^i_{oth}$
foreground (probe)	$\hat{f}^i_{ref} = f^i_{ref}$	$\hat{f}^i_{oth} = \frac{\alpha_{ref}}{\alpha_{oth}} f^i_{oth}$

(III.3.3)

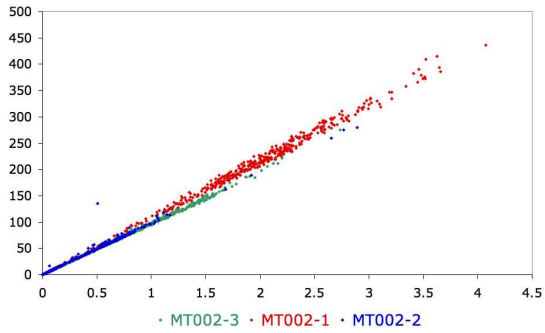

$MT002$	$B\alpha_i \rightarrow$	1	2	3
$B\alpha_j \downarrow$	$\alpha_i/\alpha_j \searrow$	108.22	100.91	97.30
1	108.22	1	0.932	0.899
2	100.91	1.072	1	0.964
3	97.30	1.112	1.037	1

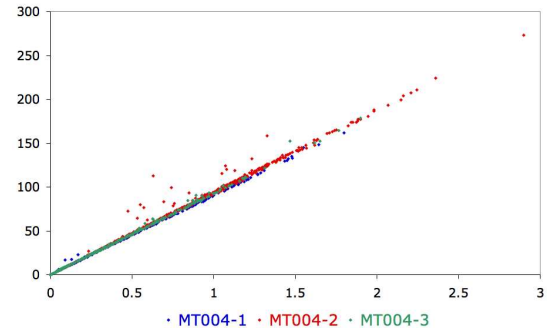

$MT004$	$B\alpha_i \rightarrow$	1	2	3
$B\alpha_j \downarrow$	$\alpha_i/\alpha_j \searrow$	106.01	94.41	93.84
1	106.01	1	0.891	0.885
2	94.41	1.123	1	0.994
3	93.84	1.130	1.006	1

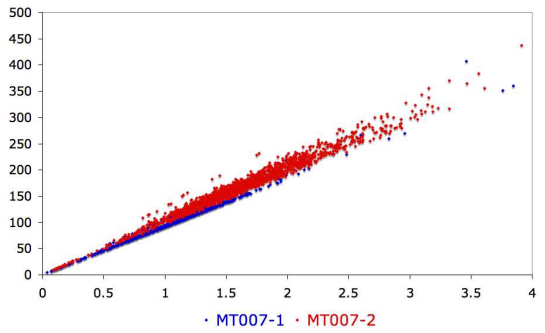

$MT007$	$B\alpha_i \rightarrow$	1	2
$B\alpha_j \downarrow$	$\alpha_i/\alpha_j \searrow$	94.20	103.56
1	94.20	1	1.099
2	103.56	0.910	1

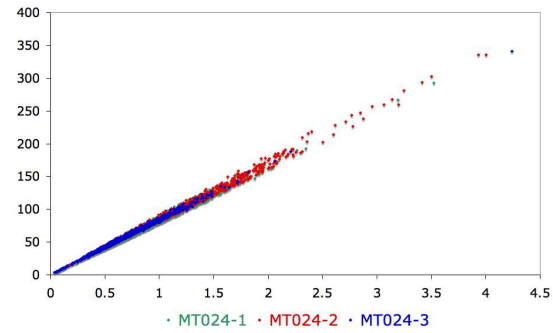

$MT024$	$B\alpha_i \rightarrow$	1	2	3
$B\alpha_j \downarrow$	$\alpha_i/\alpha_j \searrow$	81.36	84.79	83.78
1	81.36	1	1.042	1.030
2	84.79	0.959	1	0.998
3	83.78	0.971	1.012	1

Figure III.3.1: *Calibrating graphics and factors for all four sets. Top of each cell: graph* $\left(x = \frac{f^i_1}{b^i_1} - 1\,,\, y = f^i_1 - b^i_1\right)$ *described in Equation III.3.2. Bottom of each cell: calibrating factors for each individual, based on the ratios of the slopes of the linear interpolations.*

III.3.2 Results and discussion

Once the measures are calibrated for all individuals, two histograms are produced for each individual, and grouped by sets. The first histogram shows the difference

$\hat{f}^i - \hat{b}^i$ per nucleus. Using the model presented above, this quantity is:

$$\hat{f}^i - \hat{b}^i = \alpha_{ref} \cdot I^i \tag{III.3.4}$$

where I^i is the average probe intensity in nucleus i. The factor α_{ref} is unknown, but is constant within a set. This measure can be used to compare the average probe intensities per nucleus for all individuals in a set. The histograms of all individuals are presented in the left column of Figure III.3.2. To evaluate the quality of the images, we also construct the histograms of the number of segmented probes per nucleus, in the right column of Figure III.3.2, as explained in the previous section.

In the set MT002, the number of probes in MT002-3 is below 20 for about two third of the nuclei. Should this individual be left out, for low quality reasons, the differences of calibrated intensities show a clear separation between MT002-1 and MT002-2.

In the set MT004, the imaging quality is poor for MT004-1 and MT004-3, and average for MT004-2 judging from the relatively small number of probes segmented in nuclei. In addition, although it does not appear on the histogram, more than 80% of the nuclei in MT004-3 have a zero average difference of calibrated intensities. This happens when probes are visible as dome structures, but have the same average intensity as the background, due to blur. Consequently, although MT004-2 tend to show brighter probes, those measured are strongly affected by imaging conditions in set MT004.

Set MT007 only contains two individuals. The relatively high number of probes segmented per nucleus for the two individuals indicates a relatively good imaging quality. Probes in MT007-2 are generally brighter than in MT007-1. Actually, because of practical issues, MT007-2 was imaged several days after its preparation. As a result, the fluorescence of probes had reduced before imaging. This causes the differences of calibrated intensities to shift towards lower values, and increase the overlap with MT007-1. It is expected that without the imaging delay, the overlap would have been reduced.

Finally, all three individuals in set MT024 have an average imaging quality. Although less nuclei were segmented in MT024-2 than in the other cases, they tend to show brighter probes.

To conclude, judging from the histograms on the left of Figure III.3.2, showing the differences of calibrated foreground and background intensity per nucleus, one individual in each set appears to have brighter probe signals than the others. They are MT002-1, MT004-2, MT007-2 and MT0024-2, shown in red. However, there is still overlap with the other individuals. One cause is the imaging quality, in particular recurring blur in FITC images. Although these results show a promising trend, more data from more individuals would be needed before

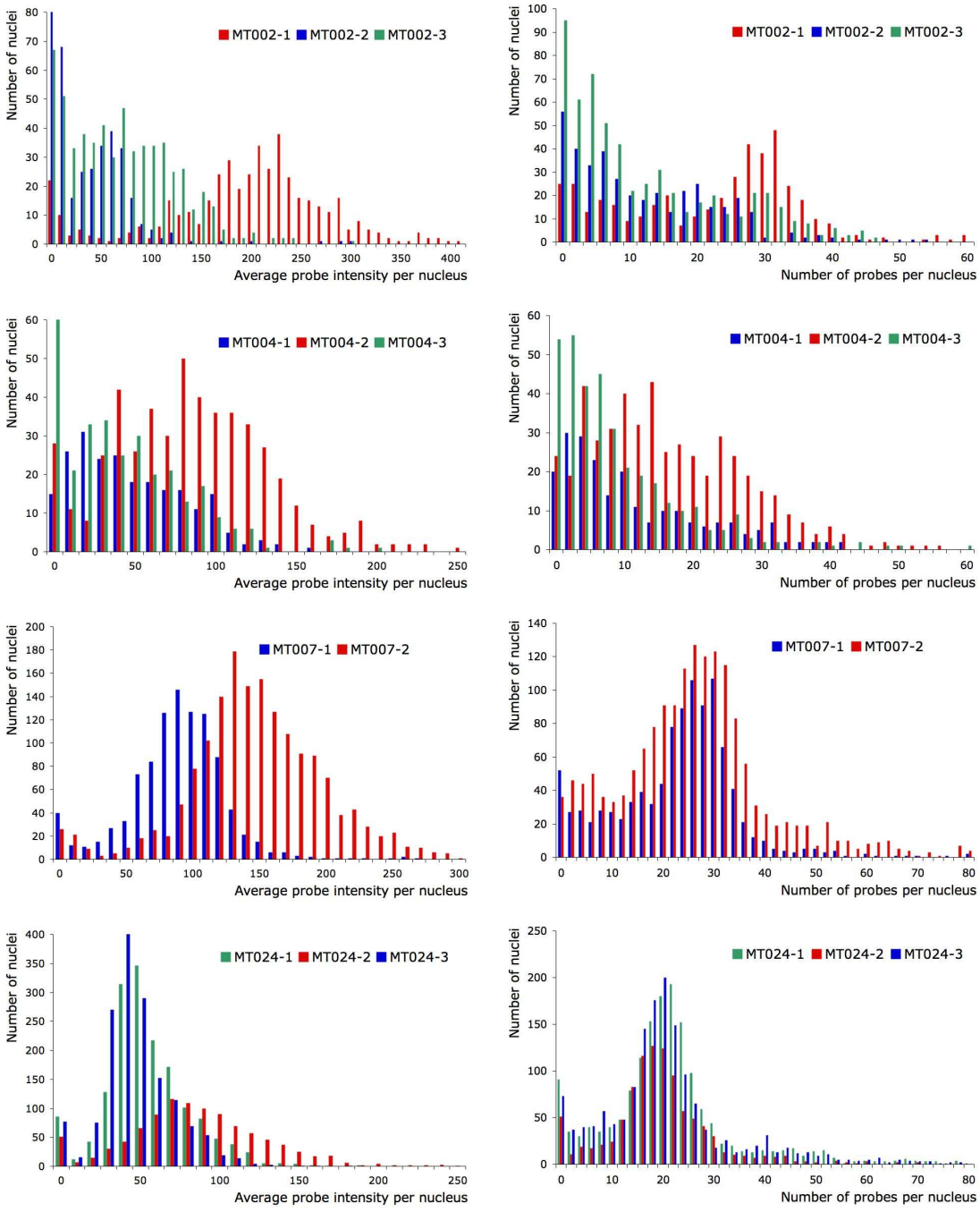

Figure III.3.2: *Calibrated probe intensity and number of probes per nucleus, for the four blind trials. Left column: histogram of the average probe intensity per nucleus, in arbitrary units. In each set the distribution of one individual (shown in red) is centred on higher intensities than the other individuals, proving it contains brighter probes. Right column: histogram of the number of segmented probes per nucleus. Nuclei with less than 20 probes suffer from low imaging quality, and their average probe intensity is unreliable. This is especially the case in MT002 and MT004.*

drawing conclusions on the quality of telomere probe intensity as a measure to distinguish individuals' ages.

Summary

In this chapter we have detailed our new segmentation methods, presented a quantitative comparison of our nucleic segmentation with the widely used watershed method, and shown an application of our methods for medical research. The nucleic segmentation method we developed is based on a new model of the image histogram, achieves a 99.3% accuracy and, to the best of our knowledge, is more robust and automatic than previously published work on this field. As for the telomere probes, our method is robust against all sources of noise, and is also 99.3% accurate. The application presented here shows that the telomere probe intensity is a potentially promising criterion to differentiate individuals' ages, but it requires good imaging conditions. In particular, each sample should be processed and imaged similarly and during the same period of time. Although major improvements can be achieved with a higher imaging quality, other post-segmentation techniques can be devised to increase the quality of the results. Selecting nuclei based on their usability is one approach, which we present in Section V.3 as future work.

Regarding computer vision, the nucleus segmentation method developed was evaluated on our whole data set, and other methods on a subset. These evaluations were performed visually by the author, based on some examples of correct segmentation provided by cytometrists. This is a time-consuming process, which depends on the evaluator's subjectivity. In the next chapter, we present a novel framework to define segmentation references, possibly combine multiple references from different users, and automatically evaluate a segmentation method against these references, with a single measure.

Chapter IV

Evaluation of a Segmentation Method

As explained in the introduction, we are interested in evaluating segmentation methods in terms of *discrepancy* [201]. It consists in comparing a segmented shape with a reference. In this chapter we address the issues related to discrepancy evaluation, in a medical imaging context, detailed in Section I.2.3. Briefly, the four issues we identified are:

- A need for quantitative as well as qualitative description of segmentation results, with the following categories: correct, over- and under-segmented, missed and noisy segmented objects.

- A definition of correctly segmented object which is less strict than a perfect match with a reference: in particular partial volume effect and blur can cause an object's boundaries to span several pixels, so a segmented object may be correct while differing from the reference by several pixels.

- A possibility to combine multiple references into a single one: references drawn by different users or by one user at different times may differ slightly at some parts of an object, yet eventually only one reference is to be used.

- A clarification in the presentation of evaluation results: for example the proportion of correctly segmented references may differ from the proportion of objects correctly segmenting a references, though both may be called success rates.

We introduce a novel method, called *Confidence Maps Estimating True Segmentations (Comets)*, to store segmentation references for medical imaging, combine multiple references, and measure the discrepancy between a segmented object and a reference. The key novelty of our model is to store local confidence factor along a reference. Local confidence is computed from user input, and is used to define a new discrepancy measure. To help resolve an ambiguity inherent to evaluation, we also introduce two complementary ways to present discrepancy results: the reference and user viewpoints. We show that, with a single measure, our method allows a qualitative and quantitative evaluation of a segmentation method, and compare it with existing metrics.

We start with a review of existing work addressing the issues mentioned above, and then present our model, *Comets*. We detail how to encode one reference, how to combine multiple references and how to evaluate a segmentation method. We also compare our evaluation method with existing metrics.

IV.1. Existing work

IV.1.1 Measures for discrepancy evaluation

Given a reference and a segmented shapes, there are several ways to assess their match. Different measures have been published and used. Many of them are based on low-level vision metrics. Two such families of measures are based on ratios of numbers of pixel (area-based), and on distances between shapes (distance-based).

Let C be a reference, and S be a corresponding segmented shape. Let A_C be the area of C in pixels, and $\{C_i\}_{1\leq i\leq n}$ the set of n pixels at the border of C. Similarly, let A_S be the area of S, and $\{S_j\}_{1\leq j\leq m}$ the set of m pixels at the border of S. Examples of area-based measures are:

Sensitivity, RUMA: true positive ratio [185], or Relative Ultimate Measurement Accuracy [54, 156, 202]:

$$Sensitivity = RUMA = \frac{A_{S\cap C}}{A_C} \ . \tag{IV.1.1}$$

Specificity: true negative ratio [185]:

$$Specificity = \frac{A_{Image-S\cup C}}{A_{Image-C}} \ . \tag{IV.1.2}$$

RAO: Relative Area Overlap [54]:

$$RAO = \frac{A_{S\cap C}}{A_{S\cup C}} \ . \tag{IV.1.3}$$

DSC: Dice Similarity Coefficient [205]:

$$DSC = \frac{2 \times A_{S\cap C}}{A_S + A_C} \ . \tag{IV.1.4}$$

Performance: [102]:

$$Performance = 1 - \sqrt{w^2(1-TP)^2 + (1-w)^2 FP^2}\,, \tag{IV.1.5}$$

where: $w = \frac{A_C}{A_{Image}}$ is the proportion of foreground pixel in the image, $TP = \frac{A_{S \cap C}}{A_C}$ is the true positive ratio, and $FP = \frac{A_{S-C}}{A_{Image-C}}$ is the false positive ratio.

Each measure indicates a fraction of misclassified pixels: for instance sensitivity gives an idea of oversegmentation, and specificity of undersegmentation; others combine the two. However, the severity of the segmentation errors can be difficult to evaluate based on these ratios. In particular, the specificity depends on the background size, which in our case is more than a million pixels: even a severe nucleus segmentation error will have a high specificity. Also, the geometry of the misclassified regions is not taken into account: this makes a tolerance margin difficult to use with the area-based measures. Pixels ratios depend on the object sizes, some even on the image size, and do not easily take into account tolerance margins.

Examples of distance-based measures are:

Hausdorff Distance: [11, 54, 87, 136]:

$$Hauss_{Max} = \max_{1 \le i \le n} \left\{ \min_{1 \le j \le m} \{d(C_i, S_j)\} \right\} \tag{IV.1.6}$$

where $d(P, Q)$ is the Euclidian distance between pixels P and Q.

Hausdorff Mean Distance and Standard Deviation: [87, 136]:

$$Hauss_{Mean} = \frac{1}{n} \sum_{i=1}^{n} \min_{1 \le j \le m} \{d(C_i, S_j)\} \tag{IV.1.7}$$

$$Hauss_{StdDev} = \frac{1}{n(n-1)} \sum_{i=1}^{n} \left(\min_{1 \le j \le m} \{d(C_i, S_j)\} - Hauss_{Mean} \right) \tag{IV.1.8}$$

Distances measures depend directly on the geometry of the misclassified regions: it is easier to include tolerance margins around a reference segmentation. However, these distances are measured in pixels. Interpreting their values to infer the severity of an incorrect segmentation require to know the typical size of an object of interest, which may vary across samples. Distinguishing between over- and under-segmentation is difficult with the definitions above, as the distance between pixels is symmetric. It may be done by introducing a sign in the computation:

$$d(C_i, S_j) = \begin{cases} +\|C_i - S_j\|_2 & \text{if } S_i \in C \\ -\|C_i - S_j\|_2 & \text{else} \end{cases} \tag{IV.1.9}$$

though it requires extra care when computing the maximum, mean and deviation of the distance distribution between the shapes.

The measures above do not require any parameter, and are straightforward to compute. However, none of them seems to be satisfying as a standalone measure: at least two needs to be combined to obtain quantitative and qualitative evaluation of a segmentation result. Interpretation of quantitative results requires an external reference as well.

Other measures are based on fuzzy systems [43, 174]. They rely on a fuzzy extension of segmentation, where pixels at the border of objects are assigned fractional labels. The measures defined above can be extended in a fuzzy framework. However, these measures introduce parameters, such as the extent of fuzzy boundaries and the relative weights of different labels. These parameters have to be tuned, which may add subjectivity the evaluation process, and raises issues when interpreting and comparing evaluation results.

Finally, an approach to evaluation has been to use several metrics at the same time [54, 87, 136, 174]. Though it gives more data, it leads to more questions on how to combine them, or which ones are more informative. Basically, it amounts to representing segmentation results in a space with many dimensions, some restricted to values between 0 and 1, some to positive values, other to any values, and each one having its own external reference for interpretation. It adds to the complexity of evaluating a single segmentation method, but also of comparing different methods, or tuning of a method's parameters. In this chapter we introduce a single measure, which can be interpreted qualitatively and quantitatively with no external reference.

IV.1.2 Combination of multiple references

Manual references, however useful for evaluation, are subject to inter- and intra-user variability. Different experts, or one expert at different times, may disagree on some parts of the objects' boundaries, while agreeing on others. This calls for a way to combine multiple segmentations into a single reference. Ideally it should keep as much expert knowledge as possible.

Different methods have recently been published. Rohlfing *et al.* [145] average the Euclidian distances between the shapes, as in [173]. Kim *et al.* [76] use Weiner measures instead of Euclidian. The results obtained, however, do not reflect how different the expert segmentations were, by treating equally the zones of agreement and disagreement between experts. In case two references differ significantly in one region, the constructed reference will be far from both, and the evaluation measure of the original references will be high, even though both

may be correct.

In an area-based approach, STAPLE [185] optimises the references' specificities and sensitivities, based on a Markov Random Field (MRF). These area-based ratios depend on the object and image sizes though, and MRF are used by some segmentation methods [13, 31]. It requires the tuning of many parameters, uses criteria that are size-dependent, and violates the independence criterion described by Lehmann in [91]. It may be biased favorably for segmentation methods based on MRF, and for area-based discrepancy measures.

In this chapter we present a novel way to encode expert references, and use it to define a new single metric for discrepancy evaluation, size-independent, parameter-free and intuitive to interpret. We detail how to combine multiple references with *Comets*, with no parameter nor segmentation model, while keeping more information than a single shape can.

IV.2. *Comets*: a novel method of referencing

We present our novel model, *Confidence Maps Estimating True Segmentation*, *Comets*. We explain how to encode a segmentation reference with local confidence, and how to visualize it with confidence maps. Then we detail how to combine multiple segmentations using local confidence. Finally we present the new discrepancy metrics associated with our model.

IV.2.1 Encoding a reference with local confidence

The user input consists in drawing a continuous border around the object, and selecting pixels inside and outside the object (see Figure IV.2.1, left, and Figure IV.2.2, middle), according to the following criteria. We refer to the pixels on the border as *edge pixels*, and to the pixels selected around the object as *outer* and *inner limit pixels*. Outer limit pixels (respectively inner limit pixels) are examples of pixels closest to the border that the user is certain belong to the background (respectively to the object). The number of limit pixels to select depends on the local variations of confidence, the local variations of blur, or the presence of touching objects. They are used only to define the confidence that the border is locally correct. Their selection is thus easier and less critical than landmarks.

Using this user input, the local confidence factors are computed as explained below and illustrated in Figure IV.2.1. Every edge pixel is assigned an *inner* and an *outer* confidence factor, respectively IC and OC. First, for the edge pixels E that are the closest to outer limit pixels, at distance d (see Figure IV.2.1, middle):

$$OC(E) = d \tag{IV.2.1}$$

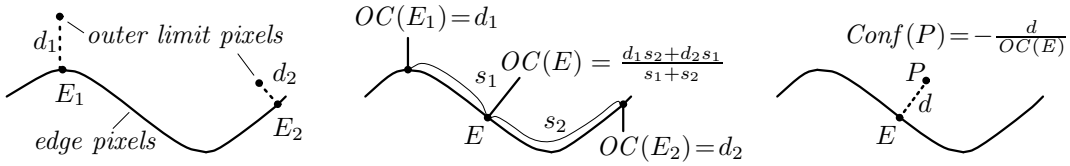

Figure IV.2.1: *Construction of a* Comets. *Left: User input. Middle: Outer Confidence factors assigned to the edge pixels closest to outer limit pixels then interpolated linearly along the curvilinear coordinate. Right: Confidence of any outside pixel P, based on the Outer Confidence factor of the closest edge pixel.*

Then, the outer confidence factors of the remaining edge pixels are computed using the existing values, with a linear interpolation along the curvilinear distance between the edge pixels. Let E be an edge pixel, and let E_1 and E_2 be the pixels already having outer confidence factors d_1 and d_2 closest to E, at curvilinear distance s_1 and s_2 (see Figure IV.2.1, middle). The outer confidence factor of E is defined as:

$$OC(E) = \frac{d_1\, s_2 + d_2\, s_1}{s_1 + s_2} \tag{IV.2.2}$$

The same method of sampling and interpolation is used to compute the inner confidence factor.

Once the confidence factors are computed, the confidence map of the reference is computed by assigning a confidence *Conf* to every pixel P. If P is an edge pixel,

$$Conf(P) = 0 \tag{IV.2.3}$$

If P is inside the shape, let E be the edge pixel closest to P, at distance d:

$$Conf(P) = \frac{d}{IC(E)} \tag{IV.2.4}$$

Finally, if P lies outside the shape, and the closest edge pixel is at distance d (see Figure IV.2.1, right):

$$Conf(P) = -\frac{d}{OC(E)} \tag{IV.2.5}$$

Qualitatively, the confidence assigned to any pixel P can be interpreted as:

$$\begin{cases} \text{if } \ Conf(P) \geq 1 & : \text{P is strongly believed to be part of the object} \\ \text{if } \ -1 < Conf(P) < 1 & : \text{P is believed to be on or close to the border} \\ \text{if } \ Conf(P) \leq -1 & : \text{P is strongly believed to be out of the object} \end{cases}$$

Quantitatively, the higher $|Conf(P)|$, the more confident the expert is that P belongs to the object or to the background. The pixels with low confidence, between -1 and 1, form a band around the object border (see white band on Figure IV.2.2, right, and Figure IV.2.3, right). The band width reflects the expert's local confidence in the true border location: the narrower the band is

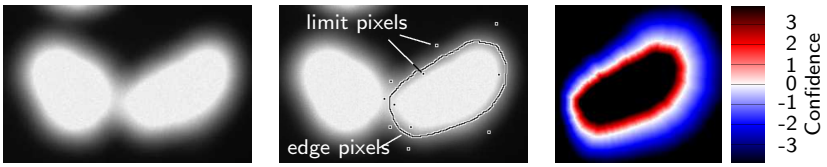

Figure IV.2.2: *Construction of a* Comets. *Left: original image. Middle: user input. Right: the corresponding* Comets.

locally, the more confident the expert is that the border drawn corresponds to the actual border.

With the user input and formulas detailed above, single references with local confidence are encoded as *Comets*. For storage optimization, only the edge pixels' coordinates and confidence factors are stored. The actual confidence map can be recomputed when needed, at any size, with the construction above. We now describe how to combine multiple segmentations of an object with *Comets*.

IV.2.2 Combining multiple segmentations into a single reference

Our novel approach to combine multiple segmentations is to weight them with the local confidences. This is done by averaging the confidence maps defined above. Let $\{C_i\}_{1\leq i\leq n}$ be the set of n expert segmentations to combine, encoded as *Comets*. Let

$$\Omega = \{P\,,\, \exists\, i : Conf_i(P) \geq -1\} \tag{IV.2.6}$$

where $Conf_i(P)$ is the confidence of pixel P with respect to C_i. All pixels outside Ω are confidently considered as background by all the experts, so they are discarded for the rest of the construction. We define the final confidence map on the domain Ω as the average of all the experts' confidence maps:

$$\forall P \in \Omega, Conf(P) = \frac{1}{n}\sum_{i=1}^{n} Conf_i(P)\ . \tag{IV.2.7}$$

We define the set of final edge pixels $\mathcal{E}$, the set of final outside confidence pixels $\mathcal{O}$, and the final inside confidence pixels $\mathcal{I}$ as:

$$\mathcal{E} = \{P \in \Omega : Conf(P) = 0\} \tag{IV.2.8}$$

$$\mathcal{O} = \{P \in \Omega : Conf(P) = -1\} \tag{IV.2.9}$$

$$\mathcal{I} = \{P \in \Omega : Conf(P) = 1\} \tag{IV.2.10}$$

The confidence factors of the final edge pixels are then computed as detailed in Section IV.2.1. An example of segmentation combination is shown in Fig-

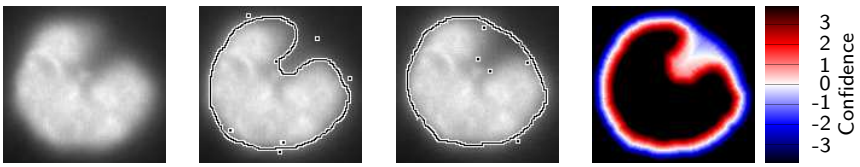

Figure IV.2.3: *Combining multiple segmentations. From left to right: original image; input from expert 1; input from expert 2; resulting average* Comets*. The zones of disagreement have lower confidence, as reflected by the width of the white band around the border.*

ure IV.2.3. Notice that the zones of disagreement receive a lower confidence that the zones of agreement.

IV.3. Evaluating a segmentation method with *Comets*

We start by defining the discrepancy measure associated to *Comets*, for a single segmented object against a single reference. We show the results obtained on a test data set, to compare different discrepancy measures. Then, we detail how to present complete results of a segmentation method, involving several objects against several references, from a *reference* and from a *user viewpoint*. Finally we illustrate how *Comets* can be used to tune a segmentation method's parameters based on a large number of references.

IV.3.1 Evaluation of a single segmented object

Let C be a reference encoded as *Comets*, with confidence $Conf$, and let $Obj_C = \{P : Conf(P) \geq 0\}$ be the set of pixels referenced as the object. Let S be the set of pixels segmented as the object, and $Mis = (S \cup Obj_C) - (S \cap Obj_C)$ the set of mislabeled pixels. The segmentation error of S against C is defined as:

$$error(S, C) = \begin{cases} \infty \text{ if } S \cap Obj_C = \emptyset \\ Conf(P_0), P_0 = \arg\max_{P \in Mis}\{|Conf(P)|\} \text{ else.} \end{cases} \quad \text{(IV.3.1)}$$

Intuitively, if there is no overlap between the segmented object and the reference, they are not related and the error is ∞. Otherwise, mislabeling pixels of low confidence only (near the object boundary) leads to a small error, while mislabeling higher confidence pixels causes a greater error. Moreover, the value of this error can be interpreted in terms of qualitative segmentation error [66], as follows. A shape with error 0 is a perfect match for the reference. An error within -1 and 1 indicates that only pixels of low confidence were mislabeled: the segmentation is considered correct. An error greater than 1 shows that object pixels were labeled as background, so the shape is over-segmented. An error below -1 is due to

background pixels labeled as object: the shape is under-segmented. The absolute value of the error reflects the severity of the mismatch.

IV.3.2 Comparison with other measures

We compare the *Comets* error measure, defined in Equation IV.3.1, with the eight discrepancy measures described in Section IV.1, in Equations IV.1.1 to IV.1.8. The data set we used for this comparison was built as follows. We manually defined 110 references, from cytometry images, encoded as *Comets*. On the same images we also manually defined five sets of segmented shapes, as follows. In set (a) each shape is correct, though slightly different from the reference; in (b) each shape includes a small amount of background all around the object; in (c) each shape includes a large amount of background at one part of the object, and is correct elsewhere; in (d) each shape excludes a small part of object all around it; in (e) each shape excludes a large part of object at one place, and is correct elsewhere. Examples are shown in Figure IV.3.1.

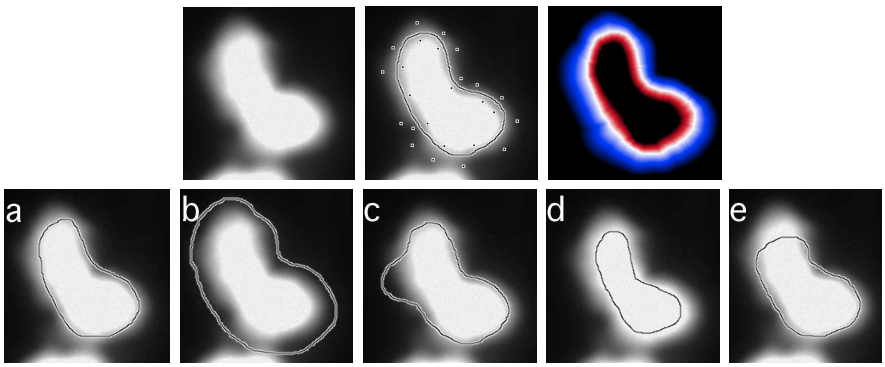

Figure IV.3.1: *Examples of shapes used for the comparison of evaluation measures. Top row, left to right: original image; user input; resulting reference encoded as* Comets*. Bottom row, left to right: correct object in set a; oversegmented object in set b; oversegmented object in set c, undersegmented object in set d; undersegmented object in set e.*

Set a is correct, sets b and c are two types of over-segmentation, sets d and e are two types of under-segmentation. We compare the segmented shapes in each set to the references, using the *Comets* error and existing methods, either on their own or in pairs. The results are shown in Figure IV.3.2.

It appears that all sets are distinguishable using the single *Comets* error. In particular set a results in values between -1 and 1. Area-based measures, namely specificity, sensitivity, RAO, RUMA, DSC and Maddah's performance, can distinguish between a local error (sets c and e) and a generalized error (sets b and d), with more or less overlap. However, they cannot distinguish clearly between

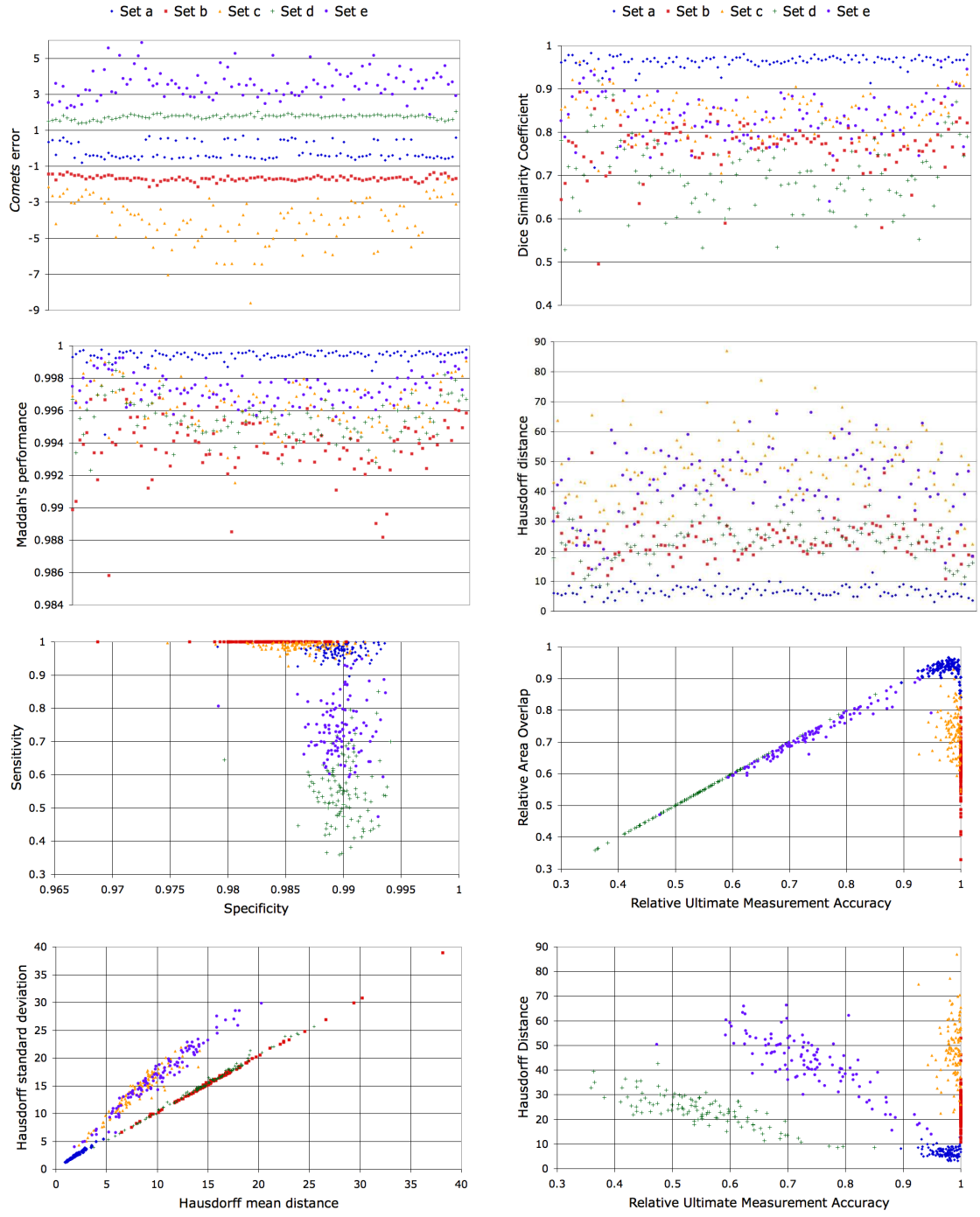

Figure IV.3.2: *Results of the comparison of evaluation methods. All the values plotted are defined in Equations IV.1.1 to IV.1.8 and IV.3.1. Top two rows: single evaluation measures. Bottom two rows: pairs of evaluation measures. On these graphs only the* Comets *error measure (on the top left) shows a clear separation of all five sets.*

under-segmentation (sets b and c) and over-segmentation (sets d and e). Conversely, Hausdorff-distance based measures can perform the opposite distinctions. This prevents distinguishing between over- and under-segmentation. Also, even though most results in set a are below all other sets, there is no threshold value separating them. Yet, combining them may not be enough to distinguish all cases. At least three of these discrepancy measures seem necessary, on this data set, to separate clearly the five sets.

IV.3.3 Evaluation of a segmentation method

The measure defined in Equation IV.3.1 can be used to evaluate a segmentation method, as follows. Let $\{C_i\}_{1\leq i\leq n}$ be the n references, and $\{S_j\}_{1\leq j\leq m}$ the m segmented shapes returned by the method to evaluate. Let EM be the $n \times m$ error matrix defined as:

$$EM(i,j) = error(S_j, C_i) \tag{IV.3.2}$$

Row i lists the errors of the method against reference C_i; if it is filled with ∞, C_i is missed. Similarly, column j shows the errors of the segmented shape S_j; if it is filled with ∞, S_j is noise.

As an illustration, the error matrix for the example in Figure IV.3.3 is:

$$EM = \Big(error(S_j, C_i)\Big)_{i,j} = \begin{array}{c} \left(\begin{array}{ccccc} 0 & \infty & \infty & \infty & \infty \\ \infty & 5 & 15 & \infty & \infty \\ \infty & \infty & \infty & \infty & \infty \end{array}\right) \begin{array}{l} \leftarrow C_1 \\ \leftarrow C_2 \\ \leftarrow C_3 \end{array} \\ \begin{array}{ccccc} \uparrow & \uparrow & \uparrow & \uparrow & \uparrow \\ S_1 & S_2 & S_3 & S_4 & S_5 \end{array} \end{array} \tag{IV.3.3}$$

As explained in Section I.2.3, there is an inherent ambiguity when presenting evaluation results. For clarification, we differentiate between a *reference viewpoint* and a *user viewpoint*. From a reference viewpoint, what matters is to assess how well each reference is segmented. The score obtained by reference C_i is the score with the lowest absolute value in row i in the error matrix. Formally:

$$score_{Ref}(C_i) = EM(i, j_0) \text{ where } j_0 = \arg\min_{1\leq j\leq m} \{|EM(i,j)|\} \tag{IV.3.4}$$

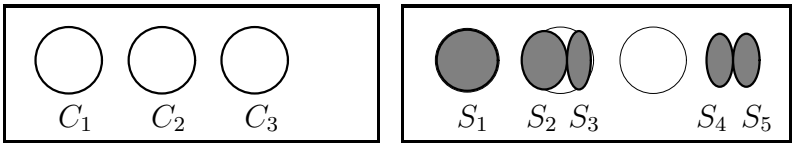

Figure IV.3.3: *Example of segmentation, to illustrate user and reference viewpoints. Left: image with three references C_i. Right: same image with five segmented objects S_j.*

These n scores can be interpreted in terms of correct, under- and over-segmented, and missed references, using the score sign and value as explained above. However, they do not account for the segmented objects classified as noise (columns filled with ∞). To do so, we add the following scores (negative to distinguish from missed references):

$$score_{Ref}(S_j) = -\infty \text{ if } \min_{1 \leq i \leq n} \{EM(i,j)\} = \infty \tag{IV.3.5}$$

As an example, consider Figure IV.3.3 and the error matrix in Equation IV.3.3. The score of the segmentation method, from a reference point of view as defined in Equations IV.3.4 and IV.3.5, is constructed as follows:

$$\left.\begin{array}{c} \begin{array}{ccccc} & & & & \textit{min} \\ \left(\begin{array}{ccccc} 0 & \infty & \infty & \infty & \infty \\ \infty & 5 & 15 & \infty & \infty \\ \infty & \infty & \infty & \infty & \infty \end{array}\right) & \begin{array}{c} \rightarrow 0 \\ \rightarrow 5 \\ \rightarrow \infty \end{array} \\ \begin{array}{ccc} \textit{empty} & \downarrow & \downarrow \\ \textit{columns} & -\infty & -\infty \end{array} & \end{array} \end{array}\right\} score_{Ref} = [\,0,\, 5,\, \infty,\, -\infty,\, -\infty\,]$$

Another way to interpret evaluation results, from a user viewpoint, is to assess how well each segmented object fits a reference. It shows how many segmented objects match a reference, or how many cause oversegmentation. The score obtained by a segmented object S_j is the entry with the lowest absolute value in column j of the error matrix, defined as:

$$score_{User}(S_j) = EM(i_0, j) \text{ where } i_0 = \arg\min_{1 \leq i \leq n} \{|EM(i,j)|\} \tag{IV.3.6}$$

Again these m scores can be interpreted in terms of correct, under-, over-, and noisy segmentated objects. Since they do not account for the missed references, we add the following scores:

$$score_{User}(C_i) = -\infty \text{ if } \min_{1 \leq j \leq m} \{EM(i,j)\} = \infty \tag{IV.3.7}$$

Using Figure IV.3.3 and the error matrix in Equation IV.3.3, the score from a user viewpoint defined in Equations IV.3.6 and IV.3.7, is constructed as:

$$\left.\begin{array}{c} \begin{array}{ccccc} \left(\begin{array}{ccccc} 0 & \infty & \infty & \infty & \infty \\ \infty & 5 & 15 & \infty & \infty \\ \infty & \infty & \infty & \infty & \infty \end{array}\right) & \begin{array}{c} \textit{empty} \\ \textit{lines} \\ \rightarrow -\infty \end{array} \\ \begin{array}{ccccc} \textit{min}\downarrow & \downarrow & \downarrow & \downarrow & \downarrow \\ 0 & 5 & 15 & \infty & \infty \end{array} & \end{array} \end{array}\right\} score_{User} = [\,0,\, 5,\, 15,\, \infty,\, \infty,\, -\infty\,]$$

and can be interpreted qualitatively as follows. From a reference viewpoint, one reference is perfectly segmented, one is severely over-segmented, one is missed,

and two non-existing object are segmented. From a user viewpoint, one segmented object fits exactly a reference, two severely oversegment references, two are noise, and one reference is missed. In practice, error matrices are very sparse, and only require storing in the order of n entries.

IV.3.4 Tuning of a segmentation method

In this section we illustrate how the evaluation method presented above can be used to tune a segmentation method's parameters based on a large number of references. We use our nucleic segmentation method, presented in Chapter III. In a first round of experiments, we tune the proportion values used to initialise the EM algorithm, as listed in Table IV.3.1. In a second round, we tune the total number of iterations of the EM algorithm. Finally, in a third round of experiments we tune the maximum number of components allowed in the EM algorithm. More details on these parameters are provided in Section III.1.2 page 66.

We defined 250 *Comets* references, as detailed above, on a subset of images, and use these objects to tune the parameters. For each round of experiments, we choose a set of parameter values as a control and perform the segmentation. We measure the *Comets* error for each reference i, and note it $score_{Ref}(C_i^{ctr})$. We then choose a set s of parameters values, and segment the reference images again. For each reference i the *Comets* error (from a reference viewpoint) is noted $score_{Ref}(C_i^s)$. For each reference i we then compute the ratio:

$$\rho_i^s = \frac{score_{Ref}(C_i^s)}{score_{Ref}(C_i^{ctr})} \tag{IV.3.8}$$

These ratios can be interpreted in the following way:

$$\begin{cases} |\rho_i^s| \leq 0.5 & : \text{the segmentation is better with parameter values } s \\ 0.5 < |\rho_i^s| \leq 1.5 & : \text{the segmentation is similar to the control} \\ |\rho_i^s| > 1.5 & : \text{the segmentation is worse with parameter values } s \end{cases}$$

The threshold values 0.5 and 1.5 are somewhat arbitrary; the whole plots of ρ_i^s values are available for comparison.

The parameter values used in our experiments are listed in Tables IV.3.2, IV.3.3 and IV.3.4. The results are presented in Figure IV.3.4.

The first round of experiments show that with the parameters in Set 5, the proportion of nuclei having a worse segmentation is the lowest, while the proportion of nuclei having a better segmentation is the highest. We keep these values for the rest of the experiments, as a control for the second round. In that round, with the parameters used in Set 11, the proportion of nuclei with a better

Table IV.3.1: *Parameters of our segmentation method to be tuned: Initial values used in the EM algorithm.*

Intensity	$0 \ldots \frac{1}{n+2} I_{max}$	$\frac{1}{n+2} I_{max} \ldots \frac{2}{n+2} I_{max}$	$\frac{j+1}{n+2} I_{max} \ldots \frac{j+2}{n+2} I_{max}, 1 \leq j \leq n$
$p_{NIB}(I)$	P_0	0.1	0
$p_{IB_i}(I)$	$(1 - P_0)/n$	$0.9/n$	P_1/n
$p_{N_i}(I)$	0	0	P_2 if $i = j$, $P_3/(n-1)$ else

Table IV.3.2: *Parameter values in the first experiment: Initial values used in the EM algorithm.*

	Ctr.	Set 1	Set 2	Set 3	Set 4	Set 5	Set 6	Set 7	Set 8
P_0	1	0.9	0.9	0.9	0.9	0.9	0.9	0.9	0.9
P_1	0	0	0	0	0.1	0.2	0.1	0.2	0.2
P_2	1	1	0.9	0.8	0.9	0.8	0.8	0.6	0.7
P_3	0	0	0.1	0.2	0	0	0.1	0.2	0.1
iterations	100	100	100	100	100	100	100	100	100
n_{max}	5	5	5	5	5	5	5	5	5

Table IV.3.3: *Parameter values in the second experiment: Number of iterations in the EM algorithm.*

	Ctr.	Set 9	Set 10	Set 11	Set 12
P_0	0.9	0.9	0.9	0.9	0.9
P_1	0.2	0.2	0.2	0.2	0.2
P_2	0.8	0.8	0.8	0.8	0.8
P_3	0	0	0	0	0
iterations	100	50	150	200	250
n_{max}	5	5	5	5	5

Table IV.3.4: *Parameter values in the third experiment: Maximum number of components in the EM algorithm.*

	Ctr.	Set 13	Set 14	Set 15	Set 16
P_0	0.9	0.9	0.9	0.9	0.9
P_1	0.2	0.2	0.2	0.2	0.2
P_2	0.8	0.8	0.8	0.8	0.8
P_3	0	0	0	0	0
iterations	200	200	200	200	200
n_{max}	5	4	6	7	8

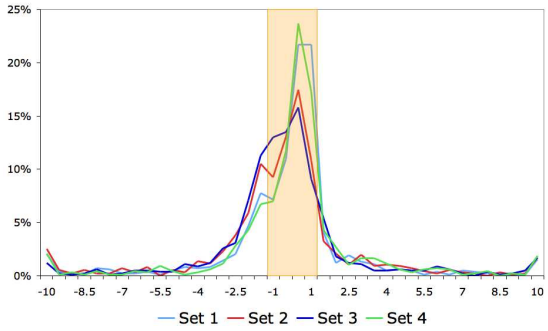

	Set 1	Set 2	Set 3	Set 4
worse	30.67%	38.84%	37.30%	33.57%
same	29.47%	21.39%	20.37%	24.04%
better	39.86%	39.77%	42.33%	42.39%

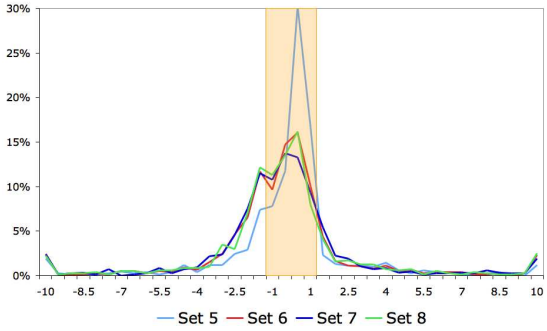

	Set 5	Set 6	Set 7	Set 8
worse	**26.12%**	37.87%	41.32%	38.81%
same	**24.06%**	21.69%	20.84%	20.15%
better	**49.82%**	40.44%	37.84%	41.04%

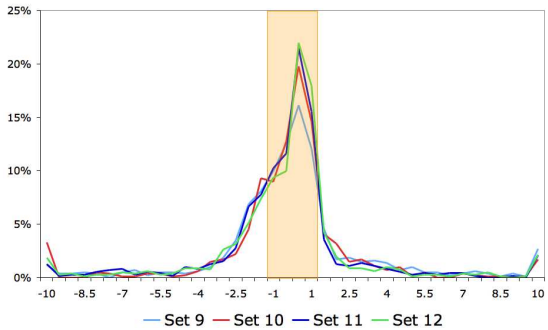

	Set 9	Set 10	**Set 11**	Set 12
worse	41.21%	34.60%	**33.38%**	33.33%
same	20.17%	23.93%	**23.27%**	25.34%
better	38.62%	41.47%	**43.35%**	41.32%

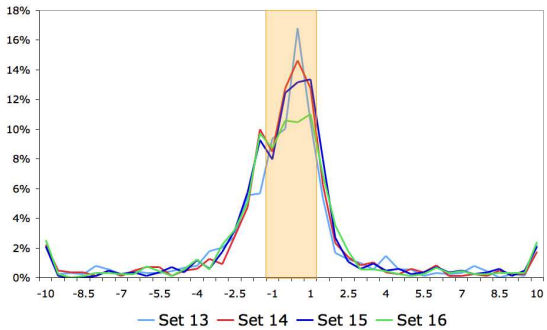

	Set 13	Set 14	Set 15	Set 16
worse	47.66%	41.35%	43.78%	49.45%
same	16.15%	22.76%	22.65%	20.75%
better	36.19%	35.89%	35.57%	29.80%

Figure IV.3.4: *Results of the three experiments on parameter tuning. Top row: first experiments. Bottom row, left: second experiment; right: third experiment. The graphs show on the y axis the proportion of nuclei having the ratio values on the x axis, as defined in Equation IV.3.8. The tables list the proportions of nuclei for which the set parameters induce a worse, similar or better segmentation than with the control parameters.*

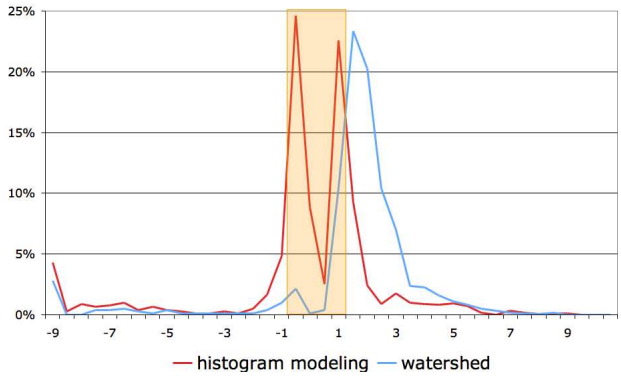

Figure IV.3.5: *Evaluation results of our nucleic segmentation and the watershed with the* Comets *measure. The graphs show on the y axis the proportion of references having a score value on the x axis.*

segmentation than the control is the highest, while the proportion of nuclei with a worse segmentation is almost the lowest (33.38% against 33.33% for Set 12). We keep Set 11 for the rest of the experiments. In the third round however, with all parameter values the proportion of nuclei with a worse segmentation is higher than that with a better segmentation. We conclude that none of the parameter values outperform the control chosen, and thus keep the control (Set 11) as the best set of values. These values are similar to the actual values chosen by visual evaluation of the results in Chapter III.

The *Comets* scores for Set 11 are shown in Figure IV.3.5, along with the scores of the watershed-based segmentation, presented in Chapter III, for comparison. The two peaks on the red curve show that most of the nuclei segmented with our method score either close to 1 or -1, while the single peak in values above 1 on the blue curve indicate that most nuclei tend to be over-segmented with the watershed.

The proportion of references with a score between -1 and 1 is 68.4% with Set 11 parameters, and 36.4% with the watershed. Using a range between -2 and 2, these proportions are respectively 77.1% and 68.4%. Although our method still outperforms the watershed, these values are significantly lower than those found by visual evaluation of the results, in Chapter III. A first explanation is that the subset of images chosen for this automatic evaluation are from only two individuals, and may not be representative enough of the diversity of images. Our future work includes marking more references from all individuals. A second explanation is that a visual inspection of segmentation results may be more lenient than a strict comparison with fixed references.

Even though these final proportions may be not representative enough, the methodology presented here allows a systematic tuning of parameters and a comparison of different segmentation methods, using a large number of objects.

Summary

We have presented our novel model, *Comets*, a single framework that allows:

- The encoding of segmentation references with local confidence factors, storing more expert knowledge than a single shape at a low cost;
- The combination of multiple references, with confidence-based local weights;
- A single discrepancy measure that allows an easy interpretation of segmentation results, in qualitative (correct, under-, over-segmented, missed, noise) and quantitative (severity) terms.

To the best of our knowledge, existing methods can perform only one of the above. These actions are based on local confidence factors, which are automatically computed from an expert user's input. The extra input needed, namely the limit pixels, is less demanding that landmark selection, and can easily be added to existing systems. All the information used in our model is provided by human experts. In particular no parameter is used, and no assumption is made to combine multiple shapes, unlike existing methods as [185]. This makes our model independent of segmentation methods, as defined in [91]. We have presented results of discrepancy measures, showing that the *Comets* error is more conclusive than some commonly used metrics.

This framework can be used to compare qualitatively and quantitatively different segmentation methods applied to the same set of images. In particular, it can be used to tune the parameters of a segmentation method. Since such comparisons may be ambiguous, we have presented two different ways to evaluate a segmentation method: from a reference and from a user viewpoint.

Discrepancy evaluation has been little used according to Zhang [201], who concludes by calling for "new ideas and procedures for the methodology and practical implementation of evaluation". We have presented here a novel method for discrepancy evaluation and detailed its implementation.

Chapter V

Discussion and Future Work

This chapter draws together the points made throughout this work. It discusses what contributions have been made, their strengths and possible improvements, and presents possible future projects connected to this work. Since our project has been application-driven, there are two complementary aspects to the discussion and contributions: from a computer vision point of view, and from a cytometry point of view. We start with computer vision, where we discuss our novel segmentation methods and our novel evaluation framework, and present some possible extensions of this framework and its uses. We then discuss the cytometric application of our work, within the SAFE Network of Excellence, and draw some conclusions from the pilot study we conducted. We also present some future projects aimed to improve the detection of fetal cells within maternal circulation.

V.1. Computer Vision

Our work has made contributions in two fields of computer vision: segmentation and evaluation.

Our nucleic segmentation method consists in modeling the image formation, in order to derive a model of image histogram. That model is then fitted to actual data by an adapted Expectation-Maximisation algorithm. When fitted, the model allows the selection of relevant threshold values, first global then local, which are used to segment the nuclei in the images. The image model that we developed is meant to evaluate the impact of object fluorescence in the surrounding background regions. The thresholds used to segment out the background are directly derived from the model we developed for this type of image formation. As a result, they have a strong theoretical justification, as opposed to other thresholding methods based non-realistic assumptions on histogram shapes. This approach to segmentation consists in gradually ruling out the background, until the objects of interest are correctly segmented. It differs from most existing segmentation methods, in which the objects are gradually ruled in (such as watershed or active contours). Our approach is more robust in our context, where the background is more predictable and easy to model than the objects. However, it is not able to isolate touching objects: this is why an extra step was needed in our segmentation method, based on an inner threshold which has no theoretical foundations. The issue of segmenting touching non-convex nuclei in 2D microscopy is generally acknowledged as challenging, not the least because even human experts cannot always perform it reliably. Our method is based on a simple observation: human experts can isolate touching nuclei when a dark path connects different sides of their borders. This can be seamlessly integrated to our segmentation method, as presented in Chapter III. However, it is difficult to evaluate this step alone, since no ground truth can be relied on. As a comment on our model, the particular profile chosen – a decreasing exponential – was not derived from a theoretic model. We believe that too many unknown factors contribute to the side illumination to

model it completely. In particular, the density and constitution of the materials surrounding the nuclei in the slide, and the volumetric geometry of the nuclei would need to play a significant role in such a model, while very little is know on them. Any other decreasing function may be tested, such as inverse quadratic, by simply 'plugging' it into the equations, to derive new illuminated background functions, and new formulas to compute their parameters from a weighted histogram. By this we mean that our segmentation method, while using a specific profile, is not dependent on it, and could be tested with other ones.

The Expectation-Maximisation (EM) algorithm is in fact, in its general form, a class of algorithms meant to fit a parametric model to incomplete data, through an iterative process. The particular algorithm we presented in Chapter III is adapted to histogram modeling. EM algorithms have two notorious weaknesses: first, their can be very sensitive to the initialisation chosen for the iterative process. Second, the more components are added to the model, the better the fit tend to be. In our case, the initialisation consists in choosing the proportions of each component over the histogram range of values. These values are somewhat constrained by the nature of the model: the non-illuminated background function will always model the darker pixels, the nuclei function will always model the brighter pixels, and the illuminated background function will model most of the pixels in-between. We have conducted a series of experiments where we vary the proportions, in keeping with these qualitative constraints, detailed in Chapter IV. The search for better parameters is still an open question: as there is no theoretical justification of the initial values in our context, we use these empirically found values. Regarding the second issue, our method actually does not suffer from it. Increasing the number of components (*i.e.* the value of n in our model) does not always improve the error, as illustrated by the last round of experiments in Chapter IV. This is because the components of our model are not independent, unlike in other models such as mixtures of Gaussians. In our model, each type a component is added, two new functions are included: one for the nuclei (an extra function N_i) and one for the illuminated background (an extra function IB_i). Each illuminated background function models a high number of pixels of low intensity: adding one such function, even with a low weight, has a significant impact on the model at the low intensities. As a result, having too many of these functions will significantly raise the distance between the model and the data. While the main issues of EM algorithms have no significant impact in our context, open questions remain on the choice of parameter values: the initial values of the model, the total number of iterations used, and the error measure chosen, have an impact on the final model chosen, but are only chosen through prior experiments.

Our probe segmentation method is meant to avoid segmenting foreground noise (*i.e.* unwashed and unattached fluorescent probes), which is the most severe issue in our context. Bearing in mind that nuclei overlapped by foreground noise occur much more frequently (by a few orders of magnitude) than fetal nuclei within maternal circulation, it is important to avoid classifying one for the other. By segmenting out foreground noise, our method ensures that it does not affect the measures of fluorescence in nuclei. A second important point is the number of probes visible within nuclei. As detailed in Chapter III, this number is a rough estimation of the imaging quality of a sample. Nuclei showing less than twenty probes are either affected by blur, foreground noise overlap, or low probe attachment rate. By segmenting probes of a given size, our method can directly evaluate the number of probes within each nuclei, while other methods cannot (such as top-hat transform). These two properties of our probe segmentation method are important when it comes to drawing conclusions from the pilot study conducted as a SAFE project.

Our two methods of segmentation have success rates of over 99% on our data set, containing nearly 14,000 nuclei. This is a significant improvement over existing methods, especially for nucleic segmentation, where typical success rates are about 80%. However, it is important to bear in mind that in most existing cytometric applications, a success rate of 80% is already more than enough. Some applications require the segmentation of a fixed number of nuclei, e.g. 200, or a proportion of nuclei below 80%. We think this is why existing segmentation methods have not been pushed towards better results, which often come at the cost of lower robustness to imaging conditions, and why simple segmentation methods such as low-level vision, watershed or active contours are still commonly used in cytometry, when they are now obsolete in other applications of computer vision. In our context however, higher rates where required, for both nuclei and probes, with no alteration to robustness or automation.

While success rates are intuitive to interpret, we wish to emphasis that evaluating segmentation methods is a challenging issue, especially on images showing multiple objects. It can be argued that segmentation is a form of classification, which leads to using the frameworks of classifiers evaluations, such as Receiver-Operating Characteristic (ROC) curves. Classification outcomes are usually classified in four categories, namely true and false positive and negative. However, when it comes to segmenting objects, it can be difficult to use such categories. Using them on a pixel basis leads to evaluation results that are challenging to interpret. On the other hand, using them on a full object basis leads to pessimistically biased results: even when a segmentation is correct, it very rarely matches a reference perfectly. Secondly, we consider that using four categories

of results does not always give enough insight into segmentation methods. Over-segmented and under-segmented objects would fall in the same category, as would minor and severe errors. In our context, these different types of errors are not equivalent, and the severity of mis-segmentation is important. For these reasons, in Chapter III we presented results using five categories, and in Chapter IV we introduced a method to measure the severity of errors at the same time.

The novel framework for discrepancy evaluation introduced in Chapter IV, called *Comets*, is meant to provide results with a direct and simple interpretation, even for objects affected by blur and ambiguity. It was designed so that the measure between a segmented object and a reference would reflect both the type of difference between them (over or under-segmentation), and its severity, with a single real number. By convention, a number between -1 and 1 is interpreted as a correct result, with 0 being a perfect match with the reference. A number below -1 reflects under-segmentation, and a number above 1, over-segmentation. In both cases, the higher absolute value of the number, the more severe the error. This is achieved by encoding the references as confidence maps, and not only binary masks or sharp boundaries as is often the case. A confidence map assigns each pixel in and around an object a number, which reflects the user's confidence that the pixel belongs to the background, the object, or the boundary. The higher the confidence assigned to a pixel, the more severe a mislabeling of this pixel is. Based on this observation, the error between a segmented object and a reference can simply be defined as the confidence of a mislabeled pixel with the maximum absolute value. As detailed in Chapter IV, such a confidence map can be defined manually by a user through simple clicks, and encoded as a text file in an efficient way. One of the strengths of this approach is that the confidence maps may look different in various parts of the object, depending on the local level of blur, or the presence of nearby objects. However, segmented objects often suffer from both under- and over-segmentation. Since the error measure we introduced consists of only one number, only the worst of these two errors is kept for the evaluation. When they are of similar severity, the final outcome may be somehow arbitrary; and when the parameters of a segmentation methods are slightly changed, an object may suddenly have an error with a different sign. This issue may be avoided by defining the error as a couple of real numbers: the lowest negative and the highest positive confidence of mislabeled pixels. It would still make the results intuitive to interpret, though possibly less easy to visualise and compare. Other possible extensions of the *Comets* framework include defining confidence maps for 3D data, and exploring its uses in non-medical data.

Along with the error measure developed, we clarified in Chapter IV the definition of success rates for images showing multiple objects. First, each object can

be measured against each reference. Then, from a reference point of view, the best scores achieved on each reference are kept, along with the number of objects not matching any reference. Conversely, from a user point of view, the best scores achieved by each object are kept, along with the number of missed references. Both approaches can be interpreted in their own right, to define rates of success, over-segmentation, etc. Using the reference point of view, this framework allows a systematic evaluation of a segmentation method on a potentially large set of data, quickly and automatically. We illustrated this in Chapter IV, and showed that it can be used to tune the parameters of a segmentation method, or to compare different methods. However, it requires the prior definition of references as confidence maps in the *Comets* framework.

V.2. Cytometry

As detailed in Chapter I, this work is part of the SAFE Network of Excellence, and our particular interest lies in the search for markers to discriminate fetal from maternal nuclei within maternal circulation. The particular marker tested in this work is the fluorescence of telomeric probes, as an indication of the telomeric length, known to be higher in fetal nuclei than in maternal ones. To assess this marker and its potential to discriminate, a pilot study was conducted, by some of the SAFE partners, involving a series of blind tests. For each test, a sample of fetal cells, along with one or two samples from adults, were processed separately but in the same way, resulting in a series of fluorescence microscopy images from each individual. These images were anonymised and processed by the software we developed, which implemented the segmentation methods and measures detailed in Chapter III. The goal of this pilot study was to evaluate whether the protocols and measures used (from the cell preparation to the imaging and the image processing) resulted in a clear separation of the fetal nuclei from the adult ones.

The results we obtained are presented and discussed in Chapter III. At this stage, the conclusions to be drawn from this pilot study belong to the SAFE Network of Excellence, and several partners are involved. They are far beyond the scope of this work, which is why we do not include them here. We only discuss some implications of our results.

The main observation from the results on the blind trials is that in each case, one individual stands out as having brighter probes. This tends to show that the method used can efficiently distinguish different un-mixed populations of nuclei based on their telomeric length. However useful as it may be, this is significantly different from an original goal of this work, which required to isolate a few nuclei within another population based on their telomeric length. The results obtained during the pilot test show that the overlap between the populations is still too large to distinguish between individuals of different populations with certainty.

Improving the segmentation results beyond 99.3% would not be enough to reduce the overlap, but other improvements are likely to have an effect on it.

The results presented in Chapter III also show that in two blind trials, the number of probes visible per nuclei are below the expected values. This suggests that either the probe attachment rate during the biological processing of the sample, or the imaging quality of the microscopic hardware used were not optimal. It appears that in the two cases, images were affected by visual and motion blur. This implies that the imaging quality could be improved, and at present the measures performed on the two blind trials concerned are not as conclusive as they could be.

At this stage, we are only in a position to call for improved imaging quality in the future pilot studies. Although the first results obtained show that telomeric probe fluorescence can be used to distinguish populations of nuclei but not individual nuclei yet, more tests with higher imaging quality are needed before definite conclusions on this marker can be drawn.

In the next section we present future projects, the first of which could also be used to increase the conclusiveness of the measures.

V.3. Future Work

V.3.1 Usability of nuclei

This future project aims to improve the quality of the measures used to compare the telomeric intensities from different individuals, as detailed in Chapter III. Not all uncultured nuclei will be usable in the final stage, where their genetic contents is to be investigated. Some are damaged during the early processing of the blood sample, and could be rejected before measuring the probe intensities. Unusable nuclei can be detected by expert cytometrists based on their visual aspect. The task would be to develop an expert system to identify unusable nuclei after segmentation, and reject them prior to measuring probe intensities. In addition, clusters and nucleic debris are to be identified as such and rejected before measuring probe intensities.

In the early stages of this project, 50 isolated nuclei were labeled by experts as usable or unusable. Classifiers could be developed on this training set. Our early work investigates features based on the nuclei shapes first, focusing on the nuclei concavities, easily identified by subtraction from the convex hull, and the regularity of the border, based on Fourier decompositions. Figure V.3.1 shows early results on a test image. Future work is needed to investigate more features and implement classifiers.

V.3.2 *Comets* for parameter tuning

The *Comets* framework presented in Chapter IV is mainly intended to provide a richer way to encode references, and a single discrepancy measure to evaluate segmentation results. As illustrated in Section IV.3, the measure can be used to tune the parameters of a segmentation method. This approach can be automated: the user specifies the range of parameter values to investigate, then the segmentation, evaluation and comparison of outcomes is automatic. In this framework,

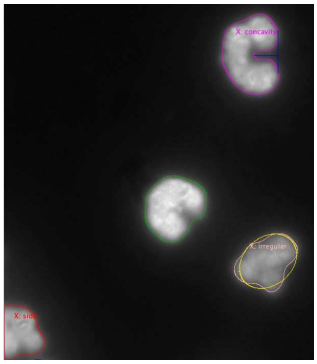

Figure V.3.1: *Illustration of the usabilities found by our method.*

the effect of any parameter on the segmentation of every nucleus individually can be measured. However, this approach amounts to a brute-force search within a parameter space.

A future project might investigate whether the *Comets* measures can be used to drive the search in the parameter space. Figure V.3.2 shows the measures performed on the same nuclei, with two different sets of parameter values used for the active contour method described in [35]. The points in the top left-hand side corner show that most of the nuclei under-segmented with the first set are over-segmented with the second set. The change of parameter values made in the second set might be too large, and could be reduced to improve the results.

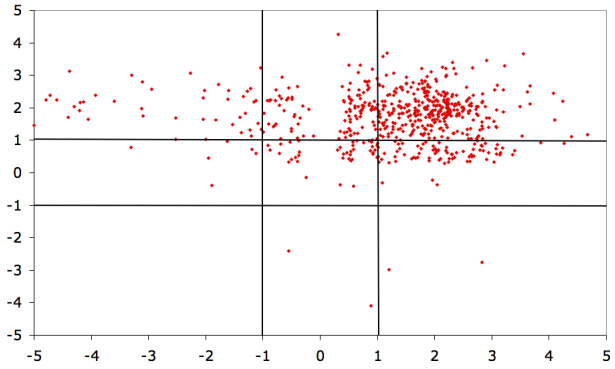

Figure V.3.2: *Individual comparisons of* Comets *results, to tune the parameters of active contours. Each point corresponds to one nucleus: the X value is the* Comets *measure with one set of parameter values, and the Y value, that with a second set of values.*

V.3.3 Distinguishing fetal and maternal nucleated erythroblasts

Another possible application is to differentiate maternal and fetal cells based on their appearance on FISH images, but not on the telomeric contents. This

project would focus on nucleated erythroblasts, or red-blood cells. Erythroblasts are mostly free of nuclei, except fetal erythroblasts in maternal blood, and a few maternal ones. They can be distinguished visually by expert cytologists. The project would develop an expert system to reproduce this distinction.

An early training set contains 230 examples of nucleated erythroblasts, manually marked as fetal or maternal, as illustrated on the left of Figure V.3.3. Our segmentation method can be used to segment the nuclei, in blue, as illustrated on the right of Figure V.3.3. However it cannot be used directly for the segmentation of the cytoplasm, in green. When cells are close and overlap, the green intensity at the border can be higher than within the cells. Our method to separate touching objects requires a darker region between them, and will fail on some images. It would be necessary to adapt it to the visual properties of red blood cells, then develop a classifier to distinguish between maternal and fetal nucleated erythroblasts.

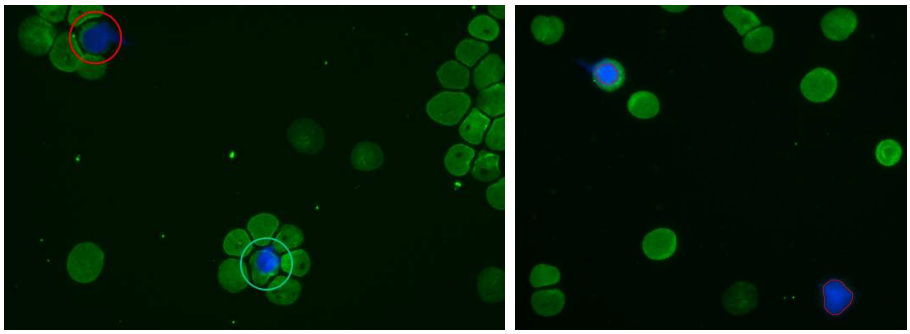

Figure V.3.3: *Nucleated erythroblasts. Left: fetal one, marked in red, and maternal one, marked in blue. Right: results of our nucleic segmentation method.*

V.4. Conclusion

In this dissertation we have presented our contributions to the automation of cell image analysis, in particular the segmentation of fluorescent nuclei and probes, and the evaluation of segmentation results. We have developed two novel segmentation methods, adapted for nuclei and probes in Fluorescence *in-situ* Hybridisation images. We have demonstrated that they are both robust, automated, and achieve 99.3% accuracy on our database of over two thousand images. We have compared them with state-of-the-art techniques used in cytometry, which we reviewed in detail, and discussed their strengths. We have used them to show that telomeric probe intensities are a promising approach to distinguish between maternal and fetal uncultured leucocytes, and shown that imaging quality is a key factor to improve the distinction.

We have also presented *Comets*, a novel framework for discrepancy evaluation of segmentation methods, in the context of medical imaging. This framework allows the encoding of expert segmentation references with local confidence factors, can be used to combine multiple references of objects, and provides a single measure that can be easily interpreted quantitatively and qualitatively. We have shown that this measure can be used to tune a segmentation method's parameters on a large volume of data.

In the Appendices we have detailed the implementation of our methods on a distributed computing environment. We have presented the XML database structures adapted to the storage of references and different results, and the architecture and protocols used to achieve a reliable, scalable and robust processing of large number of images, and the main graphical user interfaces. We have presented quantitative results showing the performance of our program on this distributed environment.

We hope that our work will contribute to the success of the European Commission-funded Network of Excellence SAFE, and through it to the progress of cytometry and prenatal genetic disease detection.

Related publications

The following papers, published or under review, are related to the contents of this dissertation.

- Christophe Restif and William F. Clocksin. Comparison of segmentation methods for cytometric assay. In *Medical Image Understanding and Analysis*, pages 153-156, London, UK, September 2004.

- Christophe Restif. Towards Safer, Faster Prenatal Genetic Tests: Novel Unsupervised, Automatic and Robust Methods of Segmentation of Nuclei and Probes. In *European Conference on Computer Vision*, pages 437-450, Graz, Austria, May 2006.

- Anthony J. McCollum, Christophe Restif and William F. Clocksin. Imaging system design for detecting small changes in telomere length. In *Medical Image Understanding and Analysis*, pages 206-210, Manchester, UK, July 2006.

- Christophe Restif, William F. Clocksin. Computer Vision for Segmentation in Cytometry. Submitted to *ACM Computing Surveys* in December 2005.

Appendices

A. Algorithms

A.1 Low-level vision algorithms

Grayscale reconstruction

This operation is based on conditional dilation. Let m be a mask, *i.e.* an image with the same dimensions as f but a different content. The condition dilation of f by kernel k under the mask m is:

$$f \oplus_m k = (f \oplus k) \wedge m \tag{A.1}$$

where $\wedge$ is the pixel-wise minimum operator, defined as:

$$(f_1 \wedge f_2)(x, y) = \min(f_1(x, y), f_2(x, y)) \tag{A.2}$$

Conditional dilations are iterated as:

$$(f \oplus_m k)^{n+1} = (f \oplus_m k)^n \oplus_m k \ , \ n \geq 1 \tag{A.3}$$

Since this sequence is increasing and has discrete and bounded (grayscale) values, conditional dilations converge after a finite number of iterations. The resulting image is the grayscale reconstruction of image f under mask m with kernel k, and is noted:

$$f \perp_k m = (f \oplus_m k)^\infty \tag{A.4}$$

To extract domes of high h (in gray values), the image to reconstruct is f_{-h}, defined as $f_{-h}(x, y) = \max(0, f(x, y) - h)$. In the reconstruction of f_{-h} under the mask f, the domes are actually cut off. Thus, the domes of high h are the connected components of the image g_{dome} defined as:

$$g_{dome} = f - (f_{-h} \perp_{k_{dome}} f) \ , \ k_{dome} = \begin{pmatrix} 0 & 0 & 0 \\ 0 & 0 & 0 \\ 0 & 0 & 0 \end{pmatrix} \tag{A.5}$$

Gradient Vector Flow

The GVF is defined as the field $g(x,y) = (g_x(x,y), g_y(x,y))$ which minimises the energy functional:

$$\varepsilon = \sum_{x,y} \mu \left|\nabla g\right|^2(x,y) + \left\|\nabla f(x,y)\right\|^2 \cdot \left\|g(x,y) - \nabla f(x,y)\right\|^2 \tag{A.6}$$

$$\text{where } \left|\nabla g\right|^2 = \left(\frac{\partial g_x}{\partial x}\right)^2 + \left(\frac{\partial g_x}{\partial y}\right)^2 + \left(\frac{\partial g_y}{\partial x}\right)^2 + \left(\frac{\partial g_y}{\partial y}\right)^2 \tag{A.7}$$

and μ is a constant, weighting the relative importance of smoothing g: the noisier the image f, the higher μ should be [194]. The functional ε can be minimised by an iterative process, using finite differences in space (steps δx and δy) and time (step δt). Using the following notations from [195]:

$$\begin{aligned} \partial_x f(x,y) &= f(x+1,y) - f(x,y) \qquad &, c_x(x,y) &= b(x,y) \cdot \partial_x f(x,y) \\ \partial_y f(x,y) &= f(x,y+1) - f(x,y) \qquad &, c_y(x,y) &= b(x,y) \cdot \partial_y f(x,y) \\ b(x,y) &= (\partial_x f(x,y))^2 + (\partial_y f(x,y))^2 \,, \qquad & r &= \mu \cdot \delta t / (\delta x \cdot \delta y) \end{aligned} \tag{A.8}$$

where $r \leq 4$ to avoid oscillations, g_x and g_y are evaluated iteratively until convergence, with the formulas:

$$\begin{cases} g_x^0(x,y) &= \partial_x f(x,y) \\ g_x^{t+1}(x,y) &= (1 - b(x,y)\delta t)\, g_x^t(x,y) + r\nabla^2 g_x^t(x,y) + c_x(x,y)\delta t \end{cases} \tag{A.9}$$

where $\nabla^2 g_x^t(x,y)$ is the non-directional Laplacian of g_x^t, defined above. g_y is computed with similar formulas, replacing the underscripts x with y. In [193], Xu *et al.* suggest a more general energy functional defining GVF:

$$\varepsilon = \sum_{image} \phi\left(\left\|\nabla f\right\|\right) \left|\nabla g\right|^2 + \psi\left(\left\|\nabla f\right\|\right) \left\|g - \nabla f\right\|^2 \tag{A.10}$$

and apply it with $\phi(r) = 1 - e^{-\left(\frac{r}{\kappa}\right)^2}$, $\psi(r) = e^{-\left(\frac{r}{\kappa}\right)^2}$, for a constant κ. The previous definition of the GVF corresponds to the special case $\phi(r) = \mu$ and $\psi(r) = r^2$.

Chamfer distance transform

Supposing the foreground pixels are 1 and the background 0, the Chamfer algorithm offers a quick way to compute the distance transform g of f by performing only three scans of images, but requires one temporary image h. Initially, g and h are two copies of f. First, g is filtered in the left-to-right top-down direction with the filter $k_{forward}$ and the formula

$$g(x,y) = \min_{k_{forward}(i,j)>0} \left(k_{forward}(i,j) + g(x+i, y+j)\right) \tag{A.11}$$

Then, h is filtered right-to-left bottom-up with the filter $k_{backward}$ and the formula

$$h(x,y) = \min_{k_{backward}(i,j)>0} (k_{backward}(i,j) + h(x+i, y+j)) \tag{A.12}$$

In the final scan of g, $g(x,y)$ is assigned the value $min(g(x,y), h(x,y))$. These three operations are only applied to the foreground pixels. Typical filters are:

$$k_{forward} = \begin{pmatrix} 4 & 3 & 4 \\ 3 & 0 & 0 \\ 0 & 0 & 0 \end{pmatrix} \ , \ k_{backward} = \begin{pmatrix} 0 & 0 & 0 \\ 0 & 0 & 3 \\ 4 & 3 & 4 \end{pmatrix} \tag{A.13}$$

To increase the precision of the distance computation, bigger filters can be used [187], such as:

$$\begin{pmatrix} 0 & 11 & 0 & 11 & 0 \\ 11 & 7 & 5 & 7 & 11 \\ 0 & 5 & 0 & 0 & 0 \\ 0 & 0 & 0 & 0 & 0 \\ 0 & 0 & 0 & 0 & 0 \end{pmatrix} , \begin{pmatrix} 0 & 0 & 0 & 0 & 0 \\ 0 & 0 & 0 & 0 & 0 \\ 0 & 0 & 0 & 5 & 0 \\ 11 & 7 & 5 & 7 & 11 \\ 0 & 11 & 0 & 11 & 0 \end{pmatrix} \tag{A.14}$$

Squared Euclidian distance transform

We present here the fast algorithm detailed by Felzenszwalb and Huttenlocher [51], to compute the square of the l_∞ distance exactly. We use the following notations. Let f be the original image with dimensions max(*column*) and max(*row*), and g its distance transform: $g(x,y)$ is accessed as either $g_{row\ y}(x)$ or $g_{column\ x}(y)$. The distance transform can be seen as the lower envelope of a set of parabolas: let v be an array containing the centres of the parabolas, and z an array containing the intersections of the parabolas. Let n be the maximum of max(*column*) and max(*row*) of f: v should be of size n and z of size $n+1$. During the algorithm, g is scanned only twice, and at the end, it contains the square of the Euclidian distance transform of f.

Thresholding techniques

Otsu's method consists in maximising the scatter between the background and foreground pixels. Let N be the total number of pixels, G the total number of gray levels, and p the probability mass function of the image f: $p(i)$ is the number of pixels of intensity i divided by N. With the following notations:

$$P_b(T) = \sum_{i=0}^{T-1} p(i) \ , \ P_f(T) = \sum_{i=T}^{G} p(i) \ , \ m_b(T) = \sum_{i=0}^{T-1} ip(i) \ , \ m_f(T) = \sum_{i=T}^{G} ip(i) \tag{A.15}$$

Algorithm 3 Squared Euclidian Distance Transform

1: **for** $i = 0$ to $\max(column)$ **do**
2: **for** $j = 0$ to $\max(row)$ **do**
3: $g_{column\,i}(j) \leftarrow f(i,j)$ /* *same as:* $g_{row\,j}(i) \leftarrow f(i,j)$ */
4: **end for**
5: **end for**
6: **for** $coord = column$, row **do**
7: **for** $i = 0$ to $\max(coord)$ **do**
8: $k \leftarrow 0$
9: $v[0] \leftarrow 0$
10: $z[0] \leftarrow -\infty$
11: $z[1] \leftarrow +\infty$
/* *Compute the lower envelope of parabolas* */
12: **for** $q = 1$ to $n - 1$ **do**
13: $s \leftarrow ((g_{coord\,i}(q) + q^2) - (g_{coord\,i}(v[k]) + v[k]^2))\,/(2q - 2v[k])$
14: **while** $s \leq z[k]$ **do**
15: $k \leftarrow k - 1$
16: $s \leftarrow ((g_{coord\,i}(q) + q^2) - (g_{coord\,i}(v[k]) + v[k]^2))\,/(2q - 2v[k])$
17: **end while**
18: $k \leftarrow k + 1$
19: $v[k] \leftarrow q$
20: $z[k] \leftarrow s$
21: $z[k+1] \leftarrow +\infty$
22: **end for**
/* *Fill in the values of the distance transform* */
23: $k \leftarrow 0$
24: **for** $q = 0$ to $n - 1$ **do**
25: **while** $z[k+1] < q$ **do**
26: $k \leftarrow k + 1$
27: **end while**
28: $g_{coord\,i}(q) \leftarrow (q - v[k])^2 + g_{coord\,i}(v[k])$
29: **end for**
30: **end for**
31: **end for**

Otsu's threshold is defined as:

$$T_{Otsu} = \arg \max_{0 \leq T \leq G} \frac{P_b(T) \cdot P_f(T) \cdot [m_b(T) - m_f(T)]^2}{P_b(T) \cdot \sigma_b^2(T) + P_f(T) \cdot \sigma_f^2(T)} \tag{A.16}$$

where $\sigma_b^2(T)$ and $\sigma_f^2(T)$ are the variances of the background and foreground pixels.

The isodata threshold T_{iso} is the value T for which the mean values of the background pixels $\mu_b(T)$ and foreground pixels $\mu_f(T)$ are equidistant to T. It can easily be computed iteratively:

$$T_0 = \frac{G}{2}\ ,\ T_{n+1} = \frac{\mu_b(T_n) + \mu_f(T_n)}{2} \text{ for } n \geq 0 \tag{A.17}$$

stopping when the difference between T_n and T_{n+1} is small enough (e.g. less than 1).

A.2 Watershed algorithm

We present here a popular algorithm to compute the watershed, published by Vincent and Soille [180], and analysed by Roerdink and Meijster [144]. We adapted it to use arbitrary markers as starting points for the immersion. In keeping with our previous notations, let f be the original image and g the watershed transform of f. Let *dist* be a helper image of the same size as f. Each pixel p has an original value $f(p)$, ranging from h_{min} to h_{max}, a label $g(p)$, and a distance $dist(p)$ – initially 0. The possible label values $g(p)$ are integers, with the following conventions:

MASK $= -2$ is a temporary value
INIT $= -1$ is the initial value of all pixels in g
WSH $= 0$ is the label of pixels in watershed lines
$1, 2, 3, ...$ are the labels of the catchment basins

Let *Marker* be the set of the pixel marked as starting points for the flooding process. Let *fifo* be a queue of pixels (a *first-in-first-out* data structure storing pixels) with the following operations:

fifo_add(p): adds pixel p at the tail of *fifo*
fifo_first(): removes and returns the pixel at the head of *fifo*
fifo_empty(): returns *true* if *fifo* is empty and *false* otherwise

A fictitious pixel FICT will be used in the queue, to decide when to stop iterations. Let $N(p)$ be a function returning the set of pixels that are neighbours of p. Finally,

as all pixels p need to be accessed by increasing values of $f(p)$, it is useful to have an array indexed by h from h_{min} to h_{max} referring to all the pixels of value h – called iso-level h. The watershed by immersion algorithm is described as Algorithm 4.

At the end of the flooding, all the pixels in g are labeled, from 0 on the watershed lines, to n, the number of catchment basins. The original algorithm starts a new catchment basin at each local minima. This is implemented by replacing line 3 in Algorithm 7 "**if** $p \in$ *Marker* **then**" with "**if** $g(p) =$ MASK **then**". To stop the flooding at level h_{stop}, line 3 in Algorithm 4 has to be changed into "**for** $h = h_{min}$ to h_{stop} **do**". The pixels between $h_{stop}+1$ and h_{max} should be labeled as background.

Algorithm 4 Watershed by Immersion: Outline

```
1: fifo_add(FICT)
2: current_label ← 0
3: for h = h_min to h_max do
4:    prepare iso-level h for processing (see Algorithm 5 page 131)
5:    extend the catchment basins (see Algorithm 6 page 132)
6:    process new markers (see Algorithm 7 page 133)
7: end for
```

Algorithm 5 Watershed by Immersion: Preparing Iso-Level h for Processing

```
1: for all p such that f(p) = h do
2:    g(p) ← MASK
3:    for all q ∈ N(p) do
4:       if g(q) ≥ 0 then
5:          dist(p) ← 1
6:          fifo_add(p)
7:          break for
8:       end if
9:    end for
10: end for
```

A.3 Geometric active contours

Fourier contours

The Fourier basis $(1, \cos(k2\pi s), \sin(k2\pi s))_{k\geq 1}$ is orthogonal for the standard dot product of continuous functions over $[0,1)$: $< f, g >= \int_0^1 f(s)g(s)ds$. These

Algorithm 6 Watershed by Immersion: Extending the Catchment Basins

```
1: current_distance ← 1
2: fifo_add(FICT)
3: loop
4:    p ← fifo_first()
5:    if p = FICT then
6:       if fifo_empty() then
7:          break loop
8:       else
9:          fifo_add(FICT)
10:         current_distance ← current_distance + 1
11:         p ← fifo_first()
12:      end if
13:   end if
      /* Inspect the neighbours of p to find its label */
14:   for all q ∈ N(p) do
15:      if dist(q) < current_distance and g(q) ≥ 0 then
16:         if g(q) > 0 then
17:            if g(p) = MASK or g(p) = WSH then
18:               g(p) ← g(q)
19:            else if g(p) ≠ g(q) then
20:               g(p) ← WSH
21:            end if
22:         else if g(p) = MASK then
23:            g(p) ← WSH
24:         end if
25:      else if g(q) = MASK and dist(q) = 0 then
26:         dist(q) ← current_distance + 1
27:         fifo_add(q)
28:      end if
29:   end for
30: end loop
```

Algorithm 7 Watershed by Immersion: Processing New Markers

```
1: for all p such that f(p) = h do
2:    dist(p) ← 0
3:    if p ∈ Marker then
4:       current_label ← current_label + 1
5:       fifo_add(p)
6:       g(p) = current_label
7:       while not fifo_empty() do
8:          q ← fifo_first()
9:          for all r ∈ N(q) do
10:            if g(r) = MASK then
11:               fifo_add(r)
12:            end if
13:         end for
14:      end while
15:   end if
16: end for
```

functions can be linearly combined to define a function that will interpolate the N points $v(s_i) = (x(s_i), y(s_i))$, where $s_i \in [0, 1), 0 \leq i < N$. These points would have been the vertices of a parametric active contour. However, as v is defined on a discrete sampling $\{s_i, 0 \leq i < N\} \subset [0, 1)$, the corresponding dot product that will be used to interpolate v is $< f(s), g(s) >= \frac{1}{N} \sum_{i=0}^{N-1} f(s_i)g(s_i)$. To ensure a proper interpolation, one should first verify that the Fourier basis is still orthogonal for that dot product. Ideally,

$$\frac{1}{N} \sum_{i=0}^{N-1} \cos(k_1 2\pi s_i) \cdot \cos(k_2 2\pi s_i) = \begin{cases} 1 \text{ if } k_1 = k_2 = 0 \\ \frac{1}{2} \text{ if } k_1 = k_2 \geq 1 \\ 0 \text{ otherwise} \end{cases} \tag{A.18}$$

the same with the sin functions, and $\frac{1}{N} \sum_{i=0}^{N-1} \cos(k_1 2\pi s_i) \cdot \sin(k_2 2\pi s_i) = 0 \; \forall \, k_1, k_2$. In case the actual values are too different from those, more samples should be taken – or the corresponding Fourier functions should not be used for the reconstruction.
Once this verification has been done, the Fourier coefficients of $v(s_i) = (x(s_i), y(s_i))$ are defined as [164, 168]:

$$\begin{aligned} &a_0 =< x(s), 1 > , a_k = 2 < x(s), \cos(k2\pi s) > , b_k = 2 < x(s), \sin(k2\pi s) > \\ &c_0 =< y(s), 1 > , c_k = 2 < y(s), \cos(k2\pi s) > , d_k = 2 < y(s), \sin(k2\pi s) > \end{aligned} \tag{A.19}$$

where $< f(s), g(s) >= \frac{1}{N}\sum_{i=0}^{N-1} f(s_i)g(s_i)$. With the coefficients $(a_0, c_0, a_k, b_k, c_k, d_k)_{k\geq 1}$, the function $v(s)$ is interpolated over $[0, 1)$ as:

$$\begin{pmatrix} x(s) \\ y(s) \end{pmatrix} = \begin{pmatrix} a_0 \\ c_0 \end{pmatrix} + \sum_{k\geq 1} \begin{pmatrix} a_k & b_k \\ c_k & d_k \end{pmatrix} \cdot \begin{pmatrix} \cos(ks) \\ \sin(ks) \end{pmatrix} \tag{A.20}$$

Ignoring the coefficients after a given k_{max} will remove the high frequencies in the reconstruction of $v(s)$, which is usually an advantage in cytometry: objects tend to have smooth boundaries. The remaining coefficients are stored in a vector p. A geometric active contour corresponds to a unique p, and vice versa.

Derivations The vector tangent to the curve in point $v(s)$ is $\frac{dv}{ds}(s)$. Supposing the curve is oriented anti-clockwise, the external normal $n_{ext}(s)$ to the curve in point $v(s)$ is the unit vector colinear to:

$$\left(\frac{dv}{ds}\right)^{\perp}(s) = \begin{pmatrix} 0 & 1 \\ -1 & 0 \end{pmatrix} \cdot \left(\frac{dv}{ds}(s)\right) \tag{A.21}$$

Using the Fourier coefficients:

$$\left(\frac{dv}{ds}\right)^{\perp}(s) = \sum_{k=1}^{k_{max}} \begin{pmatrix} c_k & d_k \\ -a_k & -b_k \end{pmatrix} \cdot \begin{pmatrix} -k\sin(ks) \\ k\cos(ks) \end{pmatrix} \tag{A.22}$$

B-spline contours

Another way to interpolate sample points with a continuous function is to use B-splines, where B stands for *basis*. Cubic B-splines are piece-wise cubic polynomial functions with C^2 continuity and compact support[1]. They are also called B-splines of order 3.

We use the same sampling as above $(s_0, \cdots s_{N-1})$, and for convenience, we consider the samples to be cyclic, with $s_{i+N} = s_i$. B-splines are defined recursively over their order [34]:

$$\begin{aligned} B_i^0(s) &= \begin{cases} 1 \text{ if } s_i \leq s < s_{i+1} \\ 0 \text{ otherwise} \end{cases} \\ B_i^k(s) &= \left(\frac{s-s_i}{s_{i+k}-s_i}\right) B_i^{k-1}(s) + \left(\frac{s_{i+k+1}-s}{s_{i+k+1}-s_{i+1}}\right) B_{i+1}^{k-1}(s) \end{aligned} \tag{A.23}$$

where $0 \leq i < 1$ and $s \in [0, 1)$. Cubic B-splines are the family $(B_i^3(s))_{0\leq i<N}$; each function $B_i^3(s)$ is zero out of $[s_i, s_{i+4}]$. The samples $v(s_i) = (x_i, y_i)$ can be interpolated with the following combinations of splines:

$$x(s) = \sum_{l=0}^{N-1} B_l^3(s)Q_{xl}\ ,\ y(s) = \sum_{l=0}^{N-1} B_l^3(s)Q_{yl} \tag{A.24}$$

[1]The support of a function is the set of points where the function has non-zero values.

The points $Q_l = (Q_{xl}, Q_{yl})$ are called *control points*. Given that each cubic B-spline is non-zero only within four sample points, the interpolation of v can be simplified: for $s_i \leq s < s_{i+1}$, $v(s) = \sum_{l=i-3}^{i} B_l^3(s) Q_l^3$. The control points $Q_i = Q_i^3$ can be computed recursively: for $s_i \leq s < s_{i+1}$,

$$Q_i^0 = v(s_i)\ ,\ Q_i^{k-1} = \left(\frac{s-s_i}{s_{i+k}-s_i}\right) Q_i^k + \left(\frac{s_{i+k}-s}{s_{i+k}-s_i}\right) Q_{i-1}^k \tag{A.25}$$

Each value depends on s, and has to be computed recursively. Using irregular sampling requires the computation of all the cubic B-splines and all the control points for all s. With regular sampling however, not only the cubic B-splines can be computed directly, but also there are quick ways to compute the control points [142]. To do so, intermediate points $\tilde{Q}_i$ are computed as:

$$\begin{cases} \tilde{Q}_0 = \frac{1}{1-z_1^N} \sum_{l=0}^{N-1} z_1^l v(s_{N-l}) \\ \tilde{Q}_i = z_1 \tilde{Q}_{i-1} + v(s_i) \end{cases} \tag{A.26}$$

where $z_1 = \sqrt{3} - 2$, and are then used to compute the actual control points Q_i:

$$\begin{cases} Q_N = -\frac{6z_1}{1-z_1^N} \sum_{l=0}^{N-1} z_1^l \tilde{Q}_l \\ Q_i = z_1 Q_{i+1} - 6 z_1 \tilde{Q}_i \end{cases} \tag{A.27}$$

These points only depend on the samples now. Let β^3 be the symmetric cubic B-spline defined as:

$$\beta^3(t) = \begin{cases} \frac{2}{3} - |t|^2 + \frac{|t|^3}{2} & \text{if } 0 \leq |t| < 1 \\ \frac{(2-|t|)^3}{6} & \text{if } 1 \leq |t| < 2 \\ 0 & \text{otherwise} \end{cases} \tag{A.28}$$

Let h be the step between two samples: $h = s_{i+1} - s_i$. The family of B-spline $B_i^3(s)$ defined over the samples can be defined as: $B_i^3(s) = \beta(\frac{s-s_i}{h})$. This definition is not exactly equivalent to the recursive one above: with the recursive definition, the support of B_i^3 is (s_i, s_{i+4}), whereas now its support is (s_{i-2}, s_{i+2}). This simply corresponds to a shift of the indices k, so the formula to interpolate v is now, for $s_i \leq s < s_{i+1}$: $v(s) = \sum_{l=i-3}^{i} B_l^3(s) Q_{l+2}^3$.

Derivations Using B-splines with non-uniform sampling and the recursive definitions [34], the derivative is defined, for $s_i \leq s < s_{i+1}$,

$$\begin{aligned} \frac{dv}{ds}(s) &= \sum_{l=i-3}^{i} \frac{dB_l^3}{ds}(s) Q_l^3 \\ \frac{dB_l^k}{ds}(s) &= \frac{s}{s_{i+k} - s_i} B_i^{k-1}(s) - \frac{s}{s_{i+k+1} - s_{i+1}} B_{i+1}^{k-1}(s) \end{aligned} \tag{A.29}$$

If the splines as defined over a uniform sampling using the function $\beta_3(s)$, the derivative is:

$$\frac{dv}{ds}(s) = \sum_{l=i-3}^{i} \frac{dB_l^3}{ds}(s) Q_{l+2}^3 \ , \ \frac{dB_l^k}{ds}(s) = \frac{1}{h}\frac{d\beta^3}{ds}(\frac{s-s_i}{h}) \tag{A.30}$$

The curvature of $v(s)$ is defined as: $\kappa(s) = \left\| \frac{d^2v}{ds^2}(s) \right\|$ which can be computed by further derivation of the formulas above.

B. Databases for segmentation and evaluation

To process the whole set of images and store the results for later use, several databases are needed. Following the processing chain, the data to store consists of: the original images, the manual references defined on them, the measures performed after segmentation, and the evaluation results of these methods. The nature of data falls into two categories: images, stored as TIFF, JPEG and PGM files, and text results, stored as XML files. Before detailing how each type of data is stored, we briefly present the XML format.

XML, for Extensible Markup Language [189], is a tag-based, license-free, platform-independent text format with a wide range of uses. We use it to define data bases. Its extensibility allows the creation of tree-like structures with customised tags, labels, and attributes.

XML files are text-based and verbose. While they require more storage space than binary databases, they are easily readable by a user, and can be efficiently compressed for storage or network transit. With their tag-based syntax, they can easily be produced by any programming language. Parsing them can be done efficiently with simple character-based input file readers. We used the built-in XML parsers provided with Java Standard Edition [165].

```
<?xml version="1.0" encoding="utf-8"?>          ← standard first line
<!DOCTYPE root SYSTEM "/path/root.dtd">         ← file defining the structure of root
<root attr1="value1" attr2="value2">            ← opening tag, with attributes
  <leaf id="id1" attr="value">                  ⎫
    body with raw text data                     ⎬ first sub-element, with unique
  </leaf>                                       ⎭ ID and unstructured body
  <leaf id="id2" attr="other value">            ⎫
    raw text data                               ⎬ second sub-element
  </leaf>                                       ⎭
</root>                                         ← closing tag
```

Figure B.1: *Basic structure of an XML file.*

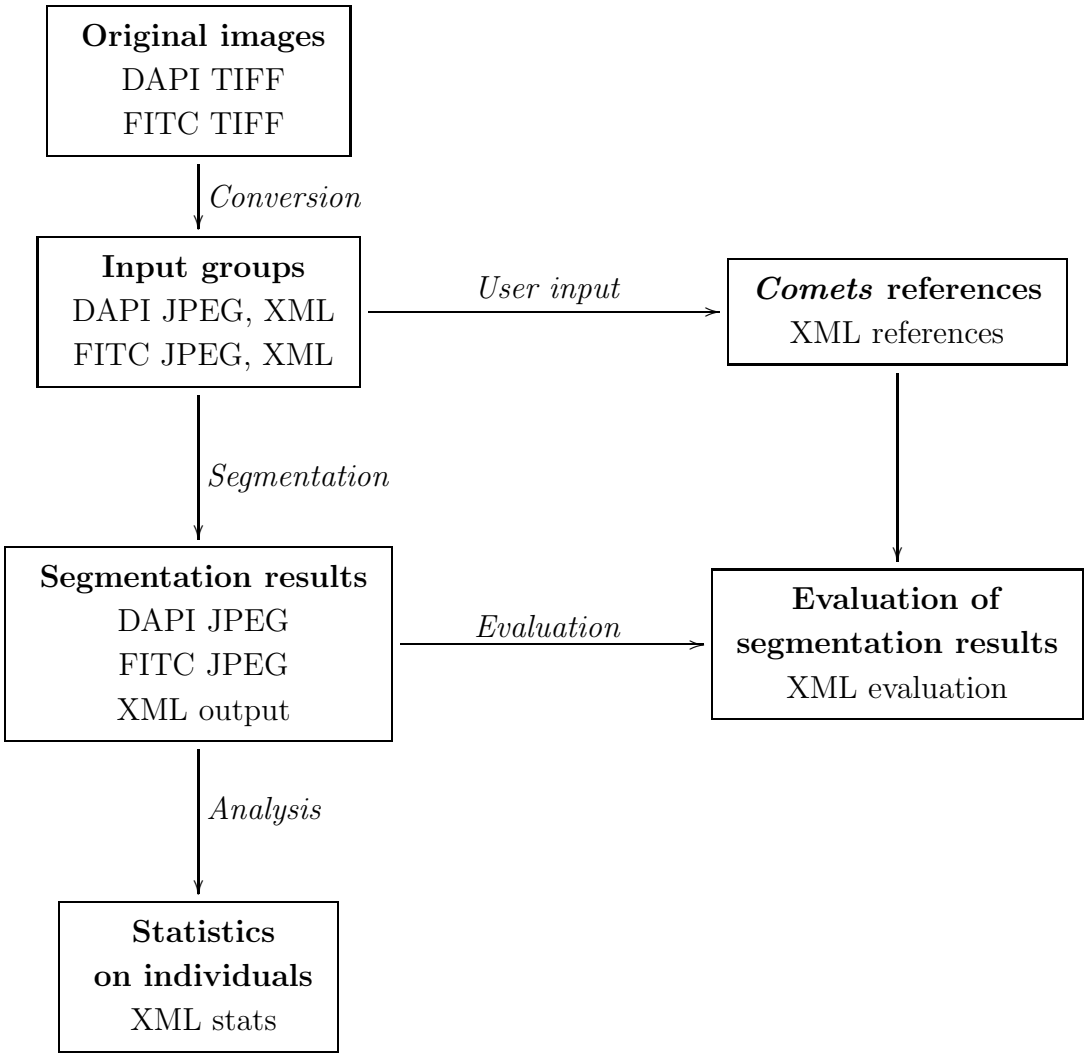

Figure B.2: *Databases and process flows: the databases used during the processing are shown as boxes, and the processes between them as arrows.*

Figure B.2 shows a summary of the databases used in our system, and the processes between them.

B.1 Original images and input groups

The original images are grayscale TIFF files, with intensity values encoded with 12 bits per pixel. They are arranged in pairs DAPI-FITC, and form the first image database, organised by individuals and sets (see Section III.3 for details).

For display, the original images converted into 8 bit JPEG files. These files are only used for visual inspection by users, and the loss of data due to the image dimming is visually small. For processing though, they are also converted into 12 bit PGM files. It is a non-proprietary format, which can easily be read by most

programming languages. Only these files, forming the second image database, will be used by our programs, for display and processing. Should a system failure occur and files get corrupted, the original images would not be affected, and would be used to rebuild the second database. We call *one input group* the set of four images (DAPI JPEG, DAPI PGM, FITC JPEG, FITC PGM) corresponding to one view.

B.2 *Comets* references

```
<?xml version="1.0" encoding="utf-8"?>
<!DOCTYPE reference SYSTEM "/telomeres/references.dtd">
<reference image="/MT002/MT002-1/1AG0000001" nbOfReferences="2">
   <comets id="c1" nbOfPoints="302">
      227 738 3.803030303030303 26.816120133932465
      227 739 3.787878787878788 26.865458004681624
      (...)
   </comets>
  <comets id="c2" nbOfPoints="335">
      774 512 3.1622776601683795 22.608380316123238
      774 513 3.1622776601683795 22.655732286889524
      (...)
   </comets>
</reference>
```

Figure B.3: *Reference database: XML file storing the references for an input group.*

The references for segmentation are defined as *Comets*. As explained in Section IV.2, one *Comets* is defined by its border points, and the inner and outer confidence factors at each border point. This is enough to build a confidence map of any size, either for display or processing. The references for each input group are stored in a distinct XML file. Figure B.3 shows an extract of such a file. The root `reference` has two attributes: the name of the corresponding input group, and the number of references defined. Each reference is stored as a sub-element `nucleus`; its attributes are a unique identifier and the number of vertices defined by the user. The body inside a `nucleus` lists the vertices' x and y coordinates, their inner and their outer confidence factors.

B.3 Segmentation results

A complete processing of one input group results in:

- a segmentation of the nuclei in the DAPI image,

```
<?xml version="1.0" encoding="utf-8"?>
<!DOCTYPE output SYSTEM "/telomeres/output.dtd">
<output image="/MT002/MT002-1/1AG0453" nbOfNuclei="2">
   <nucleus id="s1"                  nbOfVertices="185"   area="1844"
            nucleus_intens="1760103" probe_number="3"     probe_size="60"
            probe_intens="16980"     fitc_intens="243873">
      425 1021   426 1021   (...)   426 1020
   </nucleus>
   <nucleus id="s2"                  nbOfVertices="330"   area="9013"
            nucleus_intens="8934323" probe_number="28"    probe_size="534"
            probe_intens="218283"    fitc_intens="1757390">
      561 326   561 327   (...)   561 325
   </nucleus>
</output>
```

Figure B.4: *Output database: XML file storing the segmentation results of a given method on one input group.*

- a segmentation of the probes in the FITC image,
- a series of measurements in each segmented nucleus, such as the number of segmented probes or their intensities.

These results are stored in one XML file per input group. An example is shown in Figure B.4. The root `output` contains the input group and the number of segmented nuclei. Each sub-element `nucleus` has a unique identifier. Its attributes show the names and values of the measurements, while the body lists the x and y coordinates of the segmentation border's vertices. The attributes are used to perform statistics on the nuclei of each individual, as explained in Section III.3.

In addition to the XML file, the results of the two segmentations are drawn on top of the input JPEG images within the input group, and stored as two output JPEG files, for visual inspection of the segmentation results.

B.4 Evaluation of segmentation results

```
<?xml version="1.0" encoding="utf-8"?>
<!DOCTYPE evaluation SYSTEM "/telomeres/evaluation.dtd">
<evaluation image="/MT002/MT002-1/1AG0000001" nbOfEntries="2">
  <entry ref="c1" segm="s1">
    <measure name="Comets"          value="0.206901472150592"/>
    <measure name="DSC"             value="0.9280057968014078"/>
    <measure name="Hausdorff"       value="11.180339887498949"/>
    <measure name="MeanHausdorff"   value="3.93771243290371"/>
    <measure name="StdDevHausdorff" value="4.130745785111794"/>
    <measure name="RAO"             value="0.865681730397837"/>
    <measure name="RUMA"            value="1.0"/>
  </entry>
  <entry ref="c2" segm="s2">
    <measure name="Comets"          value="0.19796783664006048"/>
    <measure name="DSC"             value="0.9269553975436329"/>
    <measure name="Hausdorff"       value="14.142135623730951"/>
    <measure name="MeanHausdorff"   value="4.171888719835954"/>
    <measure name="StdDevHausdorff" value="4.574401197104007"/>
    <measure name="RAO"             value="0.863855421686747"/>
    <measure name="RUMA"            value="1.0"/>
  </pair>
</evaluation>
```

Figure B.5: *Evaluation database: XML file storing the evaluation of the segmentation results for one input group.*

The final database we use contains the results of the evaluation of a segmentation method. As detailed in Section III.3, we use an error matrix to store the discrepancies between references and segmented objects. Since this matrix is sparse, we only store the entries corresponding to overlapping references and objects (*i.e.* with a non-infinite *Comets* error). These entries are encoded in XML, with one file per input group, as illustrated in Figure B.5. The root `evaluation` contains the input group identifier and the number of matrix entries. Each sub-element `entry` lists the corresponding reference and object identifiers (corresponding to the entry's coordinates in the error matrix), and its body lists the discrepancy measures. Since more than one measure can be performed, we use a structured body with sub-elements `measure`. Each of them has two attributes: the measure's name and value.

```
<?xml version="1.0" encoding="utf-8"?>
<!DOCTYPE stats SYSTEM "/telomeres/stats.dtd">
<stat name="probe_number" case="/MT002/MT002-1/" nbOfNuclei="3234">
  <image name="1AG0453">
    <nucleus id="s1" value="3"/>
    <nucleus id="s2" value="28"/>
  </image>
  <image name="1AG0455">
    <nucleus id="s1" value="23"/>
    <nucleus id="s2" value="24"/>
  </image>
  (...)
</stat>
```

Figure B.6: *Statistics database: XML file storing the measurements performed on one input group.*

B.5 Statistics on individuals

When all images from one individual are segmented, the measures performed on the nuclei can be collected and presented graphically. Examples of graphs and histograms are presented in Section III.3. All measures are listed as attributes of sub-elements `nucleus` in the output database. Collecting the measures simply amount to transposing the presentation of the data, as shown in Figure B.6. Contrary to other databases, one XML file corresponds to one measure for one individual. Although these files are redundant with the output files, they allow a faster processing of results for all individuals. Indeed, parsing the output files for the measurements is slowed down by the necessary parsing of the vertices coordinates in the sub-elements bodies and the multiplicity of data files.

In the statistics database files, the image name and nucleus identifier are unique to each nucleus. Any nucleus in this database can be selected based on its measures, in particular interactively from a graph, and can be identified in the correct image by looking for its identifier in the corresponding output XML file.

C. Porting image processing to a cluster

C.1 Architecture

We implemented all our programs on a Mac OS X cluster with 16 dual-G5 nodes. Porting an image-processing program to a cluster can be achieved in different ways. Common methods are listed below:

1. Divide an image into several parts, have each part processed on a distinct node, and combine the results to obtain the processed image.

2. Divide the processing of one image into parallel steps, execute each step on a distinct node, and combine the results to obtain the processed image.

3. Divide the processing of one image into successive steps, execute each step on a given node, and have one node send its results to another node for the following step. This corresponds to a pipe of nodes specialised in one step, where the processed images are the output of the last node.

4. Divide the database into smaller groups of images, have each node process one group.

The first strategy cannot be applied to our segmentation methods. As described before, the segmentation of one image is based its entire contents. Splitting an image would also unavoidably clip nuclei into distinct subimages, and thus require extra processing to recover them afterwards. The second strategy is not adapted to our processing either. We use successive processing steps, which cannot run in parallel. The third strategy is only efficient when all the processing steps take approximately the same time to execute. This is not the case of our processing. In particular the segmentation nuclei is significantly longer than the probe segmentation. Using pipes of nodes would result in delays and sub-optimal use of the computing power.

The final strategy is better suited to our needs. The database of images we

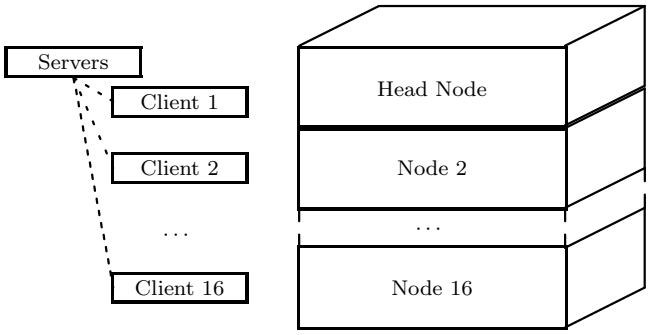

Figure C.1: *Client-Server architecture: location of the main processes on the cluster nodes.*

use contains nearly 3,000 images, which is far greater than the number of nodes in our cluster. However, dividing the database into 16 groups beforehand has two main drawbacks. First, some nodes may finish their batch earlier than others, but they would not be able to help them process their remaining images, thus wasting processing time. Second and more importantly, should a system failure occur on a node, all the images which were to be processed there would remain unprocessed at the end. Thus, it would be non-efficient and not robust. To avoid these two issues, we implemented a strategy based on a dynamic task allocation, with a client-server architecture.

The server is used only to distribute the images for processing. Each client requests an image from the server, processes it on its own, then send the processed image back, and requests another image. For programming reasons, each client communicates with a dedicated server, which in turns communicate with the main server. The servers are light processes and can run on the same cluster node as another client (See Figure C.1). Slight bottlenecks could happen in case many clients require an image at the same time. In practice however, since each node takes a different time to process its current image, the image requests occur at different times, and clients never have to wait significantly to obtain another image to process.

This way, all clients are busy at all time, until the server reaches the end of the database. This strategy ensures an optimal use of computation time on all the nodes of the cluster. Besides, in case of system failure on a node, the server will keep sending the remaining images to all other nodes. Only the image being processed at the time of the failure will be unprocessed. At the end the server will easily identify unprocessed images, and reassign them to an active node. Our strategy ensures an optimal and robust use of the cluster computing power.

C.2 Protocols

The protocols we use rely on exchanges of bytes between the communicating processes: either single bytes for standard messages, strings for file names, or arrays of bytes for file contents. Opening sockets and exchanging bytes over them can be programmed with the standard Java classes for input and output.

We use five protocols: one to start the communications, one to transfer a file, one to convert files from TIFF to PGM and JPEG, one to segment an input group, and one to end communications. They are presented in Tables C.1 to C.2. In these tables, the vertical dots indicate that a process is waiting to receive a network message, and the arrows show which process is sending a message to which. The standard messages we use are encoded as different bytes. For readability, we use names, in small capitals, instead of values to present them in the tables below. They are: REQUEST_TASK, SENDING_FILE, FILE_RECEIVED, CONVERT, SEGMENT, END.

Table C.1: *Protocol for communication opening.*

Main Server		*Dedicated Server i*		*Client i*
start				start
⋮		⟵		ask for connection
launch	⟶	start		⋮
⋮		register connection	⟶	connect
⋮		⋮	⟵	send REQUEST_TASK
⋮	⟵	send REQUEST_TASK		⋮
prepare a task		⋮		⋮

Table C.2: *Protocol for communication ending.*

Main Server		*Dedicated Server i*		*Client i*
send END	⟶	⋮		⋮
⋮		send END	⟶	⋮
⋮		close connections		close connections
⋮		end thread		end thread

Table C.3: *Protocol for file transfer.*

Sender		*Receiver*
		⋮
send SENDING_FILE	⟶	prepare for reception
send file name	⟶	store file name
send file size	⟶	store file size
send file contents	⟶	store file contents
prepare to compare	⟵	send FILE_RECEIVED
⋮	⟵	send local file size
compare with original file size - if different, start over - else, proceed to next step		⋮
Summarised as:		
send file	⟶	store file

Table C.4: *Protocol for the conversion task.*

Main Server		*Dedicated Server i*		*Client i*
send CONVERT	⟶	⋮		⋮
		send CONVERT	⟶	prepare for conversion
send file names	⟶	find the files		⋮
⋮		send TIFF files	⟶	store files
⋮		⋮		convert files
⋮		store files	⟵	send JPEG, PGM files
⋮		⋮	⟵	send REQUEST_TASK
⋮	⟵	send REQUEST_TASK		⋮
prepare a task		⋮		⋮

Table C.5: *Protocol for the segmentation task.*

Main Server		*Dedicated Server i*		*Client i*
send SEGMENT	→	⋮		⋮
		send SEGMENT	→	prepare for segmentation
send input group name	→	find the files		⋮
⋮		send JPEG, XML files	→	store files
⋮		⋮		segment images
⋮		store files	←	send JPEG, XML files
⋮		⋮	←	send REQUEST_TASK
⋮	←	send REQUEST_TASK		⋮
prepare a task		⋮		⋮

C.3 Results and discussion

The architecture and protocols presented above allow any number of clients to connect to the main server, at any time, and minimise the losses in case of a client failure. In particular, clients can be started on any computer connected to the cluster, and more than one client can be started on any computer. In this section we discuss the effect of running multiple clients on the cluster nodes. We performed the conversion and segmentation of the whole data base with 1, 2, and 3 clients running per node. We present the average elapsed time spent by each client on each image, detailed for each subtask of the conversion and the segmentation, in Figure C.2. The head node is equipped with 1Gb RAM, while the other nodes have 256 Mb RAM each. As they have a slightly different configuration, we present the results averaged over all clients, then over all clients on the head node, and over all clients on the other nodes. The total elapsed times needed to process the whole database are presented in Table C.6.

Table C.6: *Total elapsed time to process the whole database on the cluster, depending on the number of clients running per node.*

	1 client	2 clients	3 clients	2 clients with compression
Conversion	23' 49"	22' 08"	29' 39"	21' 06"
Segmentation	35' 30"	36' 57"	60' 33"	66' 10"

Judging from Figure C.2, adding clients on a node slows the processing down. The effect is less severe on the head node, where more memory is available, than

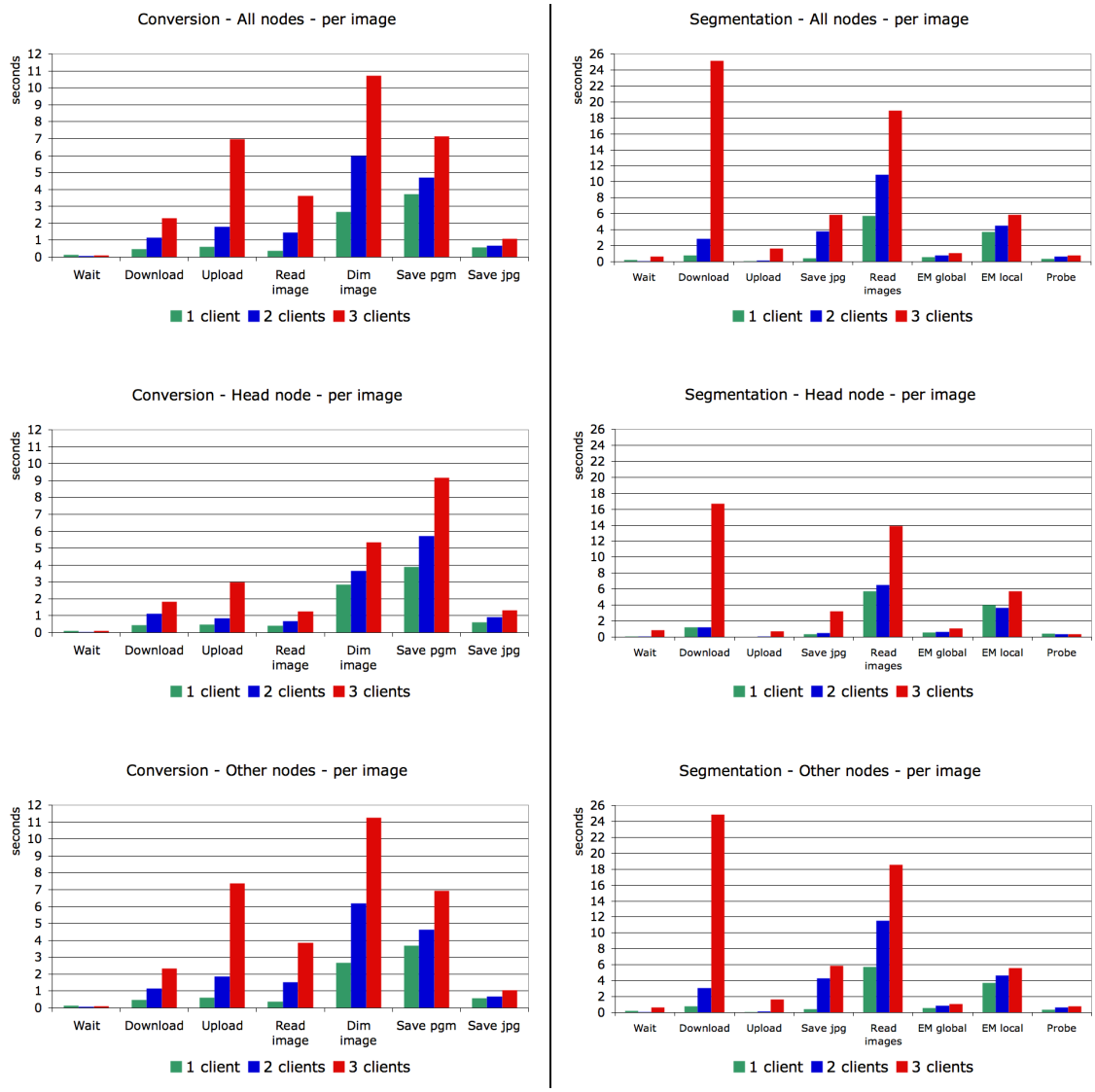

Figure C.2: *Processing times as functions of the number of clients running per node, performing conversion (left column) and segmentation (right column). The top row shows the average time per client, the middle row per client on the head node, and the bottom row per client on the other nodes.*

on the other nodes. In addition to competing for memory and CPU time, the clients also compete for network bandwidth. Adding more clients degrades the time needed to upload a converted input group: the operation is about 12 times slower on average with three clients than with one. Similarly, it affects the time needed to download an input group prior to segmentation: it is about 30 times slower with three clients than with one.

Adding more clients increases the time spent to process an image, but also reduces the total number of images processed by each client, as they share the load. Overall, the total time needed to process the whole database, either for conversion or segmentation, in Table C.6, is similar with one and two clients per node, but significantly higher with three clients per node. In the latter case, most of the time is spent on uploading and downloading data over the network. Copying the whole database on each node prior to processing would be against the flexibility provided by the architecture, as it would prevent the later addition of extra nodes to the cluster, and would require a significant amount of time and space, while duplicating a database in sixteen copies and causing maintenance issues. Another solution consists in compressing the files prior to transmitting them over the network. Compression is easily implementable with the standard Java distribution. We experimented file compression running two clients per node. Although the total conversion time is smaller (21' 06"), segmentation is significantly higher (66' 10"). This is due to the decompression step needed prior to segmentation. In our context, conversion is performed once on the whole database, while segmentation is performed as many times as needed for tuning and comparison of different methods. The small gain of conversion time is thus not enough to balance the large loss of segmentation time. We decided to perform all the tasks with one single client per node, and without any compression.

D. Software interfaces for segmentation and evaluation

In this section we present the interfaces we developed to performed the different tasks described in this work.

D.1 Defining and visualising *Comets*

The interface used to define *Comets* references consists of two parts, as illustrated in Figure D.1. The left-hand side part allows the navigation through the image database, by choosing the directory corresponding to an individual and selecting an input group to work on. The DAPI and FITC components may be displayed separately or together. The component chosen is displayed in the right-hand side of the interface. The user draws the border by dragging the mouse, and defines the inner and outer confidence pixels with single clicks. The computation are then performed automatically and the *Comets* is stored in an XML format, as detailed above.

D.2 Tuning and using a segmentation method

The interface developed to choose a segmentation and tune its parameters is similar to the one described above, and is illustrated in Figure D.2. In the left-hand side panel, the use can choose an individual, an input group, and a component to display. In addition, the segmentation method' parameters are listed and can be modified by the user, before launching the segmentation on the current image. The results, presented in the right-hand side, can be saved for each image. Once the user has chosen parameters, they can run the method on the whole database of images, by opening another interface described next.

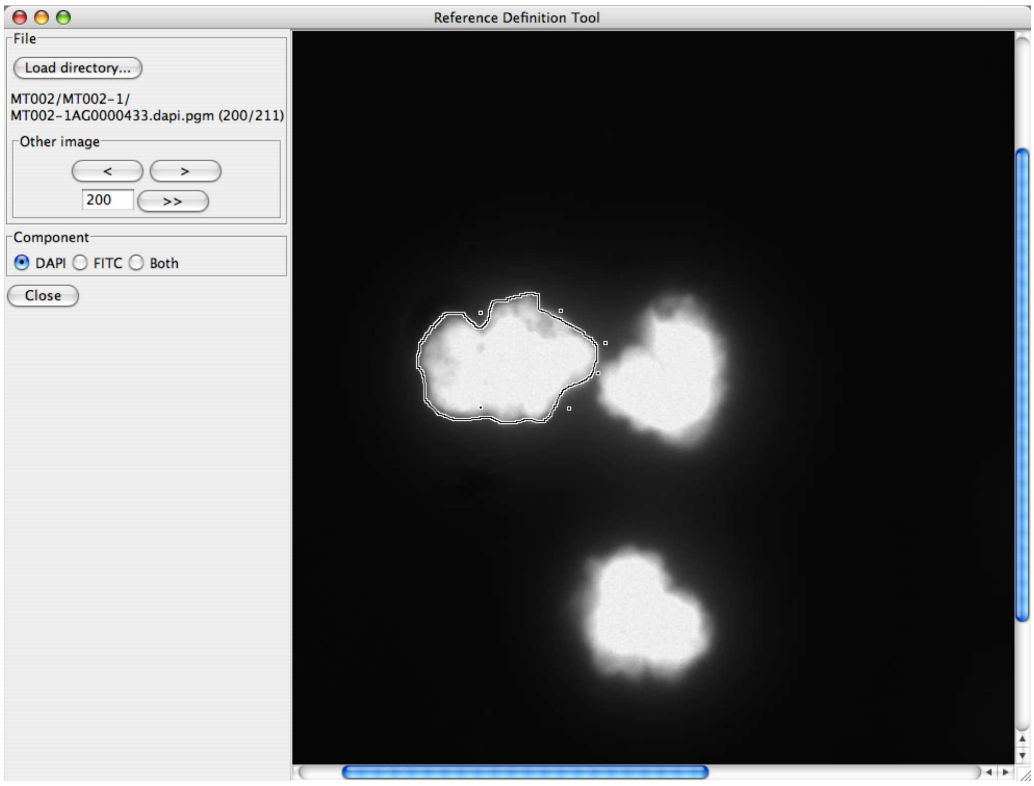

Figure D.1: *Interface to define* Comets *references.*

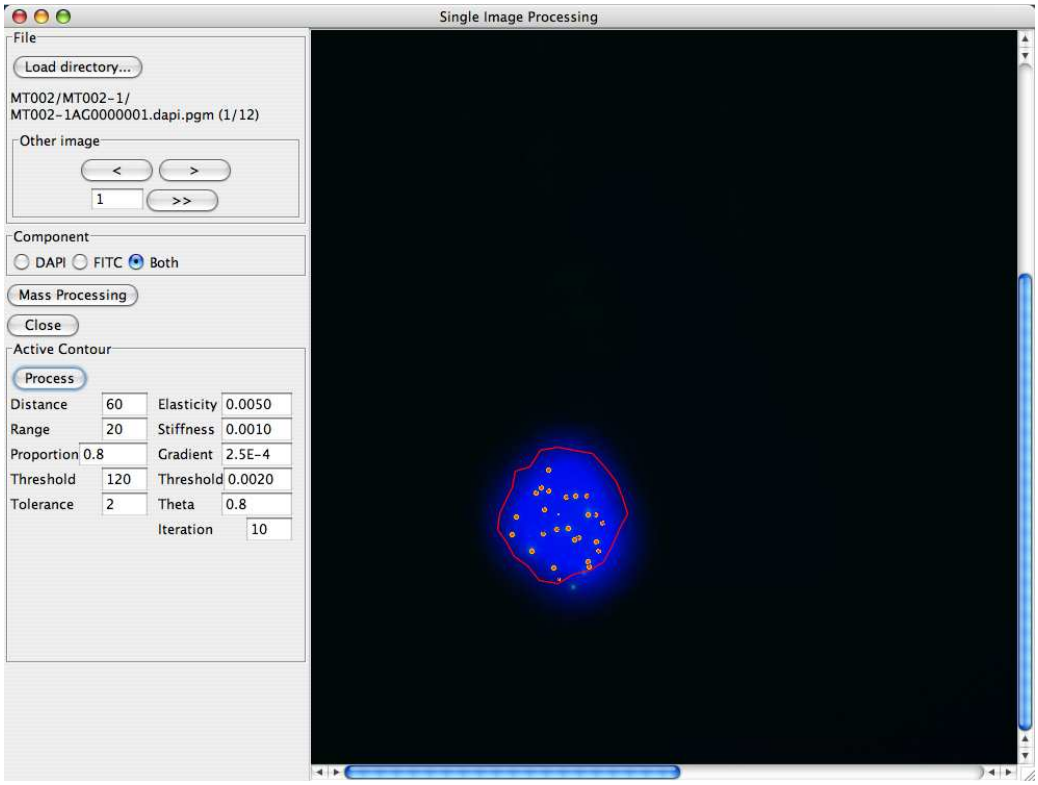

Figure D.2: *Interface to tune a segmentation method's parameters on single images.*

D.3 Visualising the processing on a cluster

As described above in this chapter, the clients open connections with the main server and receive orders from it, through dedicated servers. A light addition to the protocols described above allows the clients to pass messages to the main server at any time. These messages can be visualised in real-time.

The interface used to visualise the current status of all nodes on the cluster is presented in Figure D.3. On the left-hand side panel, the proportion of images processed overall and per individual is presented graphically, along with the total elapsed time. The right-hand side panel shows information on the clients: their current status, as reported from them, and the number of images they have processed.

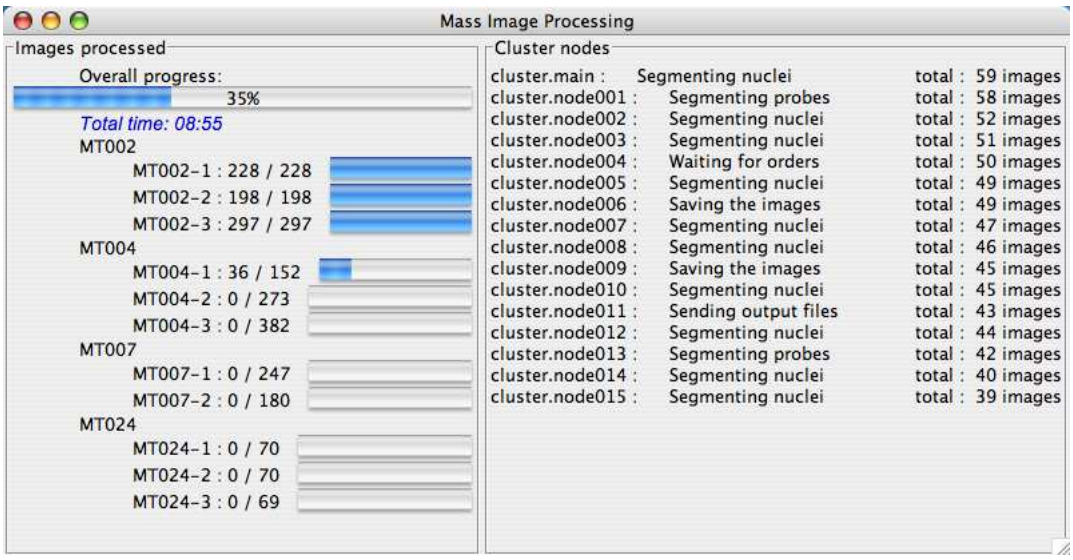

Figure D.3: *Interface to visualise the status of all nodes processing images on a cluster.*

D.4 Visualising measures on different individuals

The final interface we present here is used to display the various measures performed on the individuals in our data base, as detailed in Chapter III. It is illustrated in Figure D.4. In the left-hand side panel, the user can choose one or more individual, the values to display, and the bin size of the histograms. Other options allow filtering nuclei that are clipped at the edges of an image, and listing the number of nuclei segmented for each individual.

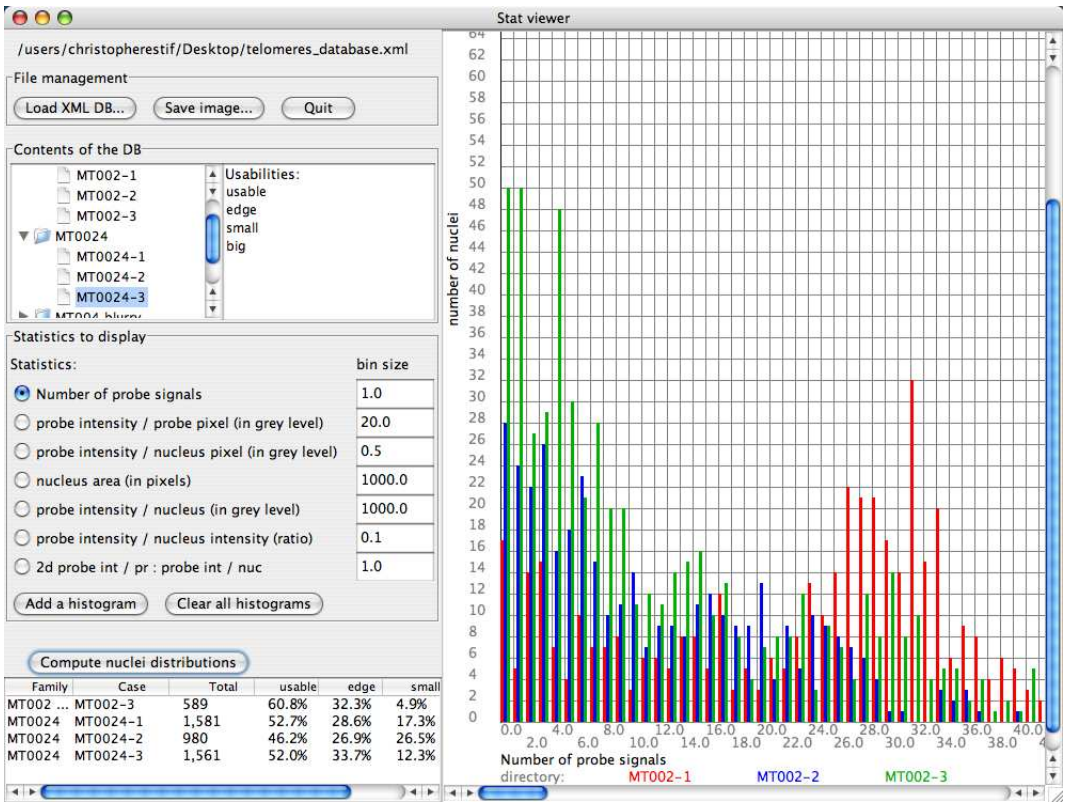

Figure D.4: *Interface to visualise the measures on different individuals.*

Bibliography

[1] Wael Abd-Almageed, Christopher E. Smith, and Samah Ramadan. Kernel snakes: Non-parametric active contour models. In *International Conference on Systems, Man, and Cybernetics*, volume 1, pages 240–244, Washington, DC, USA, October 2003.

[2] David Adalsteinsson and James A. Sethian. A fast level set method for propagating interfaces. *Journal of Computational Physics*, 118(2):269–277, May 1995.

[3] Dwi Anoraganingrum. Cell segmentation with median filter and mathematical morphology operation. In *International Conference on Image Analysis and Processing*, pages 1043–1046, Venice, Italy, September 1999.

[4] A. Antsaklis, N. Papantoniou, S. Mesogitis, S. Michalas, and D. Aravantinos. Pregnant women of 35 years of age or more: maternal serum markers or amniocentesis? *Journal of Obstetrics and Gynaecology*, 19(3):253–256, May 1999.

[5] Tatiana Babochkina, Susanne Mergenthaler, Guiseppina De Napoli, Sashka Hristoskova, Sevgi Tecanli, Wolfgang Holzgreve, and Sinuhe Hahn. Numerous erythroblasts in maternal blood are impervious to fluorescent in situ hybridization analysis, a feature related to a dense compact nucleus with apoptic character. *Haematologica*, 90(6):739–744, 2005.

[6] Gabriela M. Baerlocher, Jennifer Mak, Teri Tien, and Peter M. Lansdorp. Telomere length measurements by fluorescence in situ hybridization and flow cytometry: tips and pitfalls. *Cytometry*, 47:89–99, 2002.

[7] EunSang Bak, Kayvan Najarian, and John P. Brockway. Efficient segmentation framework of cell images in noise environments. Technical report, Memory Testing Corporation, USA, 2004.

[8] Lucia Ballerini and Leonardo Bocchi. Segmentation of liver images by texture and genetic snakes. In *European Medical and Biological Engineering Conference*, Vienna, Austria, December 2002.

[9] Lucia Ballerini and Leonardo Bocchi. Bone segmentation using multiple communicating snakes. In *SPIE Medical Imaging*, volume 5032, pages 1621–1628, San Diego, CA, USA, February 2003.

[10] Pascal Bamford. *Segmentation of Cell Images With Application to Cervical Cancer Screening*. PhD thesis, University of Queensland, 1999.

[11] Pascal Bamford. Automating cell segmentation evaluation with annotated examples. In *APRS Workshop on Digital Image Computing*, pages 21–25, Brisbane, Australia, February 2003.

[12] Pascal Bamford and Brian Lovell. Method for accurate unsupervised cell nucleus segmentation. In *IEEE Engineering in Medicine and Biology*, volume 1, pages 133–137, Istanbul, Turkey, October 2001.

[13] Julian Besag. On the statistical analysis of dirty pictures. *Journal of the Royal Statistical Society. Series B*, 48(3):259–302, 1986.

[14] S. Beucher. The watershed transformation applied to image segmentation. *Scanning Microscopy*, 6:299–314, 1992.

[15] Andrew Blake and Michael Isard. *Active Contours*. Springler-Verlag, 1998. ISBN 3-540-76217-5.

[16] W. Bocker, H-W Gantenberg, W-U Muller, and C. Streffer. Automated cell cycle analysis with fluorescence microscopy and image analysis. *Physics in Medicine and Biology*, 41:523–537, 1996.

[17] Yuri Y. Boykov and Marie-Pierr Jolly. Interactive graph cuts for optimal boundary and region segmentation of objects in n-d images. In *International Conference on Computer Vision*, volume 1, pages 105–112, Vancouver, Canada, July 2001.

[18] Jörg Bredno, Thomas M. Lehmann, and Klauss Spitzer. A general finite element model for segmentation in 2, 3, and 4 dimensions. In *SPIE Medical Imaging*, volume 3979, pages 1174–1184, San Diego, CA, USA, February 2000.

[19] Jörg Bredno, Thomas M. Lehmann, and Klauss Spitzer. A general discrete contour model in two, three and four dimensions for topology-adaptive multichannel segmentation. *IEEE Transactions on Pattern Analysis and Machine Intelligence*, 25(5):550–563, May 2003.

[20] Patrick Brigger, Jeff Hoeg, and Michael Unser. B-spline snakes: A flexible tool for parametric contour detection. *IEEE Transactions on Image Processing*, 9(9):1484–1496, September 2000.

[21] Patrick Brigger, Frank Muller, Klaus Illgner, and Michael Unser. Centered pyramids. *IEEE Transactions on Image Processing*, 8(9):1254–1264, September 1999.

[22] Tim H. Brümmendorf, Jaroslaw P. Maciejewski, Jennifer Mak, Neal S. Young, and Peter M. Lansdorp. Telomere length in leukocyte subpopulations of patients with aplastic anemia. *Blood*, 97(4):895–900, 2001.

[23] Peter J. Burt and Edward H. Adelson. The Laplacian pyramid as a compact image code. *IEEE Transactions on Communications*, COM-31(4):532–540, April 1983.

[24] Kerstin Bystricky, Patrick Heun, Lutz Gehlen, Jörg Langowski, and Susan M. Gasser. Long-range compaction and flexibility of interphase chromatin in budding yeast analyzed by high-resolution imaging techniques. *PNAS*, 101(47):16495–16500, November 2004.

[25] Nigel P. Carter. Fluorescence in situ hybridization – state of the art. *Bioimaging*, 4:41–51, 1996.

[26] Vicent Caselles, Ron Kimmel, and Guillermo Sapiro. Geodesic active contours. In *International Conference on Computer Vision*, pages 694–699, Boston, MA, USA, June 1995.

[27] Vincent Caselles, Ron Kimmel, and Guillermo Sapiro. Geodesic active contours. *International Journal of Computer Vision*, 22(1):61–79, February / March 1997.

[28] D. Casey, C. Cantor, and S. Spengler. Primer on molecular genetics. Technical report, US Department of Energy, DOE Human Genome Project, Oak Ridge National Laboratory, 1060 Commerce Park, Oak Ridge, TN 37830, June 1992.

[29] Francis H.Y. Chan, F.K. Lam, and Hui Zhu. Adaptive thresholding by variational method. *IEEE Transactions on Image Processing*, 7(3):468–473, March 1998.

[30] Su Chen and Robert Haralick. Recursive erosion, dilation, opening, and closing transforms. *IEEE Transactions on Image Processing*, 4(3):335–345, March 1995.

[31] Xiaohua Chen, Michael Brady, and Daniel Rueckert. Simultaneous segmentation and registration for medical image. In *Medical Image Computing and Computer-Assisted Intervention*, volume 1, pages 663–670, Saint-Malo, France, September 2004.

[32] Yunmei Chen, Feng Huang, Hemant D. Tagare, Murali Rao, David Wilson, and Edward A. Geiser. Using prior shape and intensity profile in medical image segmentation. In *International Conference on Computer Vision*, pages 1117–1124, Nice, France, October 2003.

[33] Yunqiang Chen, Thomas S. Huang, and Yong Rui. Optimal radial contour tracking by dynamic programming. In *International Conference on Image Processing*, volume 1, pages 626–629, Thessaloniki, Greece, October 2001.

[34] Ward Cheney and David Kincaid. *Numerical Mathematics and Computing*. Brooks/Cole Publishing, fourth edition, 1999. ISBN 0-534-35184-0.

[35] William F. Clocksin. Automatic segmentation of overlapping nuclei with high background variation using robust estimation and flexible contour models. In *International Conference on Image Analysis and Processing*, pages 682–687, Mantova, Italy, September 2003.

[36] William F. Clocksin and Boaz Lerner. Automatic analysis of fluorescence in-situ hybridisation images. In *British Machine Vision Conference*, pages 666–674, Bristol, UK, September 2000.

[37] Laurent D. Cohen. On active contour models and balloons. *Computer Vision, Graphics, and Image Processing: Image Understanding*, 53(2):211–218, March 1991.

[38] Timothy F. Cootes, Gareth J. Edwards, and Christopher J. Taylor. Comparing active shape models with active appearance models. In *British Machine Vision Conference*, pages 173–182, Nottingham, UK, September 1999.

[39] Timothy F. Cootes and Christopher J. Taylor. Statistical models of appearance for medical image analysis and computer vision. In *SPIE Medical Imaging*, volume 4322, pages 236–248, San Diego, CA, USA, February 2001.

[40] Timothy F. Cootes, Carole J. Twining, Vladimir Petrović, Roy Schestowitz, and Christopher J. Taylor. Groupwise construction of appearance models using piece-wise affine deformations. In *British Machine Vision Conference*, volume 2, pages 879–888, Oxford, UK, September 2005.

[41] Timothy F. Cootes, Carole J. Twining, and Christopher J. Taylor. Diffeomorphic statistical shape models. In *British Machine Vision Conference*, volume 1, pages 447–456, London, UK, September 2004.

[42] Thomas H. Cormen, Charles E. Leiserson, and Ronald L. Rivest. *Introduction to Algorithms*. Addison Wesley, first edition, 1990. ISBN 0-262-03141-8.

[43] William R. Crum, Oscar Camara, Daniel Rueckert, Mark Jenkinson, and Derek L.G. Hill. Evaluating atlas segmentation of multiple structures using generalised measures of region overlap. In *Medical Image Understanding and Analysis*, pages 163–166, Bristol, UK, July 2005.

[44] Michael B. Dillencourt, Hannan Samet, and Markku Tamminen. A general approach to connected-component labeling for arbitrary image representations. *Journal of the Association for Computing Machinery*, 39(2):253–280, April 1992.

[45] Edward Dougherty and Roberto Lotufo. *Hands-on Morphological Image Processing*, volume TT59, chapter 5 Gray-Scale Morphology, pages 81–120. SPIE, July 2003.

[46] Edward Dougherty and Roberto Lotufo. *Hands-on Morphological Image Processing*, volume TT59, chapter 6 Morphological Process of Gray-Scale Images, pages 121–138. SPIE, July 2003.

[47] Edward Dougherty and Roberto Lotufo. *Hands-on Morphological Image Processing*, volume TT59, chapter 7 Morphological Segmentation - Watershed, pages 139–154. SPIE, July 2003.

[48] Nick Efford. *Digital Image Processing – a practical introduction using Java*. Addison Wesley, 2000. ISBN: 0-201-59623-7.

[49] M. Egmont-Petersen, D. de Ridder, and H. Handels. Image processing with neural networks – a review. *Pattern Recognition*, 35:2279–2301, 2002.

[50] Bing Fang, Wynne Hsu, and Mong Li Lee. On the accurate counting of tumor cells. *IEEE Transactions on Nanobioscience*, 2(2):94–103, June 2003.

[51] Pedro F. Felzenszwalb and Daniel P. Huttenlocher. Distance transforms of sampled functions. Technical report, Cornell University, September 2004. TR2004-1963.

[52] Samuel D. Fenster, Chun-Bin Gary Kuo, and John R. Kender. Nonparametric training of snakes to find indistinct boundaries. In *CVPR Workshop on Mathematical Methods in Biomedical Image Analysis*, Kauai, Hawaii, USA, December 2001.

[53] Alban Foulonneau, Pierre Charbonnier, and Fabrice Heitz. Affine-invariant multi-reference shape priors for active contours. In Aleš Leonardis, Horst Bischof, and Axel Pinz, editors, *European Conference on Computer Vision*, volume 3952 of *LNCS*, pages 601–613. Springer, 2006.

[54] Guido Gerig, Matthieu Jomier, and Miranda Chakos. Valmet: A new validation tool for assessing and improving 3D object segmentation. In *Medical Image Computing and Computer-Assisted Intervention*, Utrecht, The Netherlands, October 2001.

[55] V. Grau, A.U.J. Mewes, M. Alcaniz, R. Kikinis, and S.K. Warfield. Improved watershed transform for medical image segmentation using prior information. *IEEE Transactions on Medical Imaging*, 23(4):447–458, 2004.

[56] W.E.L. Grimson, Michael E. Leventon, Olivier Faugeras, and William Wells. Computer vision methods for image guided surgery. In *British Machine Vision Conference*, pages 1–12, Bristol, UK, September 2000.

[57] Yu Guo, Sebrina Levesque, Thomas Manfred, and Ying Sun. Automated detection and delineation of mitochondria in electron micrographs of human skeletal muscles. *Microscopy research and technique*, 63(3):133–139, February 2004.

[58] James E. Haddow, Glenn E. Palomaki, George J. Knight, George C. Cunningham, Linda S. Lustig, and Patricia A. Boyd. Reducing the need for amniocentesis in women 35 years of age or older with serum markers for screening. *New England Journal of Medicine*, 330:1114–1118, April 1994.

[59] Sinuhe Hahn and Wolfgang Holzgreve. *Fetal cells and Fetal DNA in maternal blood*. Karger, Basel, Switzerland, 2001.

[60] Sinuhe Hahn, Rosalie Sant, and Wolfgang Holzgreve. Fetal cells in maternal blood: current and future perspectives. *Molecular Human Reproduction*, 4(6):515–521, 1998.

[61] Ghassan Hamarneh, Tim McInerney, and Dimitri Terzopoulos. Deformable organisms for automatic medical image analysis. In *Medical Image Computing and Computer-Assisted Intervention*, pages 66–75, Utrecht, The Netherlands, October 2001.

[62] Xiao Han, Chenyang Xu, and Jerry L. Prince. A topology preserving level set method for geometric deformable models. *IEEE Transactions on Pattern Analysis and Machine Intelligence*, 25(6):755–768, June 2003.

[63] Calvin B. Harley, A. Bruce Futcher, and Carol W. Greider. Telomeres shorten during ageing of human fibroblasts. *Nature*, 345(6274):458–460, May 1990.

[64] Harald Hohmann, Susanne Michel, Wolfgang Reiber, Michael Gunther, Uwe Claussen, and Ferdinand von Eggeling. How to enrich and analyse fetal cells from maternal blood: 5-year experience with PCR, FISH and cultivation. In *Fetal Cells and Fetal DNA in Maternal Blood - New Developments for a New Millennium*, pages 47–55. Karger, 2001.

[65] Wolfgang Holzgreve, Xiao Yan Zhong, Carolyn Troeger, Isabelle Haari, Vivian Kiefer, and Sinuhe Hahn. Fetal cells in maternal blood: An overview of the Basel experience. In *Fetal Cells and Fetal DNA in Maternal Blood - New Developments for a New Millennium*, pages 28–36. Karger, 2001.

[66] Adam Hooverand, Gillian Jean-Baptiste, Xiaoyi Jiang, Patrick J. Flynn, Horst Bunke, Dmitry B. Goldgof, Kevin Bowyer, David W. Eggert, Andrew Fitzgibbon, and Robert B. Fisher. An experimental comparison of range image segmentation algorithms. *IEEE Transactions on Pattern Analysis and Machine Intelligence*, 18(7):673–689, July 1996.

[67] Wu-Chih Hu and Hsin-Teng Sheu. Quadratic B-spline for curve fitting. *National Science Council Republic of China*, 24(5):373–381, 2000.

[68] James P. Ivins. *Statistical Snakes: Active Region Models*. PhD thesis, University of Sheffield, 1996.

[69] James P. Ivins and John Porrill. Everything you always wanted to know about snakes (but were afraid to ask). Technical report, AIVRU, University of Sheffield, March 2000.

[70] Mathews Jacob. *Parametric Shape Processing in Biomedical Imaging*. PhD thesis, Ecole Polytechnique fédérale de Lausanne, 2003.

[71] Torsten Jarkrans. *Algorithms for Cell Image Analysis in Cytology and Pathology*. PhD thesis, Uppsala University, 1996.

[72] Stéphanie Jehan-Besson and Michel Barlaud. DREAM^{2}S: deformable regions driven by an Eulerian accurate minimization method for image and video segmentation. *International Journal of Computer Vision*, 53(1):45–70, 2003.

[73] Stéphanie Jehan-Besson, Michel Barlaud, Gilles Aubert, and Olivier Faugeras. Shape gradients for histogram segmentation using active contours. In *International Conference on Computer Vision*, pages 408–415, Nice, France, October 2003.

[74] Dong Joong Kang. A fast and stable snake algorithm for medical images. *Pattern Recognition Letters*, 20:507–512, 1999.

[75] Martin Kerschner. Homologous twin snakes integrated in a bundle block adjustment. In *Symposium on Object Recognition and Scene Classification from Multispectral and Multisensor Pixels*, volume 32, pages 244–249, Colombus, Ohio, USA, July 1998.

[76] Jeong-Gyoo Kim and J. Alison Noble. Modelling an average shape. In *Medical Image Understanding and Analysis*, pages 65–68, Sheffield, UK, July 2003.

[77] Pushmeet Kohli and Philip H.S. Torr. Measuring uncertainty in graph cut solutions - efficiently computing min-marginal energies using dynamic graph cuts. In *European Conference on Computer Vision*, pages 30–43, Graz, Austria, May 2006.

[78] A. Kolialexi, G. T. Tsangaris, A. Antsaklis, S. Kitsiou-Tzeli, and A. Mavrou. Use of annexin v for the identification of fetal cells in maternal circulation. *In Vivo*, 18(5):629–632, September-October 2004.

[79] Vladimir Kolmogorov and Ramin Zabih. What energy functions can be minimized via graph cuts? *IEEE Transactions on Pattern Analysis and Machine Intelligence*, 26(2):147–159, February 2004.

[80] Steen Kølvraa, Britta Christensen, Lene Lykke-Hansen, and John Philip. The fetal erythroblast is not the optimal target for non-invasive prenatal diagnosis: preliminary results. *Journal of Histochemistry and Cytochemistry*, 53(3):331–336, March 2005.

[81] Domagoj Kovacevic, Sven Loncaric, and Erich Sorantin. Deformable contour based method for medical image segmentation. In *International Conference on Information Technology Interfaces*, pages 145–150, Zagreb, Croatia, 1999.

[82] Gerald Kuhne, Joachim Weickert, Markus Beier, and Wolfgang Effelsberg. Fast implicit active contour models. *Pattern Recognition*, 2449:133–140, 2002.

[83] B. Ravi Kumar, Danny K. Joseph, and T. T. Sreenivas. Teager energy based blood cell segmentation. *Digital Signal Processing*, 2:619–622, July 2002.

[84] M. Pawan Kumar, Philip H.S. Torr, and Andrew Zisserman. Obj-cut. In *Computer Vision and Pattern Recognition*, volume 1, pages 18–25, San Diego, CA, USA, June 2005.

[85] Zoltan Kutalik, Moe Razaz, and Jozsef Baranyi. Automated spatial and temporal image analysis of bacterial cell growth. In *BMVA Symposium on Spatiotemporal Image Processing*, London, UK, March 2004.

[86] Peter M. Lansdorp, Nico P. Verwoerd, Frans M. van de Rijke, Visia Dragowska, Marie-Térèse Little, Roeland W. Dirks, Anton K. Raap, and Hans J. Tanke. Heterogeneity in telomere length of human chromosomes. *Human Molecular Genetics*, 5(5):685–691, 1996.

[87] Robert Lapp, Maria Lorenzo-Valdes, and Daniel Rueckert. 3D/4D cardiac segmentation using active appearance models, non-rigid registration, and the Insight tool. In *Medical Image Computing and Computer-Assisted Intervention*, pages 419–426, Saint-Malo, France, September 2004.

[88] Ole Vilhelm Larsen, Petia Radeva, and Enric Marti. Guidelines for choosing optimal parameters of elasticity for snakes. In *International Conference on Computer Analysis and Image Processing*, volume 970, pages 106–113, Prague, Czech Republic, September 1995.

[89] Sébastien Lefèvre, Jean-Pierre Gérard, Aurélie Piron, and Nicole Vincent. An extended snake model for real-time multiple object tracking. In *Advanced Concepts for Intelligent Vision Systems*, pages 268–275, Ghent, Belgium, September 2002.

[90] Thomas Lehmann, Jörg Bredno, and Klauss Spitzer. On the design of active contours for medical image segmentation. *Methods of Information in Medicine*, 42(1):89–98, 2003.

[91] Thomas M. Lehmann. From plastic to gold: A unified classification scheme for reference standards in medical image processing. In *Medical Imaging 2002: Image Processing*, volume 4684, pages 1819–1827, San Diego, CA, USA, February 2002.

[92] Boaz Lerner, William F. Clocksin, Seema Dhanjal, Maj A. Hultén, and Christopher M. Bishop. Automatic signal classification in fluorescence in situ hybridization images. *Cytometry*, 43:87–93, 2001.

[93] Boaz Lerner, William F. Clocksin, Seema Dhanjal, Maj A. Hultén, and Christopher M. Bishop. Feature representation and signal classification in

fluorescence in-situ hybridization image analysis. *IEEE Transactions on Systems, Man, and Cybernetics - Part A: Systems and Humans*, 31(6):655–665, November 2001.

[94] Michael E. Leventon, W.E.L. Grimson, and Olivier Faugeras. Statistical shape influence in geodesic active contours. In *Computer Vision and Pattern Recognition*, volume 1, pages 316–323, Hilton Head Island, South Carolina, USA, June 2000.

[95] Jeffrey M. Levsky and Robert H. Singer. Fluorescence in situ hybridization: past, present and future. *Journal of Cell Science*, 116:2833–2838, 2003.

[96] Olivier Lezoray, Abder Elmoataz, Hubert Cardot, and Marinette Revenu. A.R.C.T.I.C : Un systeme automatique de tri cellulaire par analyse d'images. In *Vision Interface*, Trois-Rivières, Canada, May 1999.

[97] Qingmin Liao and Yingying Deng. An accurate segmentation method for white blood cell images. In *International Symposium on Biomedical Imaging*, pages 245–248, Washington, DC, USA, July 2002.

[98] Gang Lin, Umesh Adiga, Kathy Olson, John Guzowski, Carol Barnes, and Badrinath Roysam. A hybrid 3D watershed algorithm incorporating gradient cues and object models for automatic segmentation of nuclei in confocal image stacks. *Cytometry*, 56A(1):23–36, November 2003.

[99] Marie-Térèse Little, Sylvie Langlois, R. Douglas Wilson, and Peter M. Lansdorp. Frequency of fetal cells in sorted subpopulations of nucleated erythroid and cd34+ hematopoietic progenitor cells from maternal peripheral blood. *Blood*, 89(7):2347–2358, April 1997.

[100] Steven Lobregt and Max A. Viergever. A discrete dynamic contour model. *IEEE Transactions on Medical Imaging*, 14(1):12–24, March 1995.

[101] Suhuai Luo, Rongxin Li, and Sébastien Ourselin. A new deformable model using dynamic gradient vector flow and adaptive balloon forces. In *APRS Workshop on Digital Image Computing*, pages 9–14, Brisbane, Australia, February 2003.

[102] Mahnaz Maddah, Kelly H. Zou, William M. Wells, Ron Kikinis, and Simon K. Warfield. Automatic optimization of segmentation algorithms through simultaneous truth and performance level estimation (STAPLE). In *Medical Image Computing and Computer-Assisted Intervention*, volume 1, pages 274–282, Saint-Malo, France, September 2004.

[103] Ravikanth Malladi, James A. Sethian, and Baba C. Vemuri. Shape modeling with front propagation: A level set approach. *IEEE Transactions on Pattern Analysis and Machine Intelligence*, 17(2):158–175, February 1995.

[104] Norberto Malpica, Carlos Ortiz de Solórzano, Juan José Vaquero, Andrés Santos, Isabel Vallcorba, José Miguel García-Sagrado, and Francisco del Pozo. Applying watershed algorithms to the segmentation of clustered nuclei. *Cytometry*, 28:289–297, 1997.

[105] Matei Mancas and Bernard Gosselin. Fuzzy tumor segmentation based on iterative watersheds. In *ProRISC Workshop on Circuits, Systems and Signal Processing*, Veldhoven, the Netherlands, November 2003.

[106] Matei Mancas and Bernard Gosselin. Iterative watersheds and fuzzy tumor visualization. In *IEEE Visualization Conference*, Seattle, Washington, October 2003.

[107] Matei Mancas and Bernard Gosselin. Towards an automatic tumor segmentation using iterative watersheds. In *SPIE Medical Imaging*, San Diego, CA, USA, February 2004.

[108] Tim McInerney and Demetri Terzopoulos. Topologically adaptable snakes. In *International Conference on Computer Vision*, pages 840–845, Boston, MA, USA, June 1995.

[109] Tim McInerney and Demetri Terzopoulos. Deformable models in medical image analysis: A survey. *Medical Image Analysis*, 1(2):91–108, 1996.

[110] Tim McInerney and Demetri Terzopoulos. Medical image segmentation using topologically adaptable surfaces. In *Computer Vision, Virtual Reality and Robotics in Medicine and Medial Robotics and Computer-Assisted Surgery*, pages 23–32, Grenoble, France, March 1997.

[111] Tim McInerney and Demetri Terzopoulos. Topology adaptive deformable surfaces for medical image volume segmentation. *IEEE Transactions on Medical Imaging*, 18(10):840–850, October 1999.

[112] Alan K. Meeker, Wesley R. Gage, Jessica L. Hicks, Inpakala Simon, Jonathan R. Coffman, Elizabeth A. Platz, Gerrun E. March, and Angelo M. De Marzo. Telomere length assessment in human archival tissues. *American Journal of Pathology*, 160(4):1259–1268, April 2002.

[113] Fatima A. Merchant and Kenneth R. Castleman. Strategies for automated fetal cell screening. *Human Reproduction Update*, 8(6):509–521, 2002.

[114] Volker Metzler, Jörg Bredno, Thomas Lehmann, and Klauss Spitzer. A deformable membrane for the segmentation of cytological samples. In *SPIE Medical Imaging*, volume 3338, pages 1246–1257, San Diego, CA, USA, February 1998.

[115] Volker Metzler, Thomas Lehmann, Hans Bienert, Khosrow Mottaghy, and Klaus Spitzer. Scale-independent shape analysis for quantitative cytology using mathematical morphology. *Computers in Biology and Medicine*, 30:135–151, 2000.

[116] James V. Miller, David E. Breen, William E. Lorensen, Robert M. O'Bara, and Michael J. Wozny. Geometrically deformed models: A method for extracting closed geometric models from volume data. *Computer Graphics*, 25(4):217–226, July 1991.

[117] Morton Nadler and Eric P. Smith. *Pattern Recognition Engineering*. Wiley-Interscience, 1993. ISBN 0-471-62293-1.

[118] Y. Nakajima and S. Mori. Global and strict curve fitting method. In *International Workshop on Frontiers in Handwriting Recognition*, pages 523–528, Amsterdam, The Netherlands, September 2000.

[119] Jacinto Nascimento and Jorge Marques. An adaptive potential for robust shape estimation. In *British Machine Vision Conference*, pages 343–352, Manchester, UK, September 2001.

[120] A. Nedzved, S. Ablameyko, and I. Pitas. Morphological segmentation of histology cell images. In *International Conference on Pattern Recognition*, volume 1, pages 500–503, Barcelona, Spain, September 2000.

[121] Michael Negnevitsky. *Artificial Intelligence - A Guide to Intelligent Systems*. Addison Wesley, first edition, 2002. ISBN: 0201711591.

[122] Hans Netten, Ian T. Young, Michele Prins, Lucas J. van Vliet, Hans Tanke, Hans Vrolijk, and Willem Sloos. Automation of fluorescent dot counting in cell nuclei. In *International Conference on Pattern Recognition*, pages 84–87, Jerusalem, Israel, October 1994.

[123] Hans Netten, Ian T. Young, Lucas J. van Vliet, Hans J. Tanke, Hans Vroljik, and Willem C.R. Sloos. Fish and chips: Automation of fluorescent dot counting in interphase cell nuclei. *Cytometry*, 28:1–10, 1997.

[124] K. O'Donoghue, J. Chan, J. de la Fuente, N. Kennea, J. R. Anderson, A. Sandison, I. A. G. Roberts, and N. M. Fisk. Fetomaternal trafficking

of fetal mesenchymal stem cells: the persistence of fetal cells in maternal organs. In *Workshop on Fetal Cells and Fetal DNA*, Jena, Germany, April 2004.

[125] Carlos Ortiz de Solórzano, E. García Rodriguez, A. Johnes, D. Pinkel, J.W. Gray, D. Sudar, and S.J. Lockett. Segmentation of confocal microscope images of cell nuclei in thick tissue sections. *Journal of Microscopy*, 193:212–226, March 1999.

[126] Carlos Ortiz de Solórzano, R. Malladi, S.A. Lelièvre, and S.J. Lockett. Segmentation of nuclei and cells using membrane related protein markers. *Journal of Microscopy*, 201(3):404–415, March 2001.

[127] Arnfried Ossen, Thomas Zamzow, Helmut Oswald, and Eckart Fleck. Segmentation of medical images using neural network classifiers. In *International Conference on Neural Networks and Expert Systems in Medicine and Healthcare*, Sheffield, UK, July 1994.

[128] Jacintha N. O'Sullivan, Jennifer C. Finley, Rosa-Ana Risques, Wen-Tang Shen, Katherine A. Gollahon, Alexander H. Moskovitz, Sergei Gryaznov, Calvin B. Harley, and Peter S. Rabinovitch. Telomere length assessment in tissue sections by quantitative FISH: image analysis algorithms. *Cytometry Part A*, 58A:120–131, 2004.

[129] J.B. Pagador, J. Moreno, V. Masero, and J.M. Leon-Rojas. Active contour on the basis of inertia. In *ACM Symposium on Applied Computing*, pages 307–308, Nicosia, Cyprus, March 2004.

[130] Nikos Paragios and Rachid Deriche. Geodesic active contours and level sets for the detection and tracking of moving objects. *IEEE Transactions on Pattern Analysis and Machine Intelligence*, 22(3):266–280, March 2000.

[131] Denise M. V. Pelikan, Wilma E. Mesker, Sicco A. Scherjon, Humphrey H. H. Kanhai, and Hans J. Tanke. Improvement of the Kleihauer-Betke test by automated detection of fetal erythrocytes in maternal blood. *Cytometry Part B (Clinical Cytometry)*, 54B:1–9, 2003.

[132] Doug P. Perrin and Christopher E. Smith. Rethinking classical internal forces for active contour models. In *Computer Vision and Pattern Recognition*, volume 2, pages 615–620, Kauai, Hawaii, USA, December 2001.

[133] Dzung L. Pham, Chenyang Xu, and Jerry L. Prince. A survey of current methods in medical image segmentation. *Annual Reviews of Biomedical Engineering*, 2:315–337, 2000.

[134] Regina Pohle and Klaus D. Toennies. Segmentation of medical images using adaptive region growing. In *SPIE Medical Imaging*, volume 4322, pages 1337–1346, San Diego, CA, USA, February 2001.

[135] Regina Pohle and Klaus D. Toennies. Self-learning model-based segmentation of medical images. *Image Processing and Communications*, 7(3-4):97–113, 2001.

[136] Regina Pohle and Klaus D. Toennies. A three-level evaluation process for segmentation methods in medical imaging. In *SPIE Medical Imaging*, volume 4684, pages 287–298, San Diego, CA, USA, February 2002.

[137] R. Poli and G. Valli. Optimum segmentation of medical images with Hopfield neural networks. Technical report, School of Computer Science, The University of Birmingham, October 1995. CSRP-95-12.

[138] Steven S.S. Poon and Peter M. Lansdorp. Quantitative fluorescence in situ hybridization (Q-FISH). *Current Protocols in Cell Biology*, 18(4):1–21, 2001.

[139] Steven S.S. Poon, Uwe M. Martens, Rabab K. Ward, and Peter M. Lansdorp. Telomere length measurements using digital fluorescence microscopy. *Cytometry*, 36:267–278, 1999.

[140] Frederic Precioso. *Contours actifs parametriques pour la segmentation d'images et videos*. PhD thesis, Universite de Nice - Sophia Antipolis, September 2004.

[141] Frederic Precioso, Michel Barlaud, Thierry Blu, and Michael Unser. Smoothing B-spline active contour for fast and robust image and video segmentation. In *International Conference on Image Processing*, volume 1, pages 137–140, Barcelona, Spain, September 2003.

[142] Frederic Precioso, Michel Barlaud, Thierry Blu, and Michael Unser. Robust real-time segmentation of images and videos using a smoothing-spline snake-based algorithm. *IEEE Transactions on Image Processing*, 14(7):910–924, July 2005.

[143] Christophe Restif and William Clocksin. Comparison of segmentation methods for cytometric assay. In *Medical Image Understanding and Analysis*, pages 153–156, London, UK, September 2004.

[144] Jos B.T.M. Roerdink and Arnold Meijster. The watershed transform: Definitions, algorithms and parallelization strategies. *Fundamenta Informaticae*, 41:187–228, 2001.

[145] Torsten Rohlfing and Calvin R. Maurer Jr. Shape-based averaging for combination of multiple segmentations. In *Medical Image Computing and Computer-Assisted Intervention - MICCAI 2005*, volume 2, pages 838–845, Palm Springs, USA, October 2005.

[146] Remi Ronfard. Region-based strategies for active contour models. *International Journal of Computer Vision*, 13(2):229–251, 1994.

[147] Cecilia Di Ruberto, Andrew Dempster, Shahid Khan, and Bill Jarra. Segmentation of blood images using morphological operators. In IEEE, editor, *International Conference on Pattern Recognition*, volume 3, pages 397–400, Barcelona, Spain, December 2000.

[148] Nathalie Rufer, Tim H. Brümmendorf, Steen Kølvraa, Clauss Bischoff, Kaare Christensen, Louis Wadsworth, Michael Schulzer, and Peter M. Lansdorp. Telomere fluorescence measurements in granulocytes and t lymphocyte subsets point to a high turnover of hematopoietic stem cells and memory t cells in early childhood. *Journal of Experimental Medicine*, 190(2):157–167, July 1999.

[149] J. Da Rugna and H. Konik. Etude comparative de méthodes de segmentation dans une approche orientée indexation. In *Reconnaissance des Formes et Intelligence Artificielle*, Toulouse, France, January 2004.

[150] Stuart Russel and Peter Norvig. *Artificial Intelligence - A Modern Approach*. Prentice Hall, Upper Saddle River, NJ 07458, USA, 1995.

[151] Sabita N. Saldanha, Lucy G. Andrews, and Trygve O. Tollefsbol. Assessment of telomere length and factors that contribute to its stability. *European Journal of Biochemistry*, 270:389–403, 2003.

[152] J. Schröder, A. Tilikainen, and A. de la Chapelle. Fetal leukocytes in the maternal circulation after delivery. *Transplantation*, 17(4):346–354, April 1974.

[153] S. Schüpp, A. Elmoataz, J. Fadili, P. Herlin, and D. Bloyet. Image segmentation via multiple active contour models and fuzzy clustering with biomedical applications. In *International Conference on Pattern Recognition*, volume 1, pages 622–625, Barcelona, Spain, September 2000.

[154] Stan Sclaroff and Lifeng Liu. Deformable shape detection and description via model-based region grouping. *IEEE Transactions on Pattern Analysis and Machine Intelligence*, 23(5):475–489, May 2001.

[155] J.A. Sethian. *Level Set Methods and Fast Marching Methods*, pages 3–13. Cambridge University Press, 1999.

[156] Mehmet Sezgin and Bulent Sankur. Survey over image thresholding techniques and quantitative performance evaluation. *Journal of Electronic Imaging*, 13(1):146–168, January 2004.

[157] Erik M. Shapiro, Stanko Skrtic, Kathryn Sharer, Jonathan M. Hill, Cynthia E. Dunbar, and Alan P. Koretsky. MRI detection of single particles for cellular imaging. *Proceedings of the National Academy of Sciences*, 101(30):10901–10906, July 2004.

[158] Naeem Shareef, DeLiang L. Wang, and Roni Yagel. Segmentation of medical images using LEGION. *IEEE Transactions on Medical Imaging*, 18(1):74–91, January 1999.

[159] Michael E. Sieracki, Stephen E. Reichenbach, and Kenneth L. Webb. Evaluation of automated threshold selection methods for accurately sizing fluorescent cells by image analysis. *Applied and Environmental Microbiology*, 55(11):2762–2772, November 1989.

[160] J. Sijbers, M. Verhoye, P. Scheunders, A. Van der Linden, D. Van Dyck, and E. Raman. Watershed-based segmentation of 3D MR data for volume quantization. *Magnetic Resonance Imaging*, 15(6):679–688, 1997.

[161] Steven W. Smith. *The scientist and engineer's guide to digital signal processing*, pages 11–34. California Technical Publishing, 1997. ISBN 0-9660176-3-3.

[162] Pierre Soille. Grey scale convex hulls: Definition, implementation and application. In *Mathematical Morphology and its Applications to Image and Signal Processing*, volume 12 of *Computational Imaging and Vision*, pages 83–90. Kluwer Academic Publishers, 1998.

[163] P. Spyridonos, D. Glotsos, P. Ravazoula, V. Zolota, and G. Nikiforidis. Pattern recognition based segmentation method of cell nuclei in tissue section analysis. In *International Conference on Digital Signal Processing*, pages 1121–1124, Santorini, Greece, July 2002.

[164] Lawrence H. Staib and James S. Duncan. Boundary finding with parametrically deformable models. *IEEE Transactions on Pattern Analysis and Machine Intelligence*, 14(11):1061–1075, November 1992.

[165] Sun Microsystems. http://java.sun.com/xml/. June 2006.

[166] Lars-Göran Sundblad, Paul Geladi, Arne Dunberg, and Björn Sundberg. The use of image analysis and automation for measuring mitotic index in apical conifer meristems. *Journal of Experimental Biology*, 49(327):1749–1756, October 1998.

[167] S.Y.Tan, W.B. Chan, W.C. Cheng, A. Hagarty, K.T.Lim, and R.Quaife. Rapid prenatal diagnosis of chromosome abnormalities. *Singapore Medical Journal*, 41(10):493–497, 2000.

[168] Gábor Székely, András Kelemen, Christian Brechbühler, and Guido Gerig. Segmentation of 2-D and 3-D objects from MRI volume data using constrained elastic deformations of flexible Fourier contour and surface models. *Medical Image Analysis*, 1(1):19–34, 1996.

[169] Toshiyuki Tanaka, Tomoo Joke, and Teruaki Oka. Cell nucleus segmentation of skin tumor using image processing. In IEEE, editor, *Engineering in Medicine and Biology Society International Conference*, volume 3, pages 2716–2719, Istanbul, Turkey, October 2001.

[170] Toshiyuki Tanaka, Yoko Murase, and Teruaki Oka. Classification of skin tumors based on shape features of nuclei. In *Medicine and Biology Society / Biomedical Engineering Society Conference*, volume 3, pages 1064–1066, Houston, TX, USA, October 2002.

[171] Huseyin Tek and Huseyin Can Aras. Local watershed operators for image segmentation. In *Medical Image Computing and Computer-Assisted Intervention*, pages 127–134, Saint-Malo, France, September 2004.

[172] Sergios Theodoridis and Konstantinos Koutroumbas. *Pattern Recognition*. Elsevier Academic Press, second edition, 2003. ISBN 0-12-685875-6.

[173] Andy Tsai, Anthony Yezzi Jr., William Wells, Clare Tempany, Dewey Tucker, Ayres Fan, W. Eric Grimson, and Alan Willsky. A shape-based approach to the segmentation of medical imagery using level sets. *IEEE Transactions on Medical Imaging*, 22(2):137–154, February 2003.

[174] Jayaram K. Udupa, Vicki R. LaBlanc, Hilary Schmidt, Celina Imielinska, Punam K. Saha, George J. Grevera, Ying Zhuge, L. M. Currie, Pat Molholt, and Yinpeng Jin. Methodology for evaluating image-segmentation algorithms. In *SPIE Medical Imaging 2002: Image Processing*, volume 4684, pages 266–277, San Diego, CA, USA, February 2002.

[175] Michael Unser, Akram Aldroubi, and Murray Eden. B-spline signal processing: Part I - theory. *IEEE Transactions on Signal Processing*, 41(2):821–832, February 1993.

[176] Michael Unser, Akram Aldroubi, and Murray Eden. B-spline signal processing: Part II - efficient design and applications. *IEEE Transactions on Signal Processing*, 41(2):834–848, February 1993.

[177] Corinne Vachier and Fernand Meyer. The viscous watershed transform. Special Issue on Mathematical Morphology after 40 years for the Journal of Mathematical Imaging and Vision, 2004.

[178] Jeroen van der Laak. *Automated Identification of cell and tissue components in pathology*. PhD thesis, University Medical Center St Radboud, Nijmegen, The Netherlands, 2001.

[179] Luc Vincent. Morphological grayscale reconstruction in image analysis: Applications and efficient algorithms. *IEEE Transactions on Image Processing*, 2(2):176–201, April 1993.

[180] Luc Vincent and Pierre Soille. Watersheds in digital spaces: An efficient algorithm based on immersion simulations. *IEEE Transactions on Pattern Analysis and Machine Intelligence*, 13(6):583–598, June 1991.

[181] Carolina Wahlby. *Algorithms for Applied Digital Image Cytometry*. PhD thesis, Uppsala University, October 2003.

[182] J. Walknowska, F. A. Conte, and M. M. Grumbach. Practical and theoretical implications of fetal-maternal lymphocyte transfer. *Lancet*, 1(7606):1119–1122, June 1969.

[183] J.-Y. Wang, D. K. Zhen, M. E. Zilberstein, V. M. Falco, and D. W. Bianchi. Non-invasive exclusion of fetal aneuploidy in an at-risk couple with a balanced translocation. *Molecular Human Reproduction*, 6(2):103–106, 2000.

[184] Xun Wang, Lei He, and William G. Wee. Constrained optimization: a geodesic snake approach. In *International Conference on Image Processing*, volume 2, pages 77–80, Rochester, New York, September 2002.

[185] Simon K. Warfield, Kelly H. Zou, and William M. Wells. Simultaneous truth and performance level estimation (STAPLE): An algorithm for the validation of image segmentation. *IEEE Transactions on Medical Imaging*, 23(7):903–921, July 2004.

[186] Claudia Weierich, Alessandro Brero, Stefan Stein, Johann von Hase, Christoph Cremer, Thomas Cremer, and Irina Solovei. Three-dimensional arrangements of centromeres and telomeres in nuclei of human and murine lymphocytes. *Chromosomal Research*, 11:485–502, 2003.

[187] Paul F. Whelan and Derek Molloy. *Machine Vision Algorithms in Java*. Springer, 2001. ISBN 1-85233-218-2.

[188] Donna J. Williams and Mubarak Shah. A fast algorithm for active contours and curvature estimation. *CVGIP: Image Understanding*, 55(1):14–26, January 1992.

[189] World Wide Web Consortium. http://www.w3.org/xml/. June 2006.

[190] Sue Wu and Adnan Amin. Automatic thresholding of gray-level using multi-stage approach. In *International Conference on Document Analysis and Recognition*, pages 493–497, Edinburgh, Scotland, August 2003.

[191] Jonathan P. Wyllie, R. John Madar, Michael Wright, John Burn, and Christopher Wren. Strategies for antenatal detection of down's syndrome. *Archives of Disease in Childhood*, 76:F26–F30, 1997.

[192] Xianghua Xie and Majid Mirmehdi. Geodesic colour active contour resistent to weak edges and noise. In *British Machine Vision Conference*, pages 399–408, Norwich, UK, September 2003.

[193] Chenyang Xu and Dzung L. Phamand Jerry L. Prince. *Handbook of Medical Imaging*, chapter Image Segmentation Using Deformable Models, pages 129–174. SPIE International Society for Optical Engineering, June 2000.

[194] Chenyang Xu and Jerry L. Prince. Gradient vector flow: A new external force for snakes. In *Computer Vision and Pattern Recognition*, pages 66–71, San Juan, Puerto Rico, June 1997.

[195] Chenyang Xu and Jerry L. Prince. Snakes, shapes and gradient vector flow. *IEEE Transactions on Image Processing*, 7(3):359–369, March 1998.

[196] Ning Xu, Narendra Ahuja, and Ravi Bansal. Automated lung nodule segmentation using dynamic programming and EM based classification. In

SPIE Medical Imaging, volume 4684, pages 666–676, San Diego, CA, USA, February 2002.

[197] Ning Xu, Ravi Bansal, and Narendra Ahuja. Object boundary segmentation using graph cuts based active contours. In *Computer Vision and Pattern Recognition*, pages 87–90, Kauai, Hawaii, USA, December 2001.

[198] Ning Xu, Ravi Bansal, and Narendra Ahuja. Object segmentation using graph cuts based active contours. In *International Conference on Computer Vision*, volume 2, pages 46–53, Nice, France, October 2003.

[199] Faguo Yang and Tianzi Jiang. Cell image segmentation with kernel-based dynamic clustering and an ellipsoid cell shape model. *Journal of Biomedical Informatics*, 34:67–73, 2001.

[200] Xi-Wen Zhang, Ji-Qiang Song, Michael R. Lyu, and Shi-Jie Cai. Extraction of karyocytes and their components from microscopic bone marrow images based on regional color features. *Pattern Recognition*, 37:351–361, 2004.

[201] Y. J. Zhang. A review of recent evaluation methods for image segmentation. In *International Symposium on Signal Processing and Its Applications*, pages 148–151, Kuala Lumpur, Malaysia, August 2001.

[202] Y.J. Zhang. Evaluation and comparison of different segmentation algorithms. *Pattern Recognition Letters*, 18:963–974, August 1997.

[203] Song Chun Zhu and Alan Yuille. Region competition: Unifying snakes, region growing, and Bayes/MDL for multiband image segmentation. *IEEE Transactions on Pattern Analysis and Machine Intelligence*, 18(9):884–900, September 1996.

[204] Song Chun Zhu and Alan L. Yuille. Region competition and its analysis. Technical report, Harvard Robotics Lab., Harvard University, Cambridge MA, USA, 1995.

[205] Kelly H. Zou, Simon K. Warfield, Aditya Bharatha, Clare M.C. Tempany, Michael R. Kaus, Steven J. Haker, William M. Wells III, Ferenc A. Jolesz, and Ron Kikinis. Statistical validation of image segmentation quality based on a spatial overlap index. *Academic Radiology*, 11(2):178–189, February 2004.